

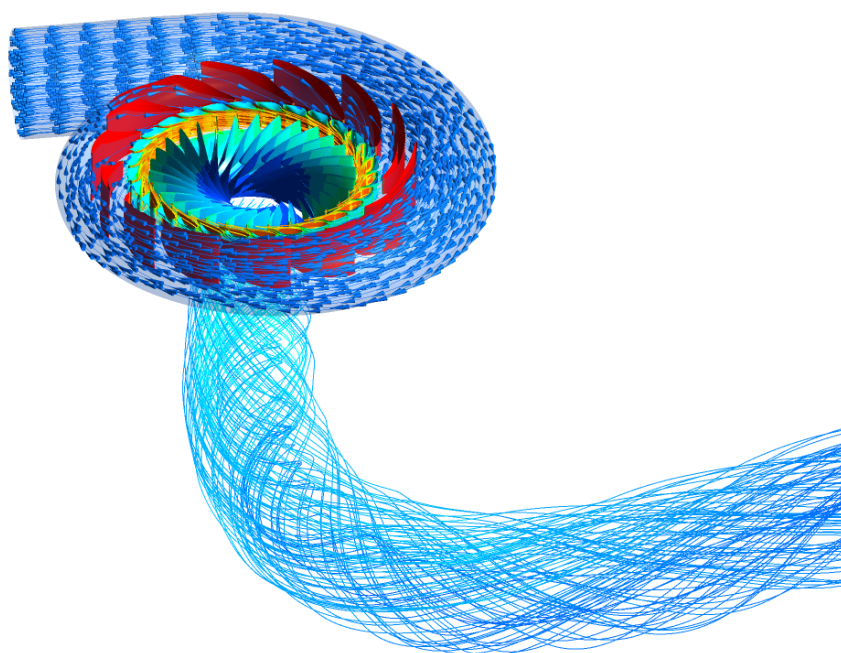
Andreas Nordvik

Variable speed operations of Francis turbines

Hovedoppgave i Produktutvikling og Produksjon

Veileder: Ole Gunnar Dahlhaug, Igor Iliev, and Chirag Trivedi.

Juni 2019



EPT-M-2019-

MASTER THESIS

for

Student Andreas Nordvik

Spring 2019

*Variable speed operation of Francis turbines
Francis turbiner med variabelt turtall***Background**

The renewable energy system of the future need the capability to produce/store energy and generate power when needed. Today, this flexibility is mostly provided from fossil-fueled power plants while in the future, hydropower can provide the flexibility with high reliability.

Today's hydropower technology has been developed to operate with a relatively stable loading over long periods of time. Norwegian hydropower plants are still operated like this, but as the future load variations become increasingly aggressive, the technology lifetime is reduced and maintenance costs are increased.

At the Norwegian Research Centre for Hydro Power Technology, HydroCen , the focus is to on increasing hydropower's flexibility. This includes variable speed operation of generators and turbines. Recently, researchers in the Waterpower Laboratory at the Norwegian University of Science and Technology (NTNU), designed their own high head Francis turbine and published both geometry and model performance data in order to provide other researchers with a relevant case to work with and to promote the Francis-99 workshops. The Francis-99 workshops aim to determine the state of the art of high head Francis turbine simulations (flow and structure) under steady and transient operating conditions as well as promote their development and knowledge dissemination openly. In this project, the student will focus on the efficiency on high head turbines during variable speed operation utilizing the Francis-99 turbine as the test case for the study.

Objective

Calibration of a numerical method for efficiency calculations of Francis turbines

The following tasks are to be considered:

1. CFD-analysis on the Francis turbine runner for selected loads on the Francis-99 turbine. Carry out a parametric study to see if the CPU-time will be reduced by the following:
 - a. Geometry simplification
 - b. Mesh independent study
 - c. Different turbulence models
2. If the student will go to Nepal for a excursion, earlier and further work will be presented as a publication and presented at the conference; *9th International symposium on Current Research in Hydropower Technologies (CRHT-IX)* at Kathmandu University
3. If there is time available, the student will carry out CFD-analysis of a new runner design and compare the numerical data with the Francis-99 turbine.

Within 14 days of receiving the written text on the master thesis, the candidate shall submit a research plan for his project to the department.

When the thesis is evaluated, emphasis is put on processing of the results, and that they are presented in tabular and/or graphic form in a clear manner, and that they are analysed carefully.

The thesis should be formulated as a research report with summary both in English and Norwegian, conclusion, literature references, table of contents etc. During the preparation of the text, the candidate should make an effort to produce a well-structured and easily readable report. In order to ease the evaluation of the thesis, it is important that the cross-references are correct. In the making of the report, strong emphasis should be placed on both a thorough discussion of the results and an orderly presentation.

The candidate is requested to initiate and keep close contact with his/her academic supervisor(s) throughout the working period. The candidate must follow the rules and regulations of NTNU as well as passive directions given by the Department of Energy and Process Engineering.

Risk assessment of the candidate's work shall be carried out according to the department's procedures. The risk assessment must be documented and included as part of the final report. Events related to the candidate's work adversely affecting the health, safety or security, must be documented and included as part of the final report. If the documentation on risk assessment represents a large number of pages, the full version is to be submitted electronically to the supervisor and an excerpt is included in the report.

Pursuant to "Regulations concerning the supplementary provisions to the technology study program/Master of Science" at NTNU §20, the Department reserves the permission to utilize all the results and data for teaching and research purposes as well as in future publications.

The final report is to be submitted digitally in DAIM. An executive summary of the thesis including title, student's name, supervisor's name, year, department name, and NTNU's logo and name, shall be submitted to the department as a separate pdf file. Based on an agreement with the supervisor, the final report and other material and documents may be given to the supervisor in digital format.

- Work to be done in the Waterpower laboratory
 Field work

Department of Energy and Process Engineering, 14. January 2019


Ole Gunnar Dahlhaug
Academic Supervisor

Co-Supervisors:

- Igor Iliev
- Chirag Trivedi

Abstract

The growing share of intermittent energy production, such as wind and solar, makes it increasingly important to have more reliable energy sources to meet the demand of varying power consumption. Hydropower can be used for this purpose, although this often leads to running the turbine under conditions for which it was not designed. Off-design operation will lead to dynamic loads, like pressure pulsations in the runner, which will significantly decrease its lifetime. Francis turbines, specifically designed to operate under variable speed conditions, may be an answer to this challenge and could help levitate the turbine for such wear. As normal synchronous speed Francis turbines are designed to run according to the frequency of the electricity grid, a standardized procedure to design a variable speed turbine is missing. By using computational fluid dynamics (CFD), one can simulate the flow through a turbine and look at its characteristics under different loads in the design process. This master thesis compares the numerically predicted hill chart to experimental measurements of a Francis turbine. The main objective is to create a model for recreating hill charts utilizing CFD. Prediction of hill charts are useful in the design stage of production and may result in a more efficient runner. Investigation of possible simplifications without loss in accuracy is also a subject of study. Simplifications of geometry have been tested to investigate if the simulation time can be reduced without sacrificing accuracy. It turns out that spiral casing can be omitted with little loss in accuracy. The $k - \epsilon$ model showed more accurate and faster results. Numerical simulations of 132 operating points, using $k - \epsilon$ turbulence model, were carried out and the numerical hill chart is predicted. It is observed that the numerical simulations overpredict the efficiency; however, the general shape is predicted well.

Sammendrag

Den økende andelen av uregulerbar kraftproduksjon, som vind og sol, blir det stadig viktigere å ha mer pålitelige energikilder for å tilfredsstille etterspørselen av et varierende strømforbruk. Vannkraft kan brukes til dette formålet, selv om dette ofte medfører å drive turbinen under forhold som den ikke var konstruert for. Turbindrift utenfor design punkt vil føre til dynamiske belastninger, som trykkpulseringer i løpehjulet, noe som vil redusere levetiden betydelig. Francis turbiner, spesielt designet for å operere under variable hastighetsforhold, kan være et svar på denne utfordringen og kunne bidra til å sikre turbinen mot slik slitasje. Ettersom synkront turtall Francis turbiner er konstruert for å kjøre i henhold til frekvensen av strømmettet, mangler vi en standardisert prosedyre for å designe en turbin med variabel hastighet. Ved å bruke numerisk fluiddynamikk (CFD) kan man simulere strømmen gjennom en turbin og se på dens egenskaper under forskjellige belastninger i designprosessen. Denne masteroppgaven sammenligner numerisk forutsatt virkningsgraddiagram med eksperimentelle målinger av en Francis-turbin. Hovedmålet er å skape en modell for gjenskapning av virkningsgradsdiagrammer ved bruk av CFD. Å kunne forutsi virkningsgradsdiagrammer er nyttig i produksjonsstadiet og kan resultere i en mer effektiv turbin. Undersøkelse av mulige forenklinger uten å tape nøyaktighet er også et av temaene i denne oppgaven. Forenklinger av geometri har blitt testet for å undersøke om simuleringstiden kan reduseres uten å ofre nøyaktighet. Det viser seg at spiraltrømmen kan utelates med lite tap i nøyaktighet. $k - \epsilon$ -modellen viste seg å være mer nøyaktig og raskere. Numeriske simuleringer av 132 operasjonspunkter, ved bruk av $k - \epsilon$ turbulensmodell, ble utført og det numeriske virkningsgradsdiagrammet ble konstruert. Det observeres at de numeriske simuleringene overestimerer effektiviteten, men den generelle formen er forutsatt godt.

Acknowledgment

Firstly, I would like to express my sincere gratitude to my advisor, professor Ole Gunnar Dahlhaug, for your support and insight during my master thesis.

Besides my advisor, I would like to thank Igor Iliev and Chirag Trivedi for all your valuable lessons. Thank you for your patience, insightful discussions, and encouragement. I appreciate all the laughs we have shared.

My sincere thanks also go to Madeleine J. Selvig Hallén, Petter T. K. Østby, Ken-Robert G. Jakobsen, and Erik Tengs – your help with ANSYS were great; you guys saved me from a lot of frustration.

Lastly, I would like to thank my family for your continuous support throughout my education. Maria and Torstein - thank you for believing in me and supporting me to go into higher education. I know I don't say it too often.

My daughter, Tuva, is the key to my willpower and drive.
Without her love,
I could not even get started.



Andreas Nordvik, M.Sc.

Department of Energy and Process Engineering, NTNU

Trondheim, June 2019

Table of contents

Task description	ii
Abstract	iv
Sammendrag	v
Acknowledgment	vi
1 Introduction	1
2 Theory	3
2.1 Hydraulic design of high head Francis turbines	3
2.2 Hill charts	5
2.3 Variable speed Francis turbines	6
2.4 The Francis-99 test case	8
2.5 Turbulence modeling	8
2.6 Uncertainty and errors in CFD simulations	10
3 Numerical method	11
3.1 Reducing computational domain	11
3.2 Mesh	14
3.3 Simulation setup	14
3.4 Turbulence models	16
3.5 Boundary conditions	16
3.6 Software and hardware	17
3.7 Mesh independence study	17
4 Results and Discussion	21
4.1 Geometry Simplification	21
4.2 Mesh independence study	25
4.3 High-performance computing (HPC)	27
4.4 Different turbulence models	28

4.5	Main results	29
4.6	Reducing simulation time	36
5	Conclusion	39
6	Further work	40
	References	I
A	Appendix	VII
A.1	Paper for CRHT-IX'19	VII
A.2	Correction of dimensions according to synchronous speed	XVIII
A.3	Reynolds-averaged Navier-Stokes equations (RANS)	XIX
A.4	Mesh statistics for medium mesh for the different domains	XIX
A.5	Constant n_{ED} -efficiency plots	XXIII
A.6	Constant guide vane opening efficiency plots	XXV
A.7	Euler efficiency hill chart compared to normal efficiency	XXVII
A.8	MATLAB Script for creating the Hill chart	XXVIII
A.9	Different messages from ANSYS	XXX
A.10	Script for running jobs on Idun	XXXII
A.11	Script for running jobs on Vilje	XXXIII

List of Tables

2.1	Data from experience for parameters a and b for calculation of NPSH.	3
3.2	Case 2	13
3.4	N=244	20
4.4	N=244	26
4.5	N=188	26
4.6	N=299	26
4.7	BEP	26
4.8	N=244	27

List of Figures

2.1	Velocity diagram of a Francis turbine runner blade, retrieved from [34, Fig. 3].	4
2.2	Example of variable speed hill chart, retrieved from [38].	7
2.3	Example of a hill chart, retrieved from [38].	7
2.4	Two-dimensional view of the investigated model Francis turbine, retrieved from [41] and edited.	8
3.1	Case 1: Full model with spiral case, runner and draft tube	11
3.2	Case 2: No volute only guide vane ring and full draft tube.	12
3.3	Case 3: Short draft tube and no volute.	12
3.4	(a) Draft tube inlet with conic form. (b) Extracting points from guide vane. .	14
3.5	Computational domain of the model Francis turbine with two interfaces namely guide vane to runner (interface-I) and runner to draft tube (interface-II). Made similar to [31].	15
3.6	RMS residuals for pressure, mass, and momentum for three different runner speeds; $n = 188$ [rpm], $n = 244$ [rpm], and $n = 299$ [rpm].	18
3.7	Iteration history of efficiency for two runner speeds; $n = 188$ [rpm] and $n = 244$ [rpm]. Pay attention to the scale of y-axis!	19
4.1	Modelling stay vane angle on guide vane boundary.	25
4.2	Simplified guide vane.	25
4.3	High-performance computing data for Vilje.	27
4.4	Comparison of different turbulence models.	28
4.5	Comparison of experimental and numerically predicted hill chart.	30

4.6	Experimental and numerically predicted hill chart on top of each other.	30
4.7	The three left plots show experimental and numerical CFD data for constant guide vane opening of $\alpha = 7^\circ$. The three right plots show experimental and numerical CFD data for constant $n_{ED} \approx 0.18$	32
4.8	a) Hydraulic losses from incidence on the leading edge at the runner blade. b) Friction loss in runner. The figure is retrieved from [78, Fig. 3].	34
4.9	Difference in efficiency for experimental and numerical data for different constant n_{ED} lines.	35
4.10	Difference in efficiency between experimental and numerical data for different guide vane openings (α).	35
4.11	Variable speed line comparison between experiments and CFD.	36
4.12	Different methods for reducing interpolation points in hill chart.	38
A.1	Mesh statistic for the runner in TurboGrid with 536 616 elements (medium mesh) in one passage. The statistics show that all elements are good in this mesh. XIX	
A.2	Mesh statistic for the guide vane ($\alpha = 7^\circ$) in TurboGrid with 103 267 elements (medium mesh) in one passage. The statistics show that all elements are good in this mesh.	XX
A.3	Mesh statistic for the draft tube in ICEM CFD with 851 190 elements (medium mesh). The statistics show that all elements are good in this mesh.	XX
A.4	Mesh statistic for the simplified guide vane in TurboGrid with 119 637 elements. The statistics show that all elements are better in this mesh compared to Fig. A.2.	XXI
A.6	Experimental and numerical hill charts for different constant n_{ED} lines.	XXIV
A.8	Experimental and numerical hill charts for different guide vane openings (α).	XXVI
A.9	Comparison between Euler efficiency hill chart according to (7) and normal efficiency according to (16).	XXVII
A.10	Memory problem that happens when simulating too many cells, in this case 27.7 million.	XXX
A.11	Artificial wall problem that happens when simulating SST turbulence model.	XXX
A.12	Overflow problem that happens when simulating total pressure inlet.	XXXI

Abbreviations

BEP	Best efficiency point
CAD	Computer-aided design
CFD	Computational fluid dynamics
CFSM	Converter-fed synchronous machine
CPU	Central processing unit
DFIM	Doubly fed induction machine
DNS	Direct numerical simulation
GCI	grid convergence index
GGI	General grid interface
GVO	Guide vane opening
GV	Guide vane
HL	High Load
HPC	High performance computing
NPSH	Nominal positive suction head
PL	Part Load
RMS	Root-mean-square deviation
RSI	Rotor stator interactions
SST	Shear stress transport model
ZLES	Zonal large-eddy-simulation

Nomenclature

α	Guide vane opening [°]
β	Angle between the relative and peripheral velocity [°]
β^*	Closing constant [-]
β_1	Closing constant [-]
ΔV_i	Volume of a mesh element [m ³]
δ_{ij}	Kronecker delta [-]

- ε Turbulent dissipation [J/kg · s]
- η Efficiency [-]
- η_h Hydraulic efficiency [-]
- γ $\gamma_1 = \beta_1/\beta^* - \sigma_{\omega_1} \kappa^2 / \sqrt{\beta^*}$
- κ Closing constant [-]
- μ Dynamic viscosity [Ns/m²]
- μ_T Turbulent viscosity [Ns/m²]
- ν_T Eddy viscosity [[m²/s]
- ω Specific turbulence dissipation rate [1/s]
- ω_b Angular rotational speed of runner [rad/s]
- \bar{f}_i External forces [m²/s²]
- \bar{p}_i Mean pressure [Pa]
- $\overline{u'_i u'_j}$ Reynolds stress [m²/s²]
- \bar{u}_i Velocity component in corresponding direction [m/s]
- $\overline{U_{i,j}}$ Mean velocity [m/s]
- ϕ Parameter of study used in GCI [-]
- ρ Density [kg/m³]
- σ_ε $k - \varepsilon$ model constant [-]
- σ_ω Closing constant [-]
- σ_k Closing constant [-]
- σ_{ω_1} Closing constant [-]
- σ_{ω_2} Closing constant [-]
- τ_{ij} Turbulent shear stress [Pa]
- \underline{c} Reduced absolute velocity [-]
- \underline{u} Reduced peripheral velocity [-]
- A Area [m²]
- a NPSH coefficient [-]

- B Runner height [m]
- b NPSH coefficient [-]
- c Absolute velocity [m/s]
- C_μ $k - \varepsilon$ model constant [-]
- $C_{\varepsilon 1}$ $k - \varepsilon$ model constant [-]
- $C_{\varepsilon 2}$ $k - \varepsilon$ model constant [-]
- D Runner diameter [m]
- e_a Approximate relative error [-]
- F_1 Function [-]
- f_{grid} Grid frequency [Hz]
- g Gravitational constant [m/s²]
- H Head [m]
- h Representative size factor [mm]
- H_e Effective head [m]
- k Turbulent kinetic energy [J/kg]
- N Number of elements/points [m]
- n Rotational speed [rpm]
- n_{ED} Dimensionless rotational speed [-]
- p Apparent order [-]
- Q Discharge [m³/s]
- Q_{ED} Dimensionless volumetric flow [m³/s]
- r Mesh refinement factor [-]
- T Torque [Nm]
- t Time [s]
- u Peripheral velocity [m/s]
- w Relative velocity [m/s]
- z Height [m]

Z_p Number of poles in generator [-]

Subscripts

$_1$ Inlet

$_2$ Outlet

$_m$ Meridional/mechanical

$_t$ Turbine mode

$_u$ Peripheral

$_{132}$ 132 operation points

$_{21}$ fine to medium mesh size

$_{corr}$ corrected value

$_h$ Hydraulic

$_{in}$ input

1 Introduction

In 2017 the world's energy consumption rose with 2,2% and was the fastest growing since 2013. Coal remains the world's dominant source of power, with a share of 38.1% in 2017, almost as much as natural gas (23.2%) [1]. Third in line comes hydroelectricity, the over 100-year-old invention [2], with a share of 15,9% of the global power production [1]. Norway produces roughly 130 TWh in a normal year [3], which makes it the biggest producer of hydropower in Europe [1]. For this reason, Norway is often referred to in the media as Europe's «green battery» [4], although it is debatable whether or not this will become a reality [5]. In contrast, more than half of the growth in renewable energy came from wind energy [1]. In 2015 wind accounted for 3.7% of the world's energy production, and prognosis says by 2030 it could be 20%, according to the Global Wind Council [6]. Norway is also following this trend, and 2017 was a record year for wind power [7]. Relying on intermittent energy sources such as wind and solar comes with the challenge to meet the consumption demand for electricity. At a large scale, variations in wind power production to power demand can be smaller from a perspective across borders [8]. However, wind power makes no measurable contribution to the primary frequency response for the electricity grid, whereas hydropower, on the other hand, contributes a large proportion of primary frequency response [9].

The Francis turbine is the most common hydropower turbine in Norway [10]. This reaction turbine is the most flexible with a wide range of head between 50 - 650m [11], making it suitable for many sites in Norway. Conventional Francis turbines are single-regulated, fixed synchronous speed type machines meaning fixed runner blades with a runner speed set to match the frequency of the electric grid, which in Norway is 50 Hz. This involves operating the turbine at design point, where the runner has the highest efficiency, and there is little to no swirl at the outlet of the runner [11]. If the turbine is operated away from the design point, i.e. best efficiency point (BEP), efficiency decreases. Having variations in power consumption throughout the day and season make power plant owners push their turbines to operate under conditions for which it was not designed. Doing this will increase the intensity of transient phenomena in the runner, like pressure pulsations in the rotor-stator interaction (RSI) and vortex rope in the draft tube [12]. These transient phenomena cause wear and tear on the runner and hence, a decrease in lifetime [13].

Variable speed operation of Francis turbines, using the doubly fed induction machine (DFIM) or the converter-fed synchronous machine (CFSM) omits the need for synchronous speed of the runner [14, 15]. With this technology, the speed of the runner to be freely adjusted according to the flow conditions and electricity demand. Already in 1987, Farrell and Gulliver investigated the hydromechanical aspects of variable speed hydro turbine operation [16]. The development of variable-speed pumped-storage plants dates back to the early 1990s in Japan, where pioneering achievements took place, and the world's first of such facilities were successfully commissioned [17]. This 400 MW adjustable speed pump storage unit can operate in a range of 330 rpm to 390 rpm utilizing a cycloconverter [18]. Heckelsmueller [19] showed that in conventional synchronous speed turbines, the efficiency falls rapidly when operated with smaller heads than the design head. And by applying variable speed technology, it is possible to operate within a range of $\pm 40\%$ of design head with the maximum efficiency, assuming a nominal guide vane aperture. The hill chart of variable speed turbines appears to be "stretched" in the direction of constant guide vane opening, making the turbine operate at high efficiency over a wider range

of runner speed (see Fig. 2.2). In the design process of Francis turbines, the synchronous speed is a governing parameter for the turbine's dimensions [11]. However, when variable speed operation is introduced a standardized procedure in the design of such turbine is missing.

With the rapid development of computer technology, computational fluid dynamics (CFD) has emerged as a powerful tool to directly simulate internal turbulent flow in individual or multiple components of a turbo machine [20, 21]. Turbines are tailor-made to specific conditions at a specific site, and small improvements in the geometry can have a large positive effect on operation [22]. A CFD aided design methodology applied to hydraulic turbines is, therefore, a desirable approach for increasing efficiency [23]. This has also been studied in [24, 25]. The efficiency diagram, also called hill chart, provides useful information about a turbine. The first numerically predicted hill chart using CFD was published in 1996 [26]. Only two other studies have been carried out on the prediction of hill charts using CFD [27, 28]. Accurate prediction of hill charts is useful in the design stage of production and can be used in an optimization procedure which may result in a more efficient runner [27]. The main objective of this work is to create a model for making hill charts using CFD.

This master thesis seeks to investigate the efficiency of high head Francis turbines during variable speed operation, utilizing the Francis-99 turbine at NTNU as validation for the study [29]. By means of CFD simulations, construction of 132 operating points in the hill chart is predicted. These simulations are carried out using 11 different guide vane openings (GVO) from part load (PL) (GVO 4°) to high load (HL) (GVO 14°). All simulations are then compared with experimental data for validation; data is provided by Iliev [30]. Due to discrepancies in efficiency being large in this study from Trivedi et al. [31], together with the aforementioned transient phenomena, it was decided to do mesh independence study at PL with GVO 7° , as well as for BEP (GVO being 9°). To ensure precise simulations for a reasonable computational cost, a parametric study on geometry simplification, mesh size, and different turbulence models are carried out. Simulations for three different cases are tested; full simulation with spiral case, no spiral case, and no spiral case with short draft tube. As a part of the mesh independence study, the simulation time was compared for three different meshes. Three different turbulence models are also studied to assess their accuracy and speed. Finally, an investigation of removing simulation points to reduce computations without sacrificing the model's precision is performed. In one sentence, as written in the task description (see p. ii), the objective statement is; «Calibration of a numerical method for efficiency calculations of Francis turbines.»

To address the last two points (2 and 3) in the task description (p. ii): The publication presented at the conference; *9th International Symposium on Current Research in Hydropower Technologies* (CRHT-IX) at Kathmandu University, is found in Appendix A.1. The last task was to carry out CFD-analysis of a new runner design and compare with the Francis-99 turbine (point 3); unfortunately, this design was not ready in time to perform any CFD-analysis.

2 Theory

Most of the theory in this section, with the exceptions of some rephrasing, some paragraphs, and Section 2.6, is reproduced from the author's project work [32].

2.1 Hydraulic design of high head Francis turbines

The conventional method for the design of high head Francis turbines are described in Brekke's «Pumper & Turbiner,» and is presented in this section [33].

To design high head Francis turbines, it is necessary to start with the outlet geometry and dimensions of the runner. We start with the volume flow at BEP, denoted by $*Q$, and the effective head, H . The selection of the peripheral velocity at the outlet of the runner, u_2 , and the meridian velocity, c_{m2} , is based on the submergence of the runner, given by the net positive suction head of the turbine (NPSH):

$$NPSH = a \frac{c_{m2}^2}{2g} + b \frac{u_2^2}{2g}, \quad (1)$$

where a and b are constants selected from Table 2.1, c_{m2} and u_2 is the meridian component of the absolute velocity and the peripheral velocity on the outlet respectively, and g is the gravitational constant.

Table 2.1: Data from experience for parameters a and b for calculation of NPSH.

Parameter	Turbines	Pumps
a	$1.05 < a < 1.15$	$1.6 < a < 2.0$
b	$0.05 < b < 0.15$	$0.2 < b < 0.25$

It is assumed that the runner has no swirl at the outlet of the runner at BEP, i.e. $c_{u2} = 0$. Due to experience in the design of Francis turbines, the outlet angle is selected from a range of $13^\circ \leq \beta_2 \leq 19^\circ$. The value of u_2 is within the range of $35m/s \leq u_2 \leq 43m/s$, with the highest value selected for high head Francis turbines. Now it is possible to calculate the outlet diameter (D_2) of the runner by inserting the relation (2) into (3), given by;

$$\tan(\beta_2) = \frac{c_{m2}}{u_2}, \quad (2)$$

$$D_2 = \sqrt{\frac{4*Q}{\pi c_{m2}}}. \quad (3)$$

To calculate the rotational speed of the runner one uses the relationship between u_2 and the angular velocity of the runner, ω_b ;

$$u_2 = \omega_b \frac{D_2}{2}, \quad (4)$$

where $\omega_b = \frac{2\pi n}{60}$ is the angular rotational velocity of the runner. This gives,

$$n = u_2 \frac{60}{\pi D_2}. \quad (5)$$

In the conventional synchronous speed turbine, n must be adjusted to meet the frequency of the electricity grid, which in Norway is 50 [Hz]. The synchronous speed is given by,

$$n = \frac{60 * f_{grid}}{Z_p}, \quad Z_p \in \mathbb{N}, \quad (6)$$

where Z_p is the number of pole pairs in the generator and f_{grid} is the grid frequency, $f_{grid} = 50$ [Hz] in Norway. If we want to keep the blade angle on the outlet, we must correct the outlet diameter, D_{2corr} , this explained in Appendix A.2. The main reason we want to do this is to conserve the velocity diagram at the outlet, to reach the true best efficiency point, see Fig. 2.1. The submergence should now be controlled for and can be calculated by (1).

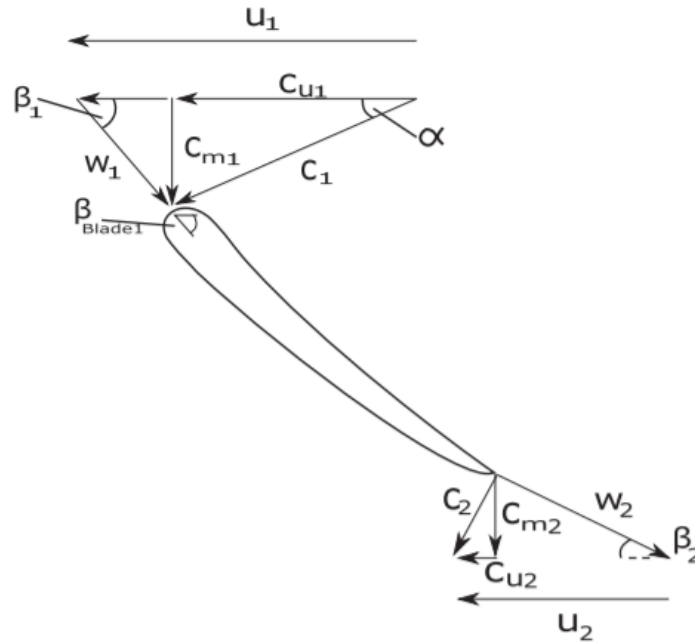


Figure 2.1: Velocity diagram of a Francis turbine runner blade, retrieved from [34, Fig. 3].

When we have found the corrected outlet dimension, it remains to calculate the inlet dimensions at the hub. The main equation for Francis turbines is the Euler's turbine equation given by;

$$\eta_h = \frac{1}{gH} (c_{u1}u_1 - c_{u2}u_2) = 2(\underline{u}_1 c_{u1} - \underline{u}_2 c_{u2}). \quad (7)$$

We have previously assumed no swirl at the outlet, i.e. $c_{u2} = 0$, which reduce the hydraulic efficiency to;

$$\eta_h = \frac{1}{gH} c_{u1} u_1 = 2 \underline{u}_1 \underline{c}_{u1} = 0.96, \quad (8)$$

where \underline{u}_1 is the reduced peripheral velocity at the inlet. The underline represents the reduced values given as $\underline{u}_1 = \frac{u_1}{\sqrt{2gH_e}}$. \underline{c}_{u1} is the reduced tangential component of the absolute velocity at the inlet. To minimize the possible impact loss when varying the guide vane angle, we choose the relationship between \underline{u}_1 and \underline{c}_{u1} . For high head Francis turbines, a value of $\underline{u}_1 = 0.71 - 0.73$ will approximately meet this criterion. By selecting, as an example, $\underline{u}_1 = 0.71$ we can calculate \underline{c}_{u1} by (8),

$$\underline{c}_{u1} = \frac{0.96}{2\underline{u}_1} = \frac{0.96}{2 \cdot 0.71} = 0.67. \quad (9)$$

Now the inlet diameter of the turbine can be calculated by the following relationship:

$$D_1 = \frac{\underline{c}_{u1}}{\underline{\omega}} = \frac{2\underline{u}_1 \sqrt{2gH_e}}{n\pi/30}. \quad (10)$$

From continuity, where we assume 10% acceleration through the runner we get:

$$c_{m1} A_1 = c_{m2} A_2 \quad \& \quad c_{m2} = 1.1 c_{m1}, \quad (11)$$

where A_1 and A_2 is the area at the inlet and outlet respectively. We often want to have an accelerated flow through the runner to avoid a detached flow. Now we can calculate the height of the inlet given by:

$$B_1 D_1 \pi = \frac{1.1 \pi D_2^2}{4} \implies B_1 = \frac{0.275 D_2^2}{D_1}. \quad (12)$$

Finally, we can calculate the inlet angle of the blade from:

$$C_{m1} = \frac{c_{m2}}{1.1} \quad \& \quad u_1 = 0.72 \sqrt{2gH_e} \quad \& \quad \tan(\beta_1) = \frac{c_{m1}}{u_1 - c_{m1}}, \quad (13)$$

where β_1 is the inlet angle of the blade.

Now we have derived the main dimensions in the design of Francis turbines. All the content here is retrieved from Brekke [33].

2.2 Hill charts

As mentioned in the introduction (Section 1), the hill chart provides us with useful information about a turbine. The efficiency diagram is also called the characteristic diagram; this is a suitable name as it shows the turbines characteristics, or how it performs, under different operating conditions [35]. Hill charts are created with dimensionless parameters, so it is applicable for

all turbines that are equally shaped geometrically. We can then compare with other rotating machinery, models, and prototypes [35]. According to IEC 60193, to construct the hill chart, the dimensionless volume flow Q_{ED} is plotted against the dimensionless rotational speed n_{ED} [36]. These parameters are given as;

$$Q_{ED} = \frac{Q}{D_2^2 \sqrt{gH}}, \quad (14)$$

$$n_{ED} = \frac{nD_2}{\sqrt{gH}}, \quad (15)$$

where Q is the discharge (volumetric flow rate) through the turbine, D_2 is the outlet diameter, H is the effective head, n is the rotational speed, and g is the gravitational constant.

To create the experimental hill chart in the laboratory, one must measure the flow, head, and torque. The guide vane opening must be kept constant while the rotational speed is varied. This procedure is then repeated for several different guide vane openings, and by (14) and (15) one can plot the points along constant guide vane lines. The hill charts iso-efficiency curves are then interpolated using the data from the procedure above. The efficiency is calculated from

$$\eta = \frac{\omega_b T}{\rho g Q H}, \quad (16)$$

where T is the torque on the runner's hub, shroud, and blades and ω_b is the rotational speed.

2.3 Variable speed Francis turbines

There are few papers or literature connected to variable speed Francis turbines. In general, most articles only explain what the benefits of variable speed operation could be but do not say anything about the design features of the turbines [37]. A study from Farell and Gulliver lists the possible advantages of variable speed turbine [16]:

1. Improved performance at off-design heads and improved range of operating heads. Low head propeller turbines, in particular, can experience a very wide range of operating head as a percent of design head.
2. Improved performance at off-design discharges and improved range of operating discharges. This is the primary topic of [16].
3. Improved performance for pump-turbine units. Here if the rotational speed is to be the same for both turbines and pump operations, some sacrifice in efficiency in either or both modes is generally necessary.

Tengs et al. [34] suggested a method to design variable speed Francis turbines using a numerically predicted hill diagram. With a very simplified passage model and limited computational resourced, they were able to improve the efficiency with 0.25% over a specific line of operation. Given the vast oversimplification of the geometry and the fact that only 40 operating points were used for creating the hill chart, the result from this study is questionable.

The rest of this subsection 2.3 explains the concept of variable speed Francis turbine and is directly retrieved from Sundf r's master thesis [38].

The idea of variable speed is that if the head or discharge changes, the rotational speed can be adjusted accordingly to maintain high efficiencies. This is demonstrated in Fig. 2.2. For fixed speed operation at a certain head, the efficiency of the turbine will decrease from a to b' when the discharge decreases from Q_a to Q_b . With variable speed operation, the speed can be adjusted from n_a to n_b to obtain an efficiency in point b , which is equivalent to the efficiency in point a .

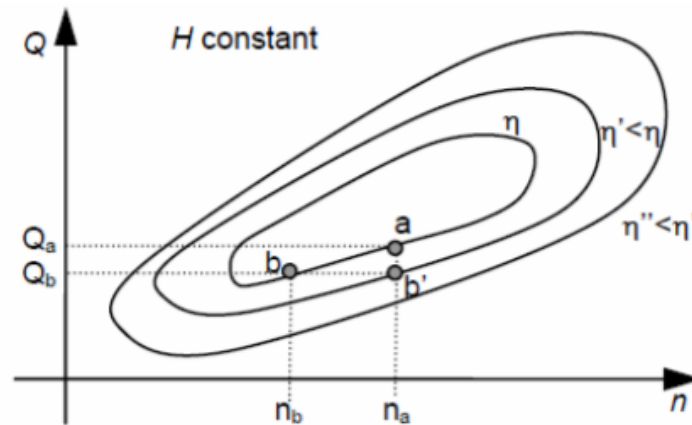


Figure 2.2: Example of variable speed hill chart, retrieved from [38].

Consequently, a variable speed turbine permits maximum efficiency tracking for a given power demand [39]. This kind of operation is only possible if the hill chart looks like the one in Fig. 2.2. If the hill chart curve is more symmetrical like in Fig. 2.3, adjusting the speed in either direction will not affect efficiency. Therefore, the goal is an attempt to make a turbine design, which ultimately can yield a hill chart curve that looks similar to the one in Fig. 2.2. However, the design should not be adjusted to such an extent that the hydraulic efficiency becomes significantly lower. The idea is to produce a «stretched» hill chart without significantly lowering the overall efficiencies.

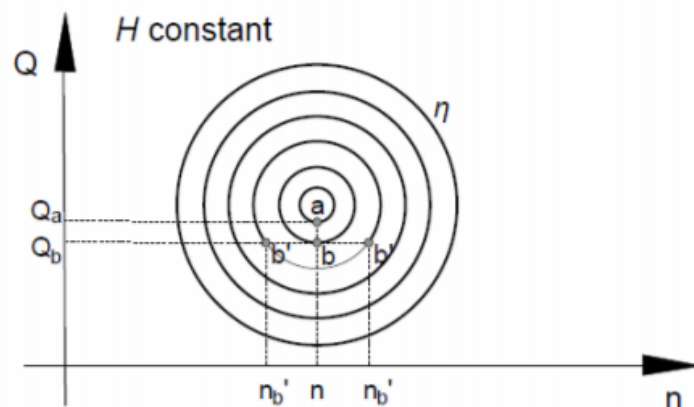


Figure 2.3: Example of a hill chart, retrieved from [38].

2.4 The Francis-99 test case

The test case for this study is a model turbine at the Waterpower Laboratory at NTNU. It is a Francis type 1:5.1 scaled model of a prototype in a Norwegian power plant called Tokke [40]. It includes a spiral casing, a distributor with 14 stay vanes integrated into the spiral casing and 28 guide vanes. The runner has 15 blades with an additional 15 splitter blades, for a total of 30 runner blades. The draft tube is an elbow-type. A 2D section of the model is illustrated in Fig. 2.4. The test rig is a hydraulic system capable of generating $\approx 14\text{m}$ head for open loop, and $\approx 100\text{m}$ head for closed loop [41]. The experimental data used to verify the numerical simulation in this master thesis is given by Iliev et al. [30] study on the same model turbine.

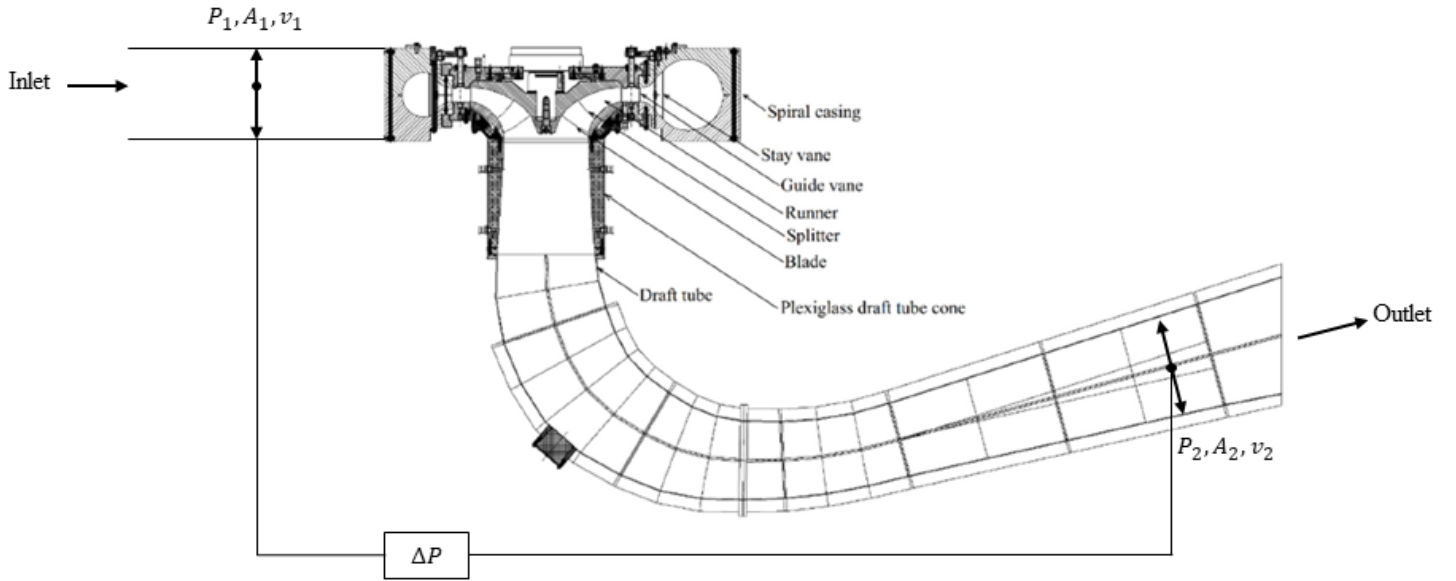


Figure 2.4: Two-dimensional view of the investigated model Francis turbine, retrieved from [41] and edited.

2.5 Turbulence modeling

The objective of turbulence modeling for the RANS equations is to approximate the Reynolds stress. The Reynolds stress can be solved through the eddy viscosity model. RANS equation and eddy viscosity model are shown in Appendix A.3. The eddy viscosity can be solved through different turbulence models. The most common turbulence model is the $k - \epsilon$ -model [42] and was introduced the first time by Jones and Launder [43]. This is a two-equation model, which means, the model has two transport equations in order to represent the turbulence of the flow. These equations are solved for turbulent kinetic energy and energy dissipation rate, described below.

The first transport variable is turbulent kinetic energy k , defined as:

$$k = \frac{1}{2} \left(\overline{(u'_{11})^2} + \overline{(u'_{22})^2} + \overline{(u'_{33})^2} \right), \quad (17)$$

where u' is the fluctuating velocity component.

This variable is used in the first transport equation:

$$\frac{\partial(\rho k)}{\partial t} + \frac{\partial(\rho k u_i)}{\partial x_i} = \frac{\partial}{\partial x_i} \left[\left(\mu + \frac{\mu_T}{\sigma_k} \right) \frac{\partial k}{\partial x_j} \right] + P_k - \rho \varepsilon. \quad (18)$$

The transport equation of turbulent dissipation, ε , is:

$$\frac{\partial(\rho \varepsilon)}{\partial t} + \frac{\partial(\rho \varepsilon u_i)}{\partial x_i} = \frac{\partial}{\partial x_i} \left[\left(\mu + \frac{\mu_T}{\sigma_k} \right) \frac{\partial \varepsilon}{\partial x_j} \right] + C_{1\varepsilon} \frac{\varepsilon}{k} P_k - C_{2\varepsilon} \rho \frac{\varepsilon^2}{k}, \quad (19)$$

where u_i represents the velocity component the i^{th} direction, P_k is the production of turbulent kinetic energy and μ represents the dynamic viscosity. μ_T represents the eddy viscosity and is given by:

$$\mu_T = \rho C_\mu \frac{k^2}{\varepsilon}. \quad (20)$$

The equations also consist of some adjustable constants C_μ , $C_{1\varepsilon}$, $C_{2\varepsilon}$, σ_k , and σ_ε . These constants are a result of many iterations of curve fitting for a wide range of turbulent flows [44]. Although this model is famous for its robustness and low computational cost, it performs poorly in the boundary layer [45].

A second way of modeling the turbulence in a flow is with the Shear Stress Transport model (SST). «The SST model was originally used for aeronautics applications but has since made its way into most industrial, commercial and many research codes» [46]. This model was first introduced by Menter in the mid-1990s, where he used the standard $k - \varepsilon$ -model, described above, and the $k - \omega$ model first created independently by Kolmogorov [47]. Using the strength of $k - \varepsilon$ to describe the flow in the free-stream and the $k - \omega$ in the viscous boundary layer, Menter showed that through a switching function between the two models, the SST model could better predict the accuracy for boundary layers in an adverse pressure gradient than any similar model [48]. The SST model is expressed mathematically as:

$$\frac{D\rho k}{Dt} = \tau_{ij} \frac{\partial u_i}{\partial x_j} - \beta^* \rho \omega k + \frac{\partial}{\partial x_j} \left[\left(\mu + \sigma_k \mu_T \right) \frac{\partial k}{\partial x_j} \right], \quad (21)$$

$$\frac{D\rho \omega}{Dt} = \frac{\gamma}{\nu_T} \tau_{ij} \frac{\partial u_i}{\partial x_j} - \beta \rho \omega^2 + \frac{\partial}{\partial x_j} \left[\left(\mu + \sigma_\omega \mu_T \right) \frac{\partial \omega}{\partial x_j} \right] + 2(1 - F_1) \rho \sigma_{\omega 2} \frac{1}{\omega} \frac{\partial k}{\partial x_j} \frac{\partial \omega}{\partial x_j}, \quad (22)$$

where τ_{ij} is the turbulent shear stress, ω is specific turbulence dissipation rate, F_1 is a function described in [49]. β^* , σ_k , σ_ω and $\sigma_{\omega 2}$ is closure coefficients also described in [49].

In CFD, it is impossible to resolve all the turbulent scales in the flow field without discretizing as far down as the Kolmogorov microscales. This is called direct numerical simulation (DNS) [50]. The number of nodes needed to solve required for DNS of homogeneous isotropic turbulence is given as; $N^3 \sim Re_T^{9/4}$ [51]. The Francis-99 runner can reach $Re = 1.8 \times 10^6$ at BEP [41], which corresponds to 1.19×10^{14} cells to perform DNS. To do this often involves high-performance computers (HPCs) with big capability both with respect to memory and performance [52].

2.6 Uncertainty and errors in CFD simulations

«The best measure of the efficiency of a solution method is the computational effort required to achieve the desired accuracy» [53]. This section will outline the different numerical uncertainty and errors related to CFD and will give insight into limitations when performing CFD simulations.

First, what is the difference between uncertainty and error? According to AIAA guidelines [54]:

Uncertainty is defined as: «A potential deficiency in any phase or activity of the modeling process that is due to the lack of knowledge.»

Error is defined as: «A recognizable deficiency in any phase or activity of modeling and simulation that is not due to lack of knowledge.»

A complete detailed description of the different categories of errors and uncertainties is found in [53, 55] but will be briefly outlined here:

1. Physical modeling errors: Are the errors related to the description of the model and deliberate simplifications of the model. This includes: • An incomplete understanding of the model to be solved, • geometry modeling error, i.e. simplifying the model's geometry, thereby introducing uncertainty (e.g. include fillets or remove part of the geometry), • parameters introduced in the model are known but with a degree of uncertainty (e.g. fluid properties or inlet/outlet conditions), and • the experimental confirmation is not possible or incomplete [56].
2. Iterative convergence errors: Entails stopping the iteration process at a reasonable time to decrease the computational cost but introduces error. This error scales with the variation of the solution for the last iterations of the simulation and is described in Section 3.7.1.
3. Discretization errors: «ANSYS CFX uses an element-based finite volume method, which first involves discretizing the spatial domain using a mesh [57].» This is an approximation which becomes more accurate for denser meshes. To study the influence of discretization; the mesh independence study is often used. This is outlined in Section 3.7.2.
4. Programming and user errors: The CFD user is responsible for trying to eliminate these kinds of error. It is often difficult for the user to locate their own errors to study their code. A better way of reducing programming errors is to run small test cases, for which the results can be compared against other studies or analytical solutions. Being thorough in analyzing the results is also crucial, e.g. checking if boundary conditions are met.
5. Computer round-off errors: Involves the computers capability to store floating point numbers. Typically, this means storing numbers as 64-bit words. Using double-precision in ANSYS CFX ensures numerical accuracy by doubling the computer memory used for a given problem [58]. Computer round-off error is not considered significant compared to other sources of errors [55].

3 Numerical method

3.1 Reducing computational domain

The content in this section has been reproduced with some improvements from the authors' project thesis [32].

The experimental model in the laboratory consists of many parts in which several of them have an impact on the measured output data. A complete simulation of the turbine with spiral casing, distributor, runner and draft tube including the labyrinth seal and disk friction losses is necessary for a realistic simulation of the flow in Francis turbines [59]. However, the increasing complexity and size of the geometry will make a necessity for more cells in the computational mesh in order to get a good resolution of the flow in the simulation. This is computationally demanding and will result in longer simulation time. A full simulation with all details is therefore not feasible. The spiral case and draft tube are large and thereby requires a lot of cells. A study by Jakobsen et al. [60], showed that reducing the computational effort of high head Francis turbines by limiting the computational domain can increase the relative speedup 2.2 times with no volute and short draft tube. Similarly, the reduction of the computational domains is assessed in this thesis. The simulations have been divided into three different cases; Case 1: Full model, Case 2 No spiral case and Case 3: Short draft tube and no spiral case. The different cases are presented in Fig. 3.1 - 3.3. Case 3, the short draft tube and no spiral case, was kindly provided by Jakobsen's study [60]. The spiral case, used in Case 1, was retrieved from the second workshop of Francis-99, and it was not possible to alter the mesh.

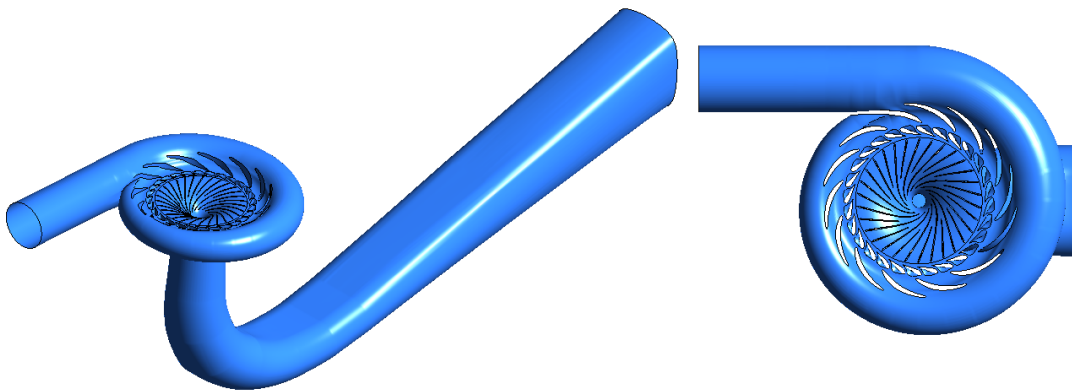


Figure 3.1: Case 1: Full model with spiral case, runner and draft tube

All simulations of Case 1-3 were performed with steady-state analysis type and at runner speed equal $n_{ED} = 0.18$, and guide vane opening $\alpha = 4^\circ$. This operation point were selected to compare against Hallén's thesis [61], which could be used as an indicator to reduce user errors. A relative strict convergence criterion for all the simulations was set to root-mean-square (RMS) $\leq 10^{-5}$. Simulations were set to run for 1000 iterations if the convergence criteria for RMS of pressure, mass-momentum, and turbulent parameters were not met. All the parameters used for performing the numerical simulations for the geometry study are shown in Table 3.1

Yaping et al. showed that the opening-type boundary condition gave a slightly better estimation of efficiency [62]. In order to further investigate these effects, several different outlet conditions

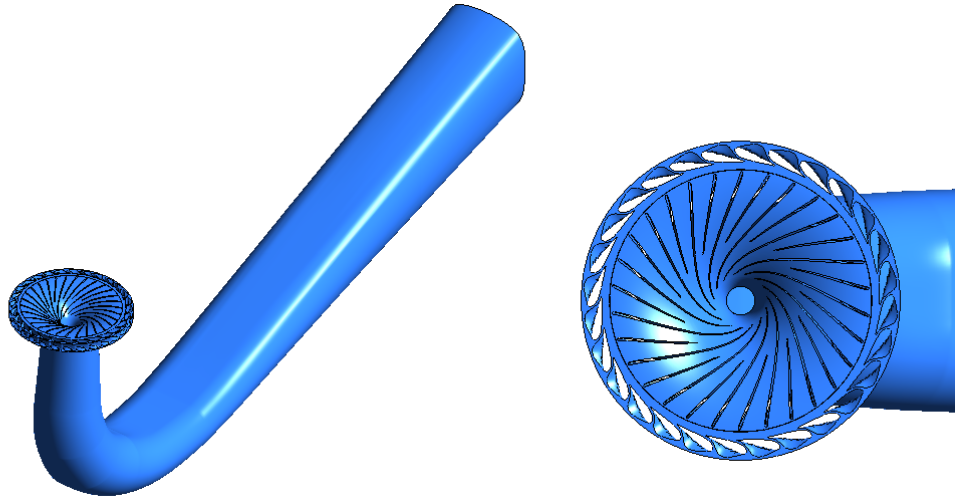


Figure 3.2: Case 2: No volute only guide vane ring and full draft tube.

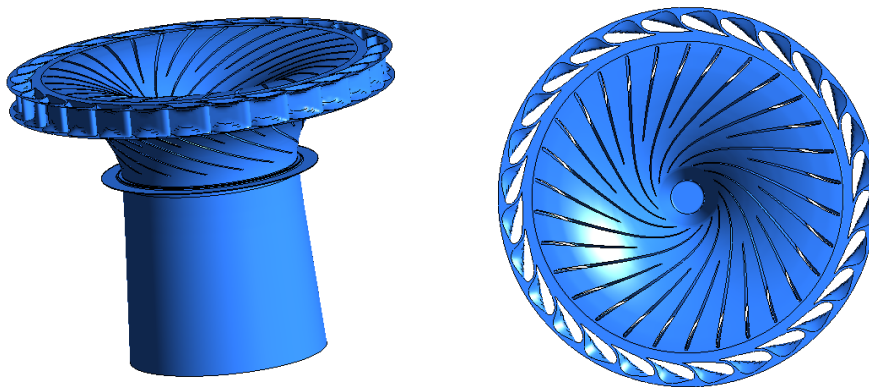


Figure 3.3: Case 3: Short draft tube and no volute.

were tested on case 2. More runs were carried out on case 2 due to its ability to easily improve and alter the mesh. The different meshes and boundary conditions for case 2 are shown in Table 3.2. The pressure at the outlet was set equal to the measured pressure from experiments $P_{out} = 113kPa$, see Section (2.4). However, CFX will adjust the pressure at the inlet to meet this boundary condition and should, therefore, be no different than a 0 Pa outlet condition. A slight difference was observed between the two was observed.

Total pressure inlet and static pressure outlet are very sensitive to initial guess [63]; therefore, the pressure from experiments (see Section 2.4) was applied. Unfortunately, this did not work, and the program stopped with an overflow problem after only 5 iterations, see Appendix A.2. A mass flow inlet condition was therefore applied instead.

Although a proper mesh Independence study was not performed at this stage, different mesh sizes for the runner and draft tube were tested in order to observe the impact of mesh refinement. In addition, a test on the number of cells that could be numerically calculated on the local desktop computer (see Table 3.1), was performed. The largest number of cells, limited by RAM on the computer (see Section 3.6), were run #11 with a global element count of 26.37 million.

Table 3.1: Simulation setup performed on all cases in the reduced geometries.

Parameter	Description
Analysis type	Steady-State
Interfaces	Frozen rotor; discretization type-GGI
Fluid	Incompressible Newtonian fluid; water properties updated with actual density and viscosity
Boundary conditions	Inlet: mass flow inlet with direction, Turbulence intensity 5% Outlet: Outlet-type with static pressure Opening-type with Opening Pres. and Dirn , Normal to Boundary Reference pressure: 0 Pa
Discretization and solution controls	Advection scheme: High resolution Turbulence numeric: First order
Turbulence models	Standard $k - \epsilon$ (scalable wall function), $k - \omega$ SST (automatic wall function)
Convergence control	rms of pressure, mass-momentum, and turbulent parameters $\leq 10E-5$
Physical timescale	1/rpm = 0.0281 [s]
Run type	IBM MPI Local Parallel: Partitions 8 (Logical)
Total run	Case 1: $k - \epsilon$, Static pressure outlet 0 Pa Case 2: Given in Table 3.2 Case 3: $k - \epsilon$, Static pressure outlet 0 Pa

Table 3.2: List of simulations performed on Case 2.

Run Nr.	Elements in runner (mill)	Elements in draft tube (mill)	Global elements (mill)	Turbulence model	Outlet condition
01	3.3	1.0	7.52	SST	Static Pressure 113 kPa
02	9.15	1.0	13.38	SST	Static Pressure 113 kPa
03	11.76	1.0	15.98	SST	Static Pressure 113 kPa
04	11.76	3.33	18.31	SST	Static Pressure 113 kPa
05	3.3	1.0	7.52	SST	Static Pressure 0 Pa
06	3.3	1.0	7.52	SST	Avg. Static Pressure 0 Pa
07	3.3	1.0	7.52	$k - \epsilon$	Static Pressure 0 Pa
08	9.15	1.0	13.38	$k - \epsilon$	Static Pressure 0 Pa
09	11.76	1.0	15.98	$k - \epsilon$	Static Pressure 0 Pa
10	11.76	3.33	18.31	$k - \epsilon$	Static Pressure 0 Pa
11	11.76	12.16	26.37	$k - \epsilon$	Static Pressure 0 Pa
12	3.3	1.0	7.52	$k - \epsilon$	Opening 0 Pa

Results for all simulations described in this section, is presented and discussed in Section 4.1.1.

3.2 Mesh

Based on the results, discussed in Section 4.1.2, it was decided to proceed with Case 2, i.e. no volute only guide vane ring and full draft tube.

At an early stage of this thesis, it was attempted to use all the meshes from the first Francis-99 workshop [29]. A considerable amount of time was spent trying to make changes to these files, e.g. altering the number of elements along a line. These files were constructed with an old version of the ANSYS CAD module called ICEM. Attempts on alteration using a newer version of ICEM 19.1, resulted in the program not responding and had to be closed. It was decided to proceed to another solution.

The draft tube mesh is an altered mesh from the first workshop. The inlet of the draft tube was made conical to better simulate the runner cone. This was done using ICEM 19.1 and is shown in Fig. 3.4 (a). Blocking and inflation layer was created in order to retain good element quality and y^+ values (see Appendix A.4). The runner mesh was made in TurboGrid using curve files extracted from the geometry for the first workshop and provided by Igor Iliev. This mesh was checked for quality and imported to CFX, see Appendix A.4.

A previous master student, Hallén [61], provided the guide vane geometry complete with blocking and mesh. However, this produced a bad mesh quality and was difficult to change guide vane angle. For that reason, it was decided to extract curve files from this geometry in ICEM. The curve files were extracted by creating points orderly around a constant height of the guide vane. This is illustrated in Fig. 3.4 (b). Then create a text file of the coordinates of those points which had to be in perfect order; otherwise, it would not work. These text files for guide vane blade, hub, and shroud were imported to TurboGrid to create the mesh. 11 different meshes were created for guide vane angles in the range of $\alpha = [4^\circ, 14^\circ]$. The mesh was then checked for element quality and then exported for further use in CFX. An example of this mesh quality is shown in Appendix A.4. All domains were made with hexahedral element type.

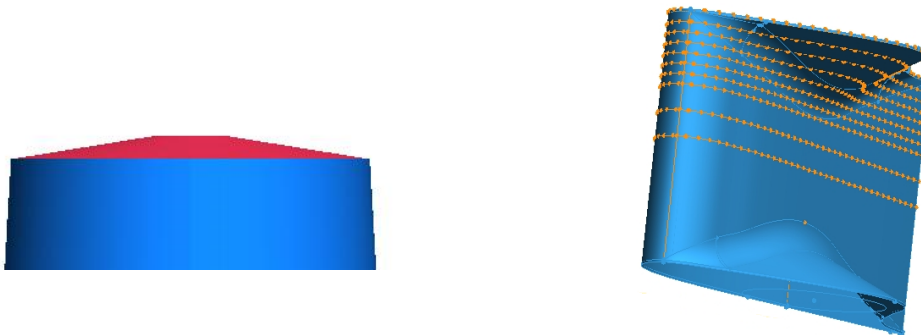


Figure 3.4: (a) Draft tube inlet with conic form. (b) Extracting points from guide vane.

3.3 Simulation setup

No change in any parameter of interest was seen after 3500 iterations when conducting mesh independence study (set to 5000 iterations). All simulations were conducted using double-precision in order to reduce computer round-off errors. The solution parameters used for performing the numerical simulations are shown in Table 3.3.

Table 3.3: System setup for all simulations.

Parameter	Description
Analysis type	Steady-state
Interfaces	Frozen rotor; discretization type-GGI
Fluid	Incompressible Newtonian fluid; water properties updated with actual density and viscosity
Boundary conditions	Inlet: total pressure inlet with direction, $P_{1,tot} = 231250$ [Pa] $\approx 12.05m$ net head Turbulence intensity 5% Outlet: Static pressure Reference pressure: 0 Pa Wall: No slip
Discretization and solution controls	Advection scheme: High resolution Turbulence numeric: High resolution
Turbulence models	Standard $k - \epsilon$, with scalable wall function
Convergence control	rms of pressure, mass-momentum, and turbulent parameters $\leq 10E-5$
Physical timescale	Auto timescale Conservative
Run type	Intel MPI Distributed Parallel: 8 nodes with 16 cores per node (see Section 4.3)
Total run for GCI	PL (GV opening 7°): $n = 188$ rpm, $n = 244$ rpm and $n = 299$ rpm BEP (GV opening 9°): $n = 320$ rpm

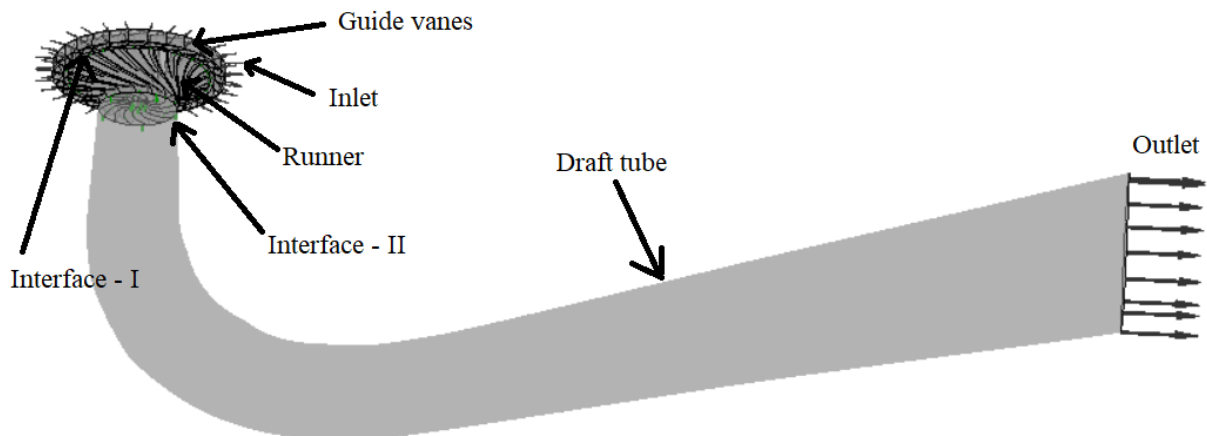


Figure 3.5: Computational domain of the model Francis turbine with two interfaces namely guide vane to runner (interface-I) and runner to draft tube (interface-II). Made similar to [31].

All meshes were connected with Frozen rotor interface between the stationary and the rotating domain. The frozen rotor interface works so that the frame of reference is changed, but the relative orientation of the components across the interface is fixed. This model produces a steady-state solution to the multiple frame of reference problem, with some account of the interaction between the two frames. These interfaces, together with the boundary conditions, are shown in Fig. 3.5.

3.4 Turbulence models

Three turbulence models have been tested in this master thesis, the $k - \varepsilon$ -model, RNG $k - \varepsilon$ -model, and the Shear Stress Transport model (SST). For the same turbine as this thesis, the model turbine installed at the Waterpower Laboratory at NTNU, Trivedi et al. [31] conducted a numerical study where they used the same two turbulence models, namely SST and $k - \varepsilon$. They found that $k - \varepsilon$ was better at estimating the hydraulic efficiency with about $\sim 1\%$. Another study on the same turbine, the Francis-99, from Yaping et al. [62] compared the standard $k - \varepsilon$ turbulence model to the SST model with different outlet boundary conditions. They found that the differences between the experimental and numerical efficiency, head and torque simulated by standard $k - \varepsilon$ turbulence model is smaller than that simulated by the SST turbulence model. Hence, the $k - \varepsilon$ model could better predict steady-state efficiency. They concluded that: «the unstable flow such as impact, flow separation and vortex may cause the torque calculation inaccuracy in the numerical simulation, which leads to numerical efficiency greater than the experimental data.» Again, on the same turbine, Jošt et al. [64] carried out a numerical study where they used SST, standard $k - \varepsilon$ and zonal large-eddy-simulation (ZLES) with different inlet conditions and solvers in order to estimate the efficiency at three operating points. They found that the efficiency, calculated with CFX, yielded good agreement with the use of $k - \varepsilon$ model. However, this was only so because both head and torque were wrong with about the same.

The selection of turbulence models for this master thesis was made from the basis of these studies. Since it is the same turbine in all three studies, it is easy to compare with the results of this thesis. Other, more advanced, turbulence models have been studied. However, these are more computational heavy and are more suited to capture transient flow [22]. All three turbulence models used in this master thesis is described in Sharenet [65].

3.5 Boundary conditions

In addition to choosing interface and turbulence model, different boundary conditions have been tested in order to look at the effect of these. The pressure at the outlet was set equal to the measured pressure from experiments $P_{out} = 113kPa$.

As well as outlet condition, it is necessary to prescribe a proper inlet condition. Tests were conducted in the project thesis (see Section 3.1) with mass flow inlet condition. However, when designing a new turbine, the flow rate corresponding to a certain guide vane opening is not known in advance. Therefore, we want to know how accurate prediction is when a value of head is input data, and flow rate is the output of the numerical simulation. For that reason, numerical simulations were conducted with total pressure at the inlet. In this case, head becomes the input data, while a value of flow rate is a result of numerical simulation [64]. Total pressure inlet and static pressure outlet are very sensitive to initial guess. Therefore, the median pressure from experiments was applied. The total pressure inlet was set to $P_{1,tot} = 231\ 250$ [Pa], which results in $\approx 12.05m$ net head.

No slip condition was applied at the walls of all domains. This means that the velocity along the wall is zero in all three directions, i.e. $u = v = w = 0$.

3.6 Software and hardware

The CFD simulations for Section 3.1 were carried out with ANSYS CFX version 19.1. All steady-state simulations were run on an Intel(R) Core(TM) i7-4770 CPU @ 3.40GHz clock speed, 3401 Mhz, 4 Cores, 8 Logical Processors and 32 GB RAM.

The rest of the simulations were executed on two different high-performance computers (HPC); Idun and Vilje.

3.6.1 Idun

Idun is a cluster at NTNU used for rapid testing and prototyping of HPC software. It consists of 25 computing nodes with type Intel Xeon E5-2630 v4 CPU @ 2.2/ 3.1GHz clock speed, 10 cores, 20 Logical Processors and 128 GB RAM. In addition, it has 8 nodes with Intel Xeon E5-6132 v5 CPU @ 2.6/3.7GHz clock speed, 14 cores, 28 Logical Processors and 192 GB RAM. All together 33 computing nodes (on WORKQ partition). See [66] for more information. Idun uses Slurm Workload Manager to manage the provided resources and to schedule jobs on these resources. A slurm script (.sh) must be sent to the Linux cluster in order to run jobs. An example of this script which was used in this thesis is given in Appendix A.10.

3.6.2 Vilje

Vilje is a supercomputer at NTNU used for research in a broad range of topics by several universities and research institutes in Norway. It consists of 1404 computing nodes with type Intel Xeon E5-2670 CPU @ 2.6/ 3.3GHz clock speed, 2x 8 cores, 16 (dual eight-core) and 32 GB RAM/node. See [67] for more information. Vilje uses Portable Batch System (PBS) for running jobs. A PBS script (.pbs) have to be sent to the Linux supercomputer in order to run jobs. An example of this script which was used in this thesis is given in Appendix A.11.

3.7 Mesh independence study

It is common to use BEP to evaluate mesh independence, e.g. [31, 68, 69]. However, this is a highly stable operating point which could lead to an artificially low grid convergence uncertainty. At part load, the flow characteristics in the runner and draft tube are highly unstable [13]. Therefore, two different loads were used to perform the mesh independence study; part load (PL), i.e. guide vane opening of $\alpha = 7^\circ$, and BEP.

From Celik et al. [70], the recommended procedure for estimation of uncertainty due to discretization in CFD has been used to evaluate the mesh independence. In accordance with these guidelines, the application of this procedure to the case at hand is presented in this section. The results from this study are presented in Section 4.2.

3.7.1 Iterative convergence

In order to decrease the iterative convergence error of the CFD simulations, the time history of the RMS residuals of pressure, mass, and momentum were analyzed in more detail. To improve the validity of the mesh independence study, a selection of three different operating points was applied. Using the same mesh with guide vane opening of $\alpha = 7^\circ$, the runner speed was varied. All simulations ran for 5000 iterations to ensure iterative convergence. Figure 3.6 presents the convergence history of the RMS values for runner speeds $n = 188$ [rpm], $n = 244$ [rpm], and $n = 299$ [rpm]. It turns out that the residuals vary some depending on runner speed. For $n = 299$, the highest RMS residual where 1.3×10^{-4} for U-velocity momentum. Whereas for $n = 244$ all residuals were well below 2×10^{-7} .

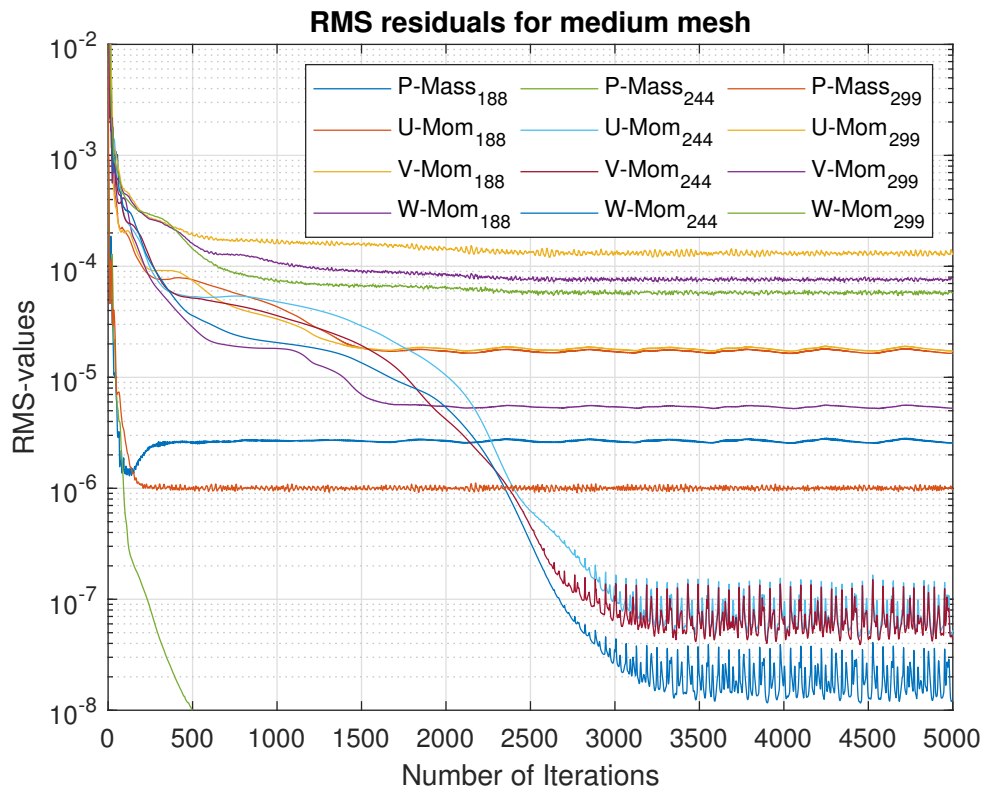


Figure 3.6: RMS residuals for pressure, mass, and momentum for three different runner speeds; $n = 188$ [rpm], $n = 244$ [rpm], and $n = 299$ [rpm].

As well as checking convergence for the residuals, it is important to check the convergence for the parameter of interest. To this specific study, it is the hydraulic efficiency, η . The iterative history for efficiency is presented in Fig. 3.7 for $n = 188$ [rpm] and $n = 244$ [rpm] ($n = 299$ [rpm] was intentionally left out but showed the same trend as for $n = 188$ [rpm]). The residuals from Fig. 3.6 is somewhat reflected in Fig. 3.7. The relatively high and oscillating residuals for $n = 188$ [rpm] may cause oscillating behavior in efficiency. However, attention should be paid to the y-axis scaling in Fig. 3.7. The amplitude is so little, that is practical to consider it converged. The residuals for BEP were well below 10^{-5} , and efficiency converged after only 500 iterations.

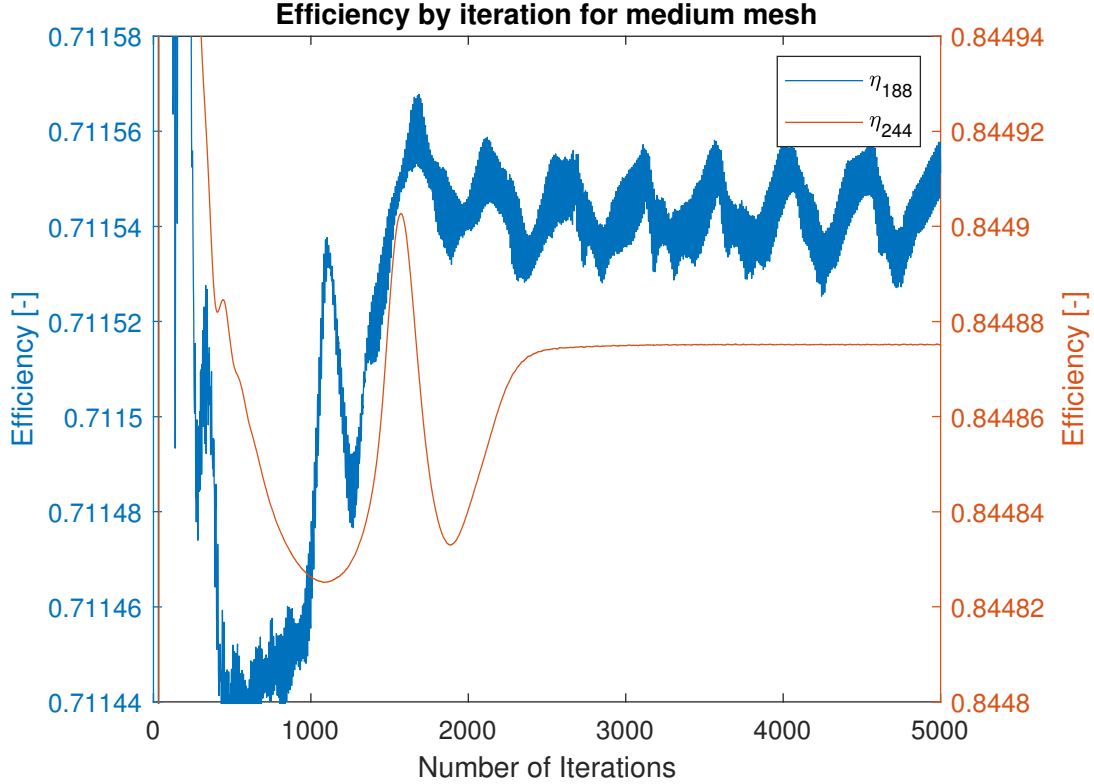


Figure 3.7: Iteration history of efficiency for two runner speeds; $n = 188$ [rpm] and $n = 244$ [rpm]. Pay attention to the scale of y-axis!

This shows that the simulation results should be analyzed carefully. The RMS residuals were checked for every following simulation. Convergence for the parameter of interest is also necessary. Looking at η_{188} in Fig. 3.7, if oscillating behavior occurs, an average of the last 500 iterations were calculated. From Fig. 3.7 it was decided to set the iterative convergence at 3500 iterations, to ensure convergence for the following simulation. Reducing the number of iterations would linearly decrease the simulation time, however, to have reliable results it is safer to stay on the conservative side.

3.7.2 Grid Convergence Index

The grid convergence index (GCI) [70] is an industry-recognized method for assessing mesh quality. The procedure for the estimation of the discretization error according to this method was summarized by Celik et al. [70] but will be briefly explained here.

First, three meshes were created to fulfill the criteria for the refinement factor $r = h_{coarse}/h_{fine}$, which desirable, should be greater than 1.3. The representative size factor were $h_3 = 6.16$ mm, $h_2 = 4.58$ mm, and $h_1 = 3.47$ mm, for the coarse, medium, and fine mesh, respectively. Inserting [70, eq. 2] into the definition of r , it is possible to approximate (assuming constant volume, V) the number of elements, N ;

$$h = \left[\frac{1}{N} \sum_{i=1}^N (\Delta V_i) \right]^{\frac{1}{3}} \stackrel{V=const.}{\implies} N_{fine} = r^3 N_{coarse} \stackrel{r=1.3}{\implies} N_{fine} \approx 2.2 N_{coarse}. \quad (23)$$

This was the method that was applied to make the three mesh sizes. Refining by global cell size and keeping good mesh quality, the three different mesh sizes were made. The information about the different mesh, including mesh quality, is presented in Table 3.4.

Analyzing the results from the three simulations, one may calculate the grid convergence index (GCI) defined as,

$$GCI_{fine}^{21} = \frac{1.25e_a^{21}}{r_{21}^p - 1}, \quad (24)$$

where 1.25 is the safety factor, e_a is the approximate relative error, p is the apparent order, and index 1, 2 are the fine and medium mesh respectively. For more details, see [70].

Table 3.4: Grid densities used in grid scaling tests

Grid type	N_1	N_2	N_3
Draft tube	1,914,614	851,190	378,082
Runner	18,360,540	8,049,240	3,572,640
Guide vane	6,725,600	2,891,476	884,100
Total elements (million)	27.00	11.79	4.83
Element angle [°] (average)	75.67	75.39	74.92
Expansion factor (average)	1.24	1.37	3.38
Element aspect ratio	5.67	5.30	6.56
Y^+ (area average at all domains)	117.74	133.06	109.02

GCI was calculated for the parameter of interest, ϕ , being efficiency, torque, and discharge. Due to computational cost, and GCI being low, it was decided to continue using the medium grid size, N_2 , for the following simulations. More details are presented in the results Section 4.2.

4 Results and Discussion

4.1 Geometry Simplification

This section presents the results for what geometry simplifications can be done to reduce computational cost without loss in accuracy.

4.1.1 Reduced models

The content of this section comes from earlier work on the author's project thesis [32].

All the parameters of interest in (16) like efficiency, head, and torque were estimated in CFX-Pre using the expression language CEL [71]. These expressions are listed in the equations below:

$$H = \frac{\Delta P}{\rho g} + \frac{v_1^2 - v_2^2}{2g} + (z_1 - z_2), \quad [m] \quad (25)$$

$$T = T_{FullBlade} + T_{SplitterBlade} + T_{Hub} + T_{Shroud}, \quad (26)$$

where v_1 and v_2 are the velocities at the inlet and outlet respectively. Water density is expressed as ρ , and the gravitational acceleration is g . The last term describes the difference in elevation from inlet to outlet. The value of the pressure (ΔP) is acquired by the differential pressure, as shown in Fig. 2.4. The total torque T is the sum of torque from runner blades, hub, and shroud. To compare the absolute values of the numerical results compared to experimental data, we define the difference (Δ) calculated as, $\Delta X = X_{numerical} - X_{experimental}$, where X is the variable of interest. E.g. efficiency;

$$\Delta \eta = \eta_{numerical} - \eta_{experimental}. \quad (27)$$

The reduced models, Case 1-3, presented in Section 3.1 has been analyzed in order to reduce computational cost without sacrifice accuracy in prediction of efficiency. All the simulations where the standard $k - \epsilon$ model was used, met the convergence criteria, except for Case 3. The other simulations, using SST, ran for 1000 iterations, except for Case 3 which were stopped after 704 iterations. When CFX sense fluid going across a boundary in both directions, it creates an artificial wall to prevent backflow. This happened to all SST simulations, which makes these simulations more unreliable, see Appendix A.9. However, the efficiency was quite similar using both turbulence models. The relative speedup was calculated for the runs that managed to reach the convergence criteria. Relative speedup is defined as CPU-time for the longest run, i.e. Case 2 #11, divided by CPU-time for a given run. The fastest relative speedup was 7.78, for the opening-type run #12. For all simulations, CPU-time and number of iterations are given in Table 4.1.

Efficiency, given by (16), is proportional to τ/H ; therefore, it is important to look at the individual parameters to get a better understanding of the simulated efficiency. The smallest deviation in head was observed with the coarsest mesh with $k - \epsilon$ model; here, the difference was 1.11 meter higher than experiments. The largest deviation in head was the same for all SST simulations, with 1.76m over prediction. In the torque parameter, the smallest discrepancy was at

35.13 Nm higher than experiments, for run #08. In the efficiency, the most important parameter of this thesis, the lowest discrepancy compared to experiments were 2.89% in run #01. This was the coarsest mesh, with the SST turbulence model, and showed large deviations in both head and torque. However, the percentage deviation was similar in both parameters and resulted in the best estimation of efficiency. The best simulation with $k - \epsilon$ model was both run #10 and #11 with relatively fine mesh. To make a case for mesh independence, different mesh sizes were tested. Little variation in head, torque and efficiency were seen after the second grid refinement of the runner, when using $k - \epsilon$ model (i.e. run # 07-11). Since the last simulation (#11), with 26.37 million elements, gave no different result in efficiency than the second grid refinement (# 08 with 13.38 million elements) it could be argued that one has reached a mesh independent solution. However, the grid convergence method (GCI) method is more acceptable and a recommended method that has been evaluated over several hundred CFD cases and is considered a standard amongst CFD users [70]. All the results from the simulations of Case 2 are given in Table 4.3.

Table 4.1: Computation time and relative speedup.

Simulation speed table					
Run Nr.	CPU seconds	Iterations	Converged [Y/N]	Mesh size factor	Relative speedup
Case 1:	6.352E+05	314	Y	1.26	2.67
Case 2:					
01	5.858E+05	1000	N	3.51	-
02	1.118E+06	1000	N	1.97	-
03	1.422E+06	1000	N	1.65	-
04	1.660E+06	1000	N	1.44	-
05	5.939E+05	1000	N	3.51	-
06	5.952E+05	1000	N	3.51	-
07	2.293E+05	395	Y	3.51	7.65
08	3.724E+05	329	Y	1.97	4.71
09	4.225E+05	295	Y	1.65	4.15
10	6.118E+05	360	Y	1.44	2.87
11	1.753E+06	322	Y	1.0	1.0
12	2.254E+05	397	Y	3.51	7.78
Case 3:	1.260E+06	704	N (Stopped)	1.55	-

Case 1, the full model with spiral case, converged after 314 iterations. The results from this case showed a 1.16m deviation in head, compared with experiments. It also showed a 35.2 Nm discrepancy in torque. This corresponds to a 3.66% difference in efficiency, which makes it more accurate than Case 3 to predict efficiency. Case 3, the short draft tube no volute case, scored the poorest off all simulations in this thesis. The fact that it did not converge, together with the highest deviation in efficiency of 5.82% made it the most unreliable of all the simulations and was stopped after 704 iterations. This makes Case 2 the most accurate model for simulating efficiency. The results for Case 1 and 3 are presented in Table 4.2.

So, what happens when using the same mesh and setup (see Table 3.1) on another operating point? To answer this, it has been simulated another problematic operating point, namely guide vane opening of $\alpha = 7^\circ$. This is around the point where we can observe the vortex rope for-

mation in the draft tube [30]. Looking at the results from this simulation in Table 4.2, one can see an even better estimation of the efficiency. With only 0.84% underprediction of efficiency compared to experiment for this operating point, one can argue that the «calibration of the numerical method» made at $\alpha = 4^\circ$ proved itself effective in a similar problematic operating point. However, it remains to see if this holds true for the whole hill chart.

Table 4.2: Result from simulations of Case 1 and Case 3 $\alpha = 4^\circ$ and the case of $\alpha = 7^\circ$.

Case Nr.	Head [m]	Torque [Nm]	η [%]	$\Delta\eta$ [%]
Case 1	13.39	282.33	88.17	3.66
Case 3	13.06	282.01	90.33	5.82
Case $\alpha = 7^\circ$				
Experiments:	12.02263028	655.7504902	83.0634938	-
Simulations:	12.97	700.51	82.22	-0.84

Table 4.3: Result from simulations of $\alpha = 4^\circ$. Corresponds to Table 4.3. $\Delta\eta$ is the difference in efficiency from simulation to experiments [30].

Experiments				
	Head [m]	Torque [Nm]	η [%]	
	12.23310356	247.1170519	84.5136798	
Simulations				
Run Nr.	Head [m]	Torque [Nm]	η [%]	$\Delta\eta$ [%]
01	13.99	292.39	87.40	2.89
02	13.99	293.07	87.64	3.12
03	13.99	293.51	87.73	3.22
04	13.99	293.53	87.75	3.24
05	13.99	292.72	87.50	2.99
06	13.99	292.72	87.49	2.98
07	13.34	282.38	88.45	3.93
08	13.36	282.25	88.38	3.86
09	13.36	282.30	88.37	3.86
10	13.36	282.31	88.38	3.87
11	13.36	282.31	88.38	3.87
12	13.36	282.45	88.47	3.95

4.1.2 Project thesis conclusions

The three cases were simulated, using two turbulence models ($k - \varepsilon$ and SST) and four computational grids. All simulations were carried out at part load, with guide vane opening of $\alpha = 4^\circ$, except one simulation at $\alpha = 7^\circ$. The selection of these operating points was made based on them being problematic operating points due to its highly transient nature and to compare against [61]. All the simulations where the standard $k - \varepsilon$ model was used, met the convergence criteria, except for Case 3. The other simulations, using SST, ran for 1000 iterations, except for Case 3 which was stopped after 704 iterations. The $k - \varepsilon$ simulations were much faster than the simulations using SST.

The lowest difference between experimental and numerical efficiency was found using the coarsest mesh and the SST turbulence model, with a difference of 2.89%. Given that the deviation in head and torque was large compared to the efficiency, it is most likely an unreliable result. The largest discrepancy in efficiency of 3.95% was found using the $k - \varepsilon$ turbulence model and opening-type boundary condition. Using different mesh sizes, it was observed the impact it had on the numerical simulations. Using the $k - \varepsilon$ turbulence model gave the most reliable result for this comparison, and little variation in head, torque and efficiency was seen after the second grid refinement of the runner. It was observed no difference in head, torque, and efficiency from the simulation of two finest meshes. However, the grid convergence method (GCI) method is more acceptable and a recommended method for studying mesh independence.

Given this insight from the project thesis, including the fact that spiral case mesh was hard to manipulate (see Section 3.2), it was decided to proceed with Case 2, i.e. no volute only guide vane ring and full draft tube. The $k - \varepsilon$ model proved to give more reliable results and was therefore prioritized (see Section 4.4).

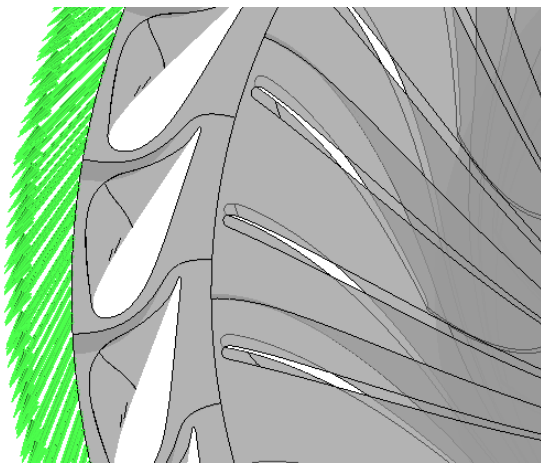
4.1.3 Sensitivity of guide vane inlet angle

Proceeding with Case 2, it was important investigate into the prescribed angled flow field into the guide vane inlet. This angle was decided based on the averaged flow vector from the simulation using the full model, i.e. Case 1. It is necessary to model the flow angle after leaving the stay vanes to decrease geometry modeling error. Figure 4.1(a) displays this boundary vector prescribed at the guide vane inlet. To quantify this angle's influence on the result, an «angle sensitivity study» was conducted. Presented in Fig. 4.1(b), five simulations with angles $27.269^\circ \pm 2^\circ$ were performed using the boundary conditions in Table 3.3. It turns out that the impact is small, varying with only 0.028% in efficiency (η) from highest to lowest value. Knowing this, a ballpark estimate might be enough to model the flow inlet angle.

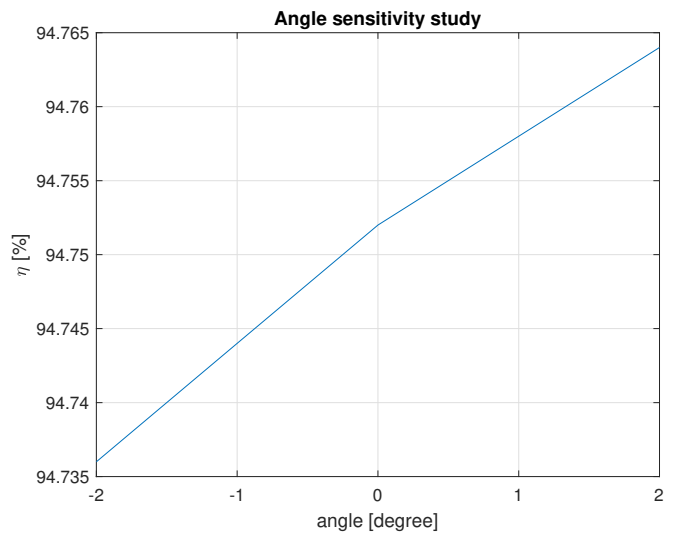
4.1.4 Simplified guide vane

The last geometry simplification tested was the simplification of the guide vane geometry. Using only one symmetric profile gave better mesh quality (see Appendix A.4), considering min- and max face angle, which leads to faster simulations. The original geometry is seen in Fig. 3.4, whereas the simplified geometry is displayed in Fig. 4.2. Simulation of the simplified guide vane was around 50% faster than the other. However, the difference in efficiency (27) was

about 0.6% higher for the simplified guide vane. To reduce the geometry modeling error, it was decided to continue with the original guide vane.



(a) Constant velocity profile at the inlet.



(b) Constant velocity profile at the inlet.

Figure 4.1: Modelling stay vane angle on guide vane boundary.

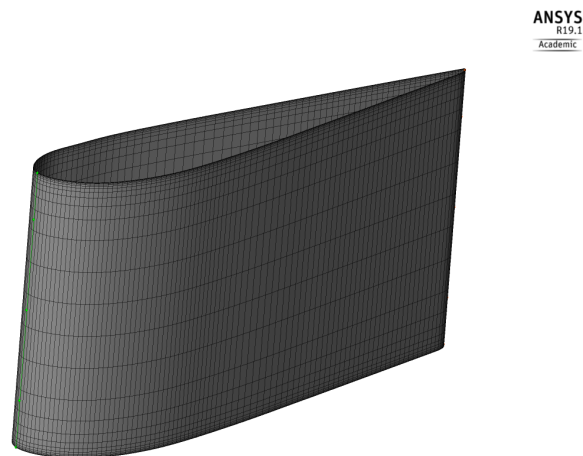


Figure 4.2: Simplified guide vane.

4.2 Mesh independence study

This section presents the results for the mesh independence study, where the uncertainty due to discretization is estimated and reported.

To estimate the error due to discretization, as suggested by Celik et al. [70], discharge, torque, and efficiency of the turbine were simulated using $k - \varepsilon$ turbulence model for all three meshes in the mesh independence study. The computed flow parameters are tabulated in Table 4.4-4.7.

Table 4.4: $n_{ED} \approx 0.13$, GV: 7°

Parameter	η [%]	T [Nm]	Q [m^3/s]
ϕ_1	84.600	618.96	0.16179
ϕ_2	84.488	615.02	0.16097
ϕ_3	83.940	586.76	0.15456
ϕ_{ext}^{21}	84.630	619.73	0.16194
e_a^{21} [%]	0.132	0.637	0.507
e_{ext}^{21} [%]	0.041	0.125	0.090
GCI_{fine}^{21} [%]	0.051	0.156	0.113
GCI_{med}^{32} [%]	0.217	0.958	0.750

Table 4.5: $n_{ED} \approx 0.10$, GV: 7°

Parameter	η [%]	T [Nm]	Q [m^3/s]
ϕ_1	71.289	716.99	0.17163
ϕ_2	71.155	711.57	0.17650
ϕ_3	70.570	676.27	0.16350
ϕ_{ext}^{21}	71.34	718.18	0.16846
e_a^{21} [%]	0.138	0.756	2.838
e_{ext}^{21} [%]	0.067	0.165	1.882
GCI_{fine}^{21} [%]	0.084	0.207	2.309
GCI_{med}^{32} [%]	0.319	1.161	5.347

Table 4.6: $n_{ED} \approx 0.16$, GV: 7°

Parameter	η [%]	T [Nm]	Q [m^3/s]
ϕ_1	92.495	511.07	0.14956
ϕ_2	92.434	508.62	0.14894
ϕ_3	91.961	486.40	0.14315
ϕ_{ext}^{21}	92.506	511.44	0.14965
e_a^{21} [%]	0.056	0.479	0.415
e_{ext}^{21} [%]	0.012	0.073	0.061
GCI_{fine}^{21} [%]	0.015	0.091	0.076
GCI_{med}^{32} [%]	0.097	0.693	0.597

Table 4.7: $n_{ED} \approx 0.17$, BEP

Parameter	η [%]	T [Nm]	Q [m^3/s]
ϕ_1	94.586	614.50	0.18446
ϕ_2	94.506	610.32	0.18335
ϕ_3	94.050	588.35	0.17758
ϕ_{ext}^{21}	94.605	615.58	0.18475
e_a^{21} [%]	0.035	0.630	0.602
e_{ext}^{21} [%]	0.020	0.176	0.158
GCI_{fine}^{21} [%]	0.025	0.220	0.197
GCI_{med}^{32} [%]	0.131	1.078	0.955

Here ϕ and ϕ_{ext} is a variable critical to the conclusions being reported and the extrapolated value, respectively. The subscript 1, 2 and 3 denotes the fine, medium, and coarse mesh, respectively. GCI_{fine}^{21} is the fine-grid convergence index and is a measure of discretization error of the mesh. The apparent order, p , of the solution ranged from 3.37 to 7.44. The different mesh sizes were made according to [70], with refinement factor $r > 1.3$. For Table 4.4-4.6, $r_{21} = 1.318$ and $r_{32} = 1.346$. For Table 4.7, $r_{21} = 1.312$ and $r_{32} = 1.326$. Presented in Table 4.5; the highest estimated numerical uncertainties in the hydraulic efficiencies were $\approx 0.32\%$ and ≈ 0.08 with fine and medium grid densities, respectively. In general, the medium mesh showed lower uncertainties, particularly on hydraulic efficiency, compared to torque and discharge. The maximum uncertainty was discharge (Q) at 5.35% with $n_{ED} \approx 0.10$ and GV angle 7° , using medium mesh. For the fine grid, the maximum uncertainty was 2.3%, on the same operating point.

Jakobsen et al. [60], studied the computational effort of CFD simulations of the Francis-99 runner. He found a close linear speed-up with the mesh size. Table 4.8 shows that the relative speed-up does not quite follow the mesh size factor as it did in [60]. Still, the computational cost may be reduced by more than two times, reducing mesh from fine to medium.

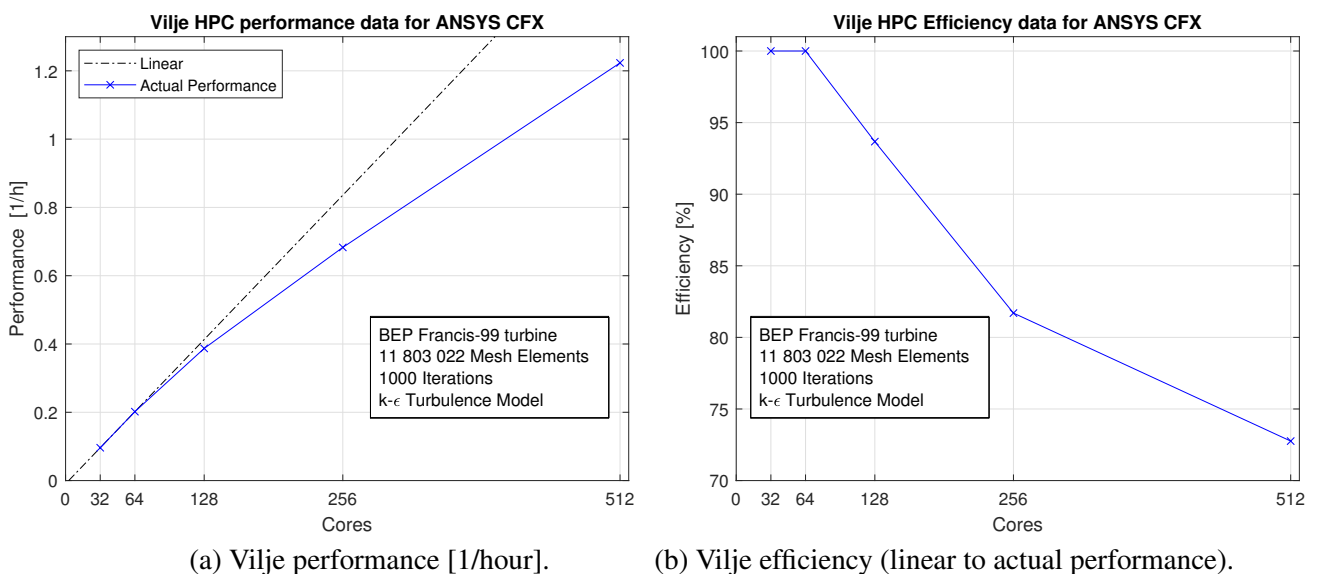
The GCI_{fine}^{21} was very low compared to the GCI_{med}^{32} . The converged solution with the medium grid was used for further simulations at different operating conditions, considering how computationally demanding the fine grid was. However, the GCI error is still quite low.

Table 4.8: Speed-up for mesh sizes at GVO 7° and $n_{ED} = 0.13$.

Grid type	Global number of nodes	Mesh size factor	Relative speedup
N_1	27,000,754	1	1
N_2	11,791,906	2.29	2.24
N_3	4,834,822	5.58	3.70

4.3 High-performance computing (HPC)

The supercomputer, Vilje, were used for most of the simulations done in this thesis (see Section 3.6.2). When using HPC, it is important to discuss the issue of scalability. The concept of scalability connotes the ability of a system to work efficiently with a growing amount of work by adding resources to the system [72]. The theoretical limits to scalability are described by Amdahl's law [73], which gives the speedup in latency of the task execution with a fixed workload, that can be expected of a system whose resources are improved. A way to quantify the scalability, as well as the performance of a given software, is to perform a benchmark test. Figure 4.3(a) presents the benchmark test performed on Vilje using ANSYS CFX. Performance is defined here as $1/\text{simulation time [1/hr]}$, whereas the efficiency in Fig. 4.3(b) is defined as $(1 - (P_l - P_a)/P_l) \times 100$ where P_l and P_a is the linear and actual performance, respectively. This benchmark test were conducted using the same simulation, i.e. same operating point (BEP), mesh size, and simulation setup. By doubling the number of compute nodes (n), i.e. $n \times 16$ cores, the simulation time compared to linear scaling. Simulation efficiency, is presented in Fig. 4.3(a). From this benchmark, one sees almost a linear drop in simulation efficiency between 64 and 256 cores. The relative speedup from 64 to 128 cores was 1.92, whereas from 128 to 256 cores gave 1.76 relative speedup. To achieve high performance, as well as a reasonable efficiency, it was decided to do most simulations using 128 cores (8 nodes).



(a) Vilje performance [1/hour].

(b) Vilje efficiency (linear to actual performance).

Figure 4.3: High-performance computing data for Vilje.

4.4 Different turbulence models

As discussed in Section 4.4 different turbulence models have been used in several studies to address its accuracy to predict the hydraulic efficiency. A more extensive examination of the accuracy and speed of different turbulence models is presented in this section.

Simulations of 25 different operating points using three different turbulence models were conducted to get a quantitative foundation for comparison. These turbulence models were; the standard $k - \epsilon$ model, RNG $k - \epsilon$ model, and the SST model. The simulations lied within the range of $n_{ED} = [0.16, 0.20]$ and $Q_{ED} = [0.11, 0.19]$, in order to capture the innermost efficiency isocurve where the BEP exist. Simulation setup and mesh (medium size) were kept constant in order to extract the influence of the turbulence models only. It is important to recognize that the different turbulence models have different demand for Y^+ values, SST requiring a value of $Y^+ < 1$ and $k - \epsilon$ having $30 < Y^+ < 300$ (outside the buffer layer) [74]. Figure 4.4 presents this isocurve made form interpolation of the simulations results. Visually, it is little difference in the shape of the three curves. The absolute value, however, is more prominent and shows that the RNG $k - \epsilon$ model and SST predicts higher efficiency than the standard $k - \epsilon$ model. From (27), the average difference in hydraulic efficiency were 2.73%, 3.26%, and 3.10% for the standard $k - \epsilon$, RNG $k - \epsilon$, and SST turbulence model, respectively.

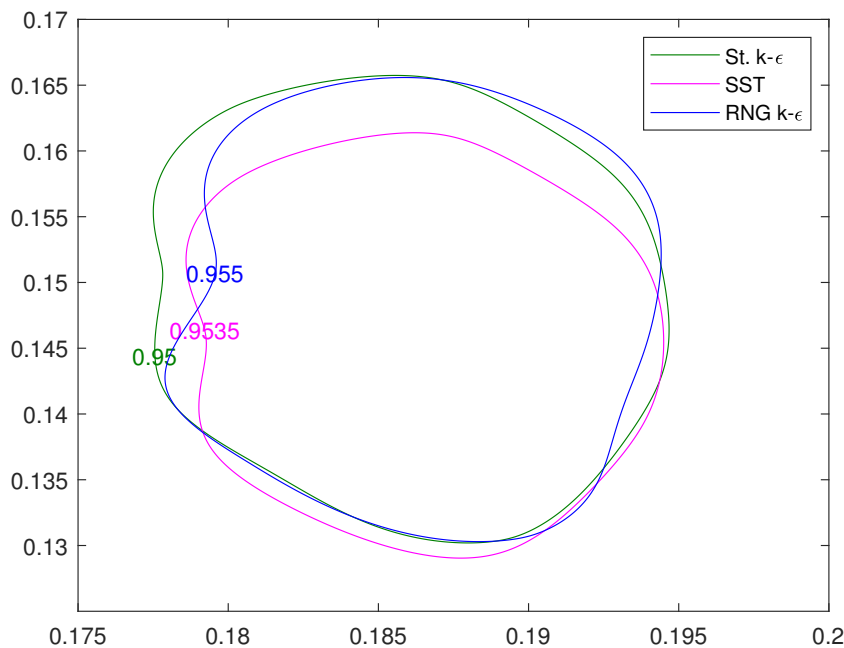


Figure 4.4: Comparison of different turbulence models.

Renormalization group (RNG) $k - \epsilon$, model is more computationally expensive than the standard $k - \epsilon$ model due to an additional term in the ϵ -equation (19). This model provides an option for modifying the turbulent viscosity, thereby cater to the effects of swirl in the flow [75]. The SST model is also more computationally heavy due to it switching from $k - \epsilon$ to $k - \omega$ [74]. The $k - \epsilon$ and SST model are both described in Section 2.5. Table 4.9 presents the average and total simulation time for the three different turbulence models. The slowest, being

the SST model, is set as a basis for the speed-up number ($= 1.0$) in Table 4.9, where speedup is the total simulation time of SST divided by total simulation time of e.g. $k - \varepsilon$. Based on $k - \varepsilon$ being more accurate and faster, it was decided to proceed using this turbulence model for creating the expanded hill chart.

Table 4.9: Evaluation of different turbulence models for reducing simulation time

Turbulence model:	Standard $k - \varepsilon$	RNG $k - \varepsilon$	SST
Average simulation time [h]	9.61	11.43	12.79
Total simulation time [h]	240.19	285.67	319.79
Speed-up	1.33	1.12	1.0

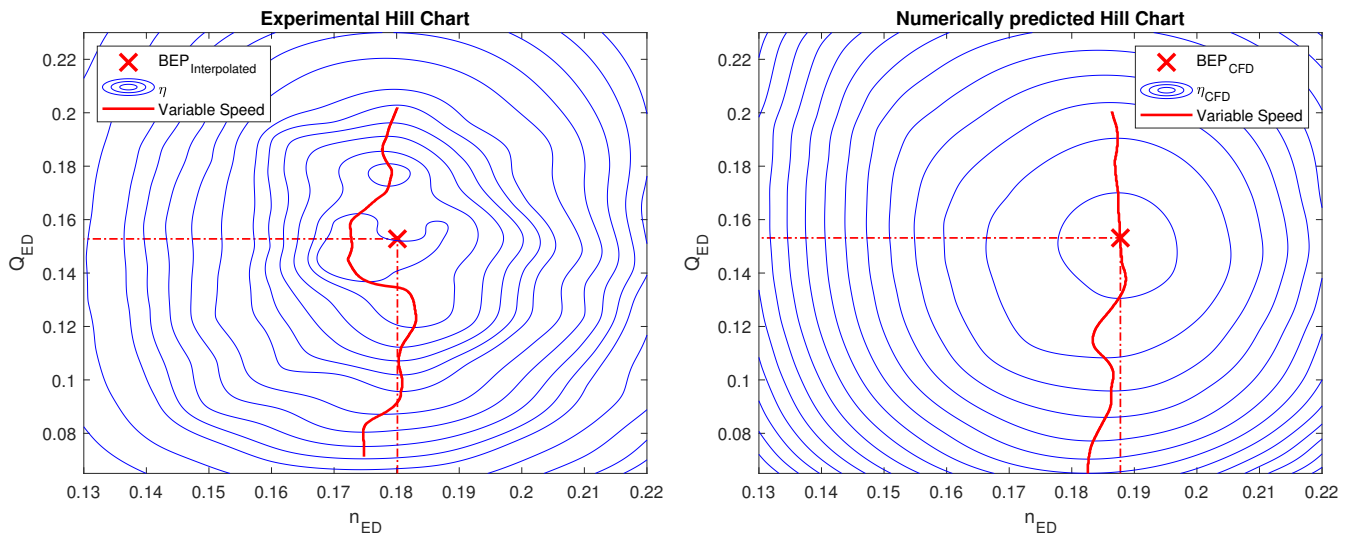
4.5 Main results

Having assessed the right geometry, mesh size, and turbulence model to achieve accurate and fast simulations, it is ready to present the main results of this master thesis. Using the medium mesh from the GCI study described in Section 4.2 and the standard $k - \varepsilon$ model, simulations for 132 operating points with 11 different guide vane angles were carried out.

These 132 operating points lied within the range of $n_{ED} = [0.12, 0.23]$ and $Q_{ED} = [0.04, 0.236]$. This range excludes the efficiency isocurves for runaway speed, i.e. zero efficiency. Operation at runaway speed is associated with high amplitude pressure fluctuation and is transient in nature. To capture the unsteady flow field in the runner, more advanced turbulence models like SAS-SST is necessary to use under these conditions [76]. Jakobsen and Holst [77] investigated the transient load change on the Francis-99 runner. A very low difference in hydraulic efficiency was observed when performing transient simulation compared to steady-state at BEP, where the transient simulation deviated the most from experimental data. Using steady-state and the setup from Table 3.3 should, therefore, be sufficiently accurate within this range of operation.

All simulations were carried out with GV opening in the range of $\alpha = [4^\circ, 14^\circ]$, and with an increment of 1° angle. These simulations were carried out using experimental values as input, i.e. exact runner speed and the average GV angle for each data set. To verify the results, head, torque, and efficiency were compared against experimental measurements given by Iliev (see Section 2.4). A reproduced hill chart from [30] is presented in Fig. 4.5(a). The red X mark the BEP, which is interpolated for the 132 experimental points. The hill chart was made using MATLAB's griddata interpolation function and contour plot, see Appendix A.8. Figure 4.5(b) shows the numerically predicted hill chart with the interpolated BEP. The red line in each plot is the efficiency-optimized variable-speed path.

To make the comparison between the experimental and the numerically predicted hill chart easier, the two are plotted on top of each other in Fig. 4.5. The experimental line is in red, and the numerical contour line is in green. Similarly, BEP is marked with red and green for experiments and CFD, respectively. Notice here, the BEP for the experiments is shifted up and to the right, i.e. higher n_{ED} and Q_{ED} . The reason being that experiments, see Section 2.4, were not conducted with an objective to locate the BEP. In order to pinpoint the location of BEP, several measurements must be conducted in a narrow $n_{ED} - Q_{ED}$ -range. These kinds of



(a) Experimental hill chart reproduced from [30]. (b) CFD hill chart with 132 operating points.

Figure 4.5: Comparison of experimental and numerically predicted hill chart.

measurements were performed by O.G. Dahlhaug, which found BEP at $n_{ED} = 0.18$, $Q_{ED} = 0.153$. The efficiency isocurves for CFD appears to be shifted to the right, the variable-speed line in Fig. 4.5 follows this trend.

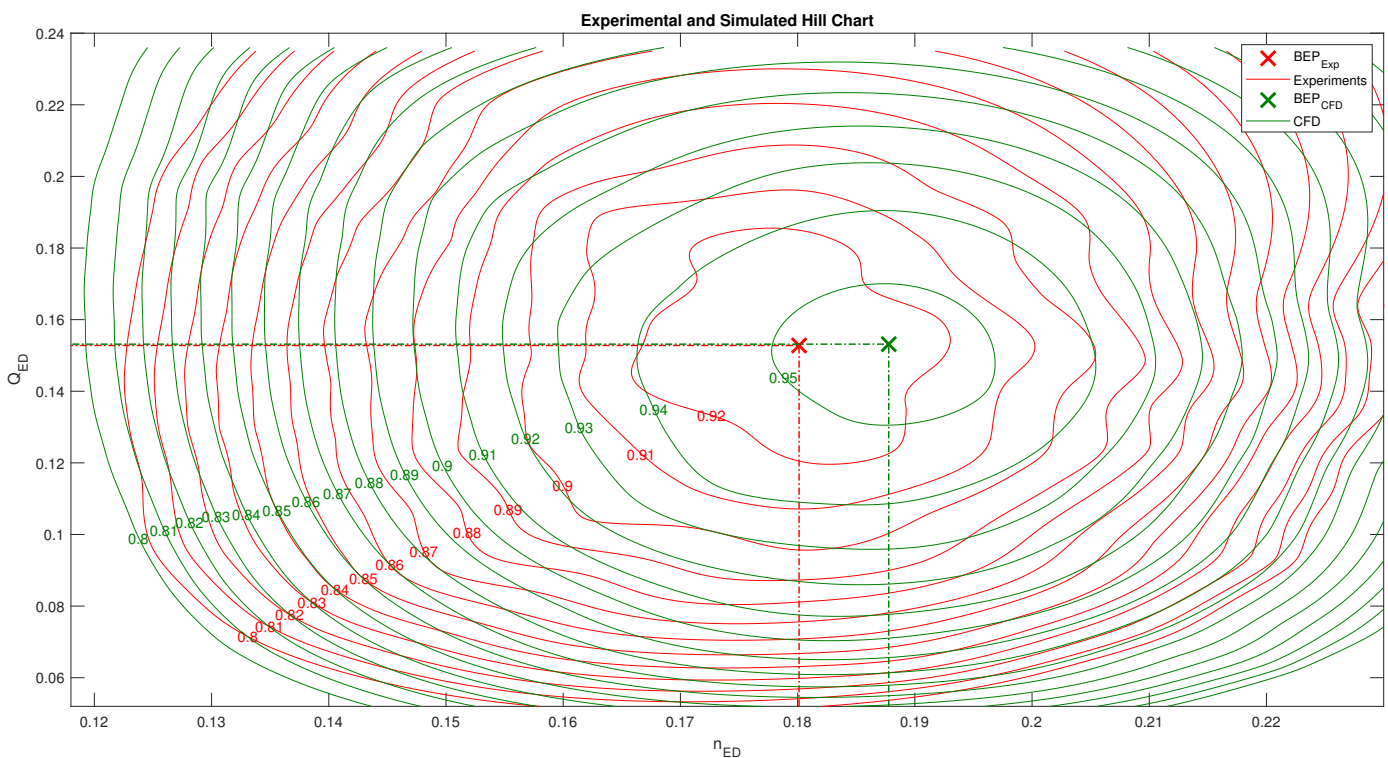


Figure 4.6: Experimental and numerically predicted hill chart on top of each other.

The hydraulic efficiency was numerically predicted with the maximum difference found at GV opening of 6° and $n = 432.5$ rpm, was calculated to be 6.93%, compared to experiments. At the lowest guide vane opening (4°), the minimum difference in efficiency was found at 0.13%, with $n = 244.4$ rpm. This is not trivial, as stated earlier, this is a highly problematic operating point

with transient flow occurring in the draft tube. It is also recognizable considering other studies on the same runner, presented in a review paper by Trivedi et al. [41], showed a much larger deviation in efficiency at part load than this study. The maximal difference in torque, found at GV opening of 14° and $n = 222.5$ rpm, was calculated to be 72.4 Nm.

Even more important than the absolute value of efficiency is getting the shape of the efficiency curve and the position of BEP. Fig. 2.3 shows that the BEP for numerical results is higher, i.e. higher efficiency, and shifted to the right in the hill chart compared to experiments. Q_{ED} matches almost exactly the experimental value, whereas the n_{ED} is off by 4.3%. The average difference in efficiency was 2.87% for the whole hill chart. Jošt et al. [64] tested both head and volume flow as input data and found that volume flow was slightly underpredicted when using head as input data. Similarly, this study underpredicted volume flow, on average, -5.6 l/s. The maximal difference in discharge, found at GV opening of 11° and $n = 241$ rpm, was calculated to be 6.5 l/s. It is worth mentioning that the imposed total pressure at the inlet $P_{1,tot}$ resulted in a head that varied only with 5.3cm from largest to smallest, whereas the head from the experimental data varied with 50.1cm correspondingly. This affects the result, and deviation, of the discharge. Even so, using total pressure inlet has been justified in Section 3.5.

A cross-section from the hill chart in Fig. 4.6 with constant $n_{ED} = 0.18$ is shown in Fig. 4.7. The constant n_{ED} -line describes the characteristics of normal operation at synchronous speed. Figure 4.7 also presents the efficiency curve for constant guide vane opening of 7° . All the efficiency plots for constant n_{ED} and GV opening is found in Appendix A.5 and Appendix A.6, respectively. Hydraulic efficiency (16), is proportional to torque divided by discharge, $\sim \tau/Q$. If torque is underpredicted by the same amount as discharge, the efficiency parameter would be artificially close to experiments, although the simulation was inaccurate. It is, therefore, important to look at these parameters individually and compare CFD against experiments. This comparison is shown in Fig. 4.7 on the second and third row in the figure. A close match between experiments and CFD can be seen in all plots in this figure. Absolute values of efficiency for CFD is greatest, compared to experiment, looking at the $n_{ED} = 0.18$ -plot. Numerical prediction of torque follows a close match to the experimental values, where CFD underpredicts. Underprediction also happens for volumetric discharge, with a larger difference for smaller GV openings. Discharge follows an almost linear trend with GV opening.

Another way of calculating the efficiency is by the Euler equation (7). A comparison between the efficiency hill chart by (16) and the Euler efficiency (7) is presented in Appendix A.7. Hardly surprising, the Euler efficiency hill chart is similarly shaped as the normal hill chart. The numerator in (7) is just another way of calculating torque times omega divided by mass flow ($T\omega_b/\dot{m}$) in (16). However, the losses in the guide vanes and draft tube are not taken into account in (7) and, therefore, the efficiency isocurves appear larger (see Appendix A.7).

4.5.1 Losses and hydraulic efficiency

To get a better grasp of the results, as well as a more fruitful discussion, this section will cover the hydraulics from a physics perspective.

According to the International Electrotechnical Commission (IEC) standard [36], the efficiency is calculated as follows;

$$\eta_{IEC} = \frac{P_m}{P_h}, \quad (28)$$

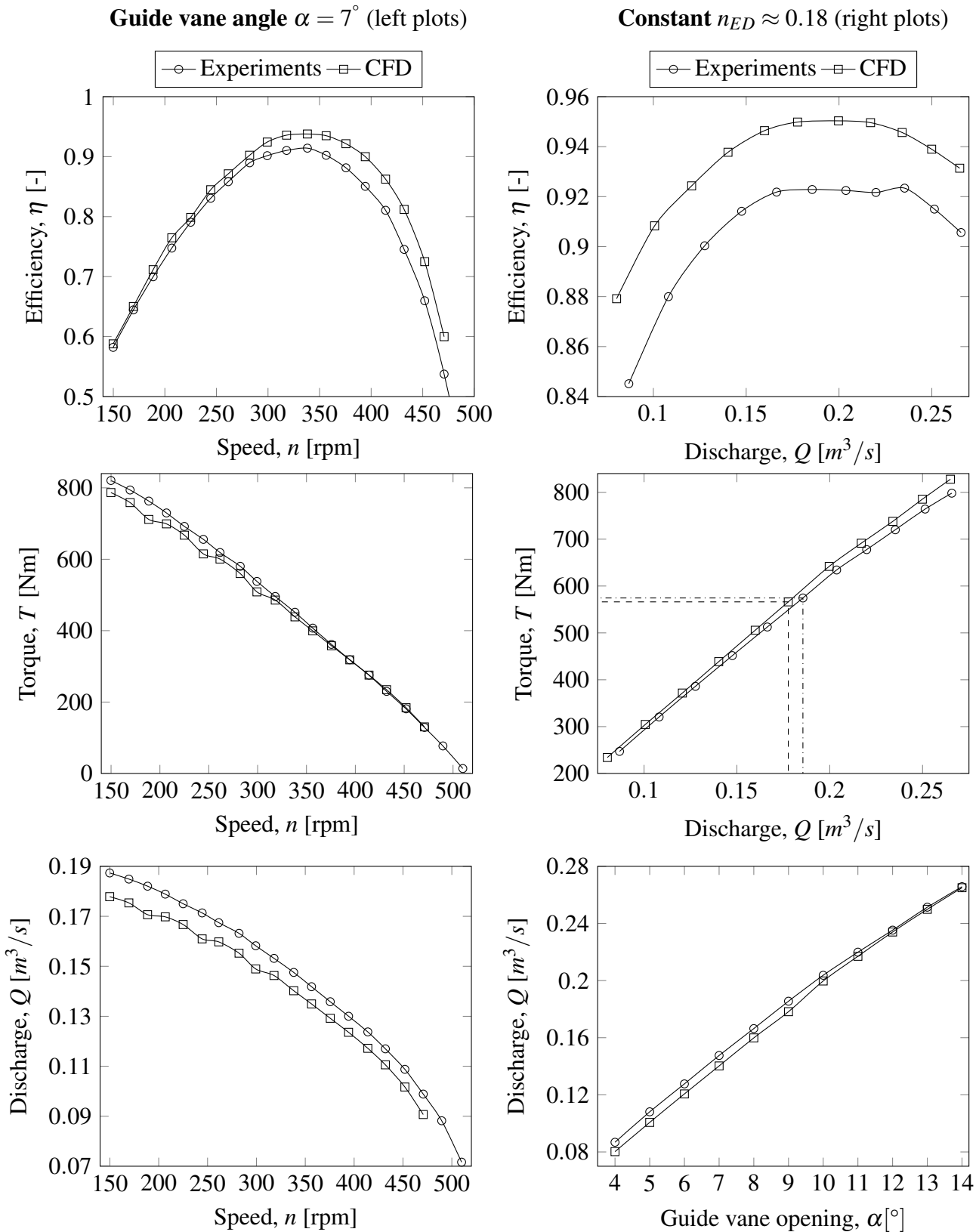


Figure 4.7: The three left plots show experimental and numerical CFD data for constant guide vane opening of $\alpha = 7^\circ$. The three right plots show experimental and numerical CFD data for constant $n_{ED} \approx 0.18$.

where P_m is the mechanical power transmitted through the coupling of the runner shaft and P_h is the hydraulic power exchanged with the water. This definition is similarly expressed in (16).

Another way of expressing the hydraulic efficiency is to analyze the power losses P_{loss} of each individual component over the power input P_{in} of the turbine. This way, the hydraulic efficiency would then be expressed as,

$$\eta = 1 - \frac{\sum P_{loss}}{P_{in}}. \quad (29)$$

Considering the waterway from the inlet of the spiral case to the outlet of the draft tube (see Fig. 2.4), these losses may be categorized into:

- $P_{Loss-SpiralCase}$: Power loss from wall friction and secondary flow losses in the spiral case including friction and incidence loss on stay vanes.
- $P_{Loss-GuideVaness}$: Power loss from guide vanes due to friction and incidence on the guide vane blades.
- $P_{Loss-Runner}$: Power loss from the runner, which can be divided into:
 - (a) $P_{Loss-Runner-Friction}$: Friction loss in the blade channel of the runner due to shear forces in the boundary layer.
 - (b) $P_{Loss-SwirlLoss}$: Loss in kinetic energy due to residual whirl being created at the outlet of the runner.
 - (c) $P_{Loss-IncidenceLoss}$: Loss caused by a difference between the direction of the fluid flow and the fixed blade angle at the inlet of the runner.
 - (d) $P_{Loss-Lekage}$: The leakage flow through the runner seals.
 - (e) $P_{Loss-DiskFriction}$: Friction loss losses of the outer surface of the runner not in contact with the main flow that is passing the runner blades [36].
- $P_{Loss-DraftTube}$: Due to skin friction, secondary flow in the elbow and decelerating flow in the draft tube.

Iliev et al. [78], outlined these different losses and applied simplified models to predict the general shape of the hill chart based on velocity triangles at the inlet and outlet of the shroud streamline. Considering $P_{Loss-IncidenceLoss}$, $P_{Loss-SwirlLoss}$, $P_{Loss-DraftTube}$, and $P_{Loss-Runner-Friction}$, theoretical equations were used to explain the different losses in the in the turbine, and their impact on the shape of the hill chart. Figure 4.8 (a) shows that $P_{Loss-IncidenceLoss}$ is most dependent on n_{ED} , and moving away from $n_{ED} = 0.18$, especially for higher values of n_{ED} , increases the incidence loss. In Fig. 4.8 (b); $P_{Loss-Runner-Friction}$ is also somewhat dependent on n_{ED} with higher gradient towards increasing n_{ED} , however the largest gradient in the Q_{ED} -direction. The draft tube loss and the swirl losses were most dependent on Q_{ED} (not seen in the figure).

Schiffer et al. [79], conducted a numerical study analyzing the different hydraulic losses and their impact on the hydraulic efficiency. The specific speed of the runner in [79] is almost two times the specific speed of the Francis-99 runner in this thesis. The comparison between the two runners should, therefore, be made carefully. Varying the flow rate, Schiffer [79] found that the losses due to spiral case were very small, i.e. max 0.8 percentage point of efficiency at a

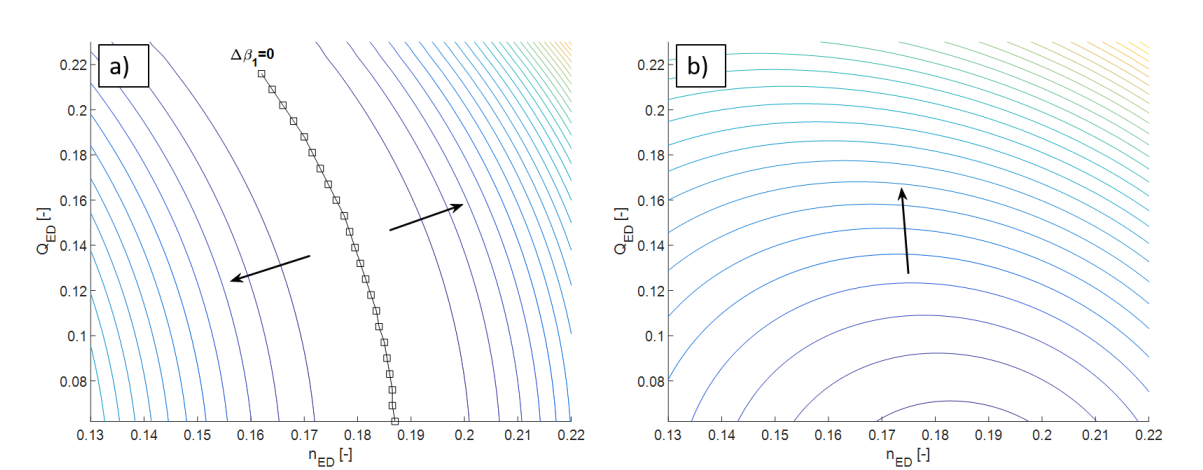


Figure 4.8: a) Hydraulic losses from incidence on the leading edge at the runner blade. b) Friction loss in runner. The figure is retrieved from [78, Fig. 3].

high flow rate. Leakage and disk friction loss were also relatively small compared to friction losses in guide vanes, runner, and draft tube.

The leakage flow is driven only by the pressure difference, which is almost the same since the head of the turbine is more or less the same in the experiments. On the Francis-99 runner; Celič et al. [59] studied the influence on hydraulic efficiency from labyrinth seal and disk friction losses using CFD. They found that the difference between the experimental and numerical efficiency lowers down from 7% to 2% at PL operation when accounting for these losses. The influence from leakage losses becomes more predominant for lower discharges as leakage flow becomes relatively higher compared to the flow through the runner, although the leakage flow stays the same. Reversely, the influence of labyrinth losses on the hydraulic efficiency decreased with the increase of the flow through the turbine. Disk friction losses are most dependent on runner speed, where increased speed increases the disk friction loss.

Having accurate numerical simulations with no spiral case might, by considering this research [79] and with the investigation outlined in Section 4.1; be justifiable. However, this deserves further scrutiny. Figure 4.9 brings together all the 2D plots from Appendix A.5 by calculating the difference in hydraulic efficiency ($\Delta\eta$) from (27). Increasing $\Delta\eta$ can be seen in Fig. 4.9 with increasing n_{ED} . Figure 4.10 confirms this, showing an increase in $\Delta\eta$ with increasing runner speed, n . A few negative values of $\Delta\eta$ can be observed in Fig. 4.10 for GV 4° and 5° , meaning underprediction of efficiency. Figure 4.10 collects all the information from Appendix A.6, showing $\Delta\eta$ for different guide vane angles. The rise in discrepancy for hydraulic efficiency is here related to a greater rotational speed of the runner. In regard to [78] and Fig. 4.8, one could argue that the simulations in this thesis underestimates the incidence loss from the runner blade leading edge and/or the runner friction loss. However, such conclusions, based on the evidence put forward in this thesis, should be drawn carefully. It is only meant as a possible explanation where further scrutiny is required. The last argument in this discussion is that higher values of $\Delta\eta$ are found at lower discharges, as is seen in Fig. 4.9. Considering [59], the reason for this might be the influence from the disk friction and labyrinth seal leakage loss, its effect on $\Delta\eta$ being higher at PL, i.e. low discharges. Again, one should be cautious in trusting such conclusions.

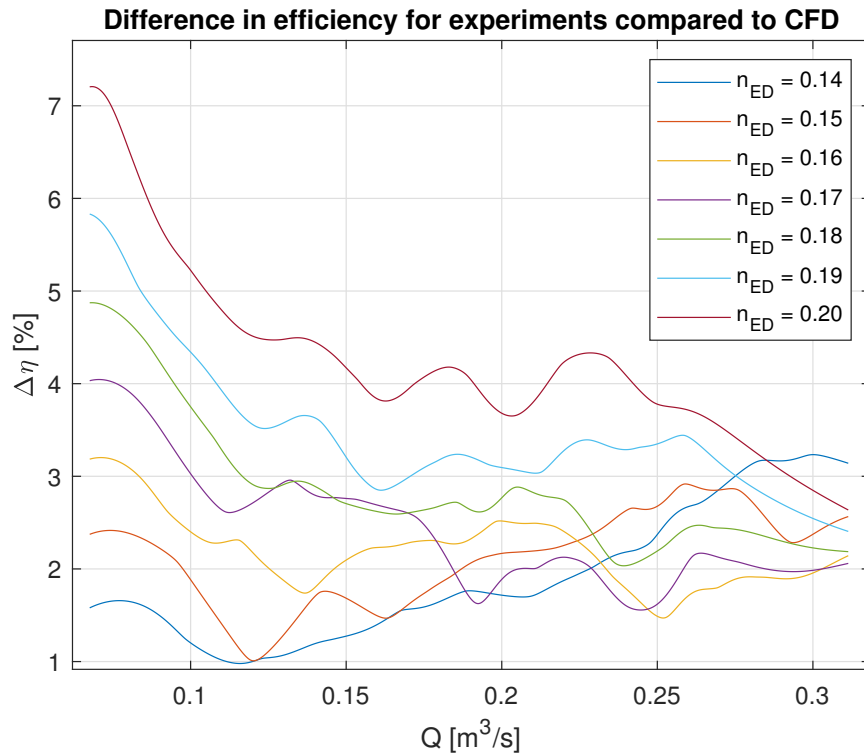


Figure 4.9: Difference in efficiency for experimental and numerical data for different constant n_{ED} lines.

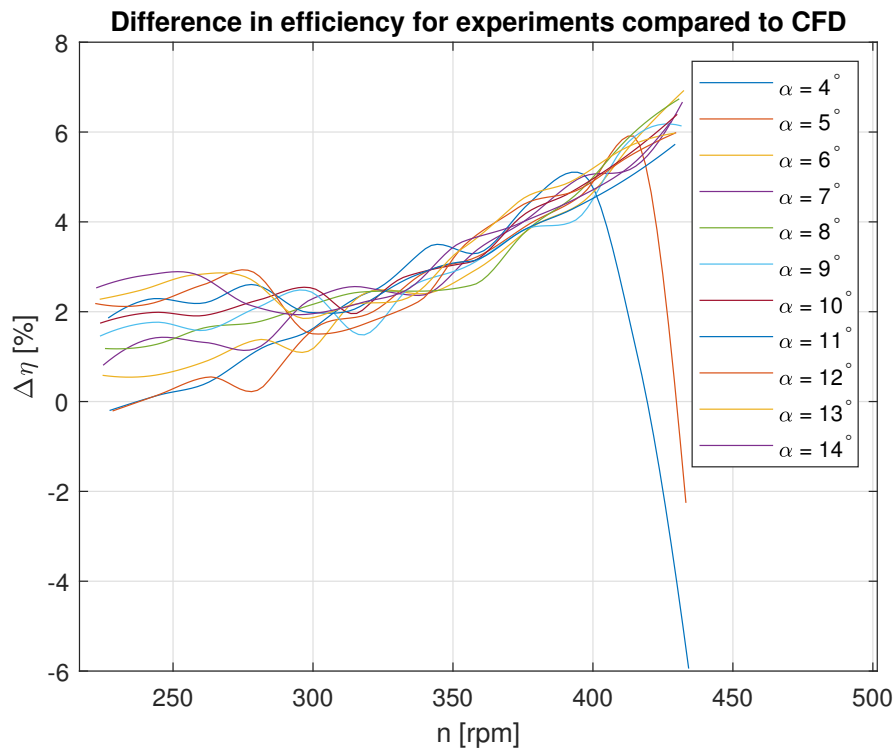


Figure 4.10: Difference in efficiency between experimental and numerical data for different guide vane openings (α).

Accurate prediction of the variable speed line is crucial when designing a Francis turbine meant for variable speed. Figure 4.5 showed how this line shifts from left for the experiment to the right for the numerical simulation. Having higher discrepancies efficiency ($\Delta\eta$) is discussed above. Figure 4.11 displays the 2D-graph of the variable-speed line. The numerical simulations over-predict the absolute value of this line. However, the general shape seems to be preserved well in Fig. 4.11.

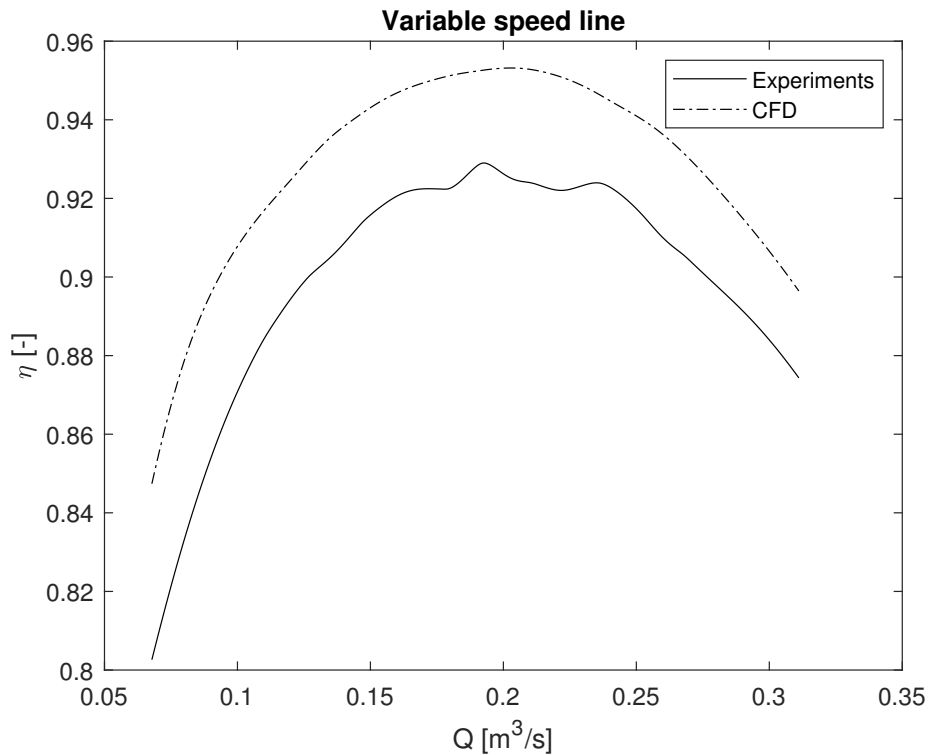


Figure 4.11: Variable speed line comparison between experiments and CFD.

4.6 Reducing simulation time

To reduce simulation time, the following methods have been discussed in this chapter:

- Reducing the geometry model, e.g. removing spiral case, simplifying GV geometry.
- Reducing mesh size.
- Optimizing parallel computing.
- Selection of turbulence model.

The last thing to address in this subject matter is; how many simulations do you need to solve?

To answer this question, it was attempted to reduce the number of operating points, i.e. simulations, in order to investigate this influence on the shape of the hill chart. The following six cases were considered:

- Case 1: Only even numbered guide vane angles were included. Resulted in 72 points.

- Case 2: Only odd numbered guide vane angles were included. Resulted in 60 points.
- Case 3: Only even numbered n_{ED} taken into account. Resulted in 66 points.
- Case 4: Combination of 1 and 3, i.e. even GV angles with 2^nd turbine speed. Resulted in 36 points.
- Case 5: Combination of 2 and 3, i.e. odd GV angles with 2^nd turbine speed. Resulted in 30 points.
- Case 6: Structurally removing every other point in n_{ED} - and Q_{ED} -direction. Resulted in 66 points.

All these cases, compared together with the full 132 point hill chart, is shown in Fig. 4.12. The complete hill chart, similar as in Fig. 4.6, is here shown in green. The red line shows the reduced hill chart for the different cases above. Red and green X is marked on each figure to show the location of BEP for the reduced and the full hill chart, respectively. The data points used to create the different cases is marked with blue squares, whereas the points left out is marked with small dots.

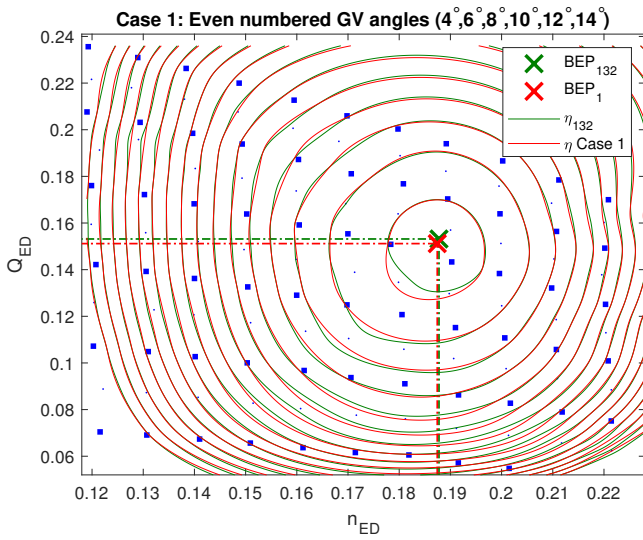
To quantify the different shape of the complete and reduced hill chart, the root-mean-square deviation was calculated by,

$$RMS = \sqrt{\frac{\sum_1^N (\eta_{132} - \eta_{reduced})^2}{N}} \times 100 \quad [\%], \quad (30)$$

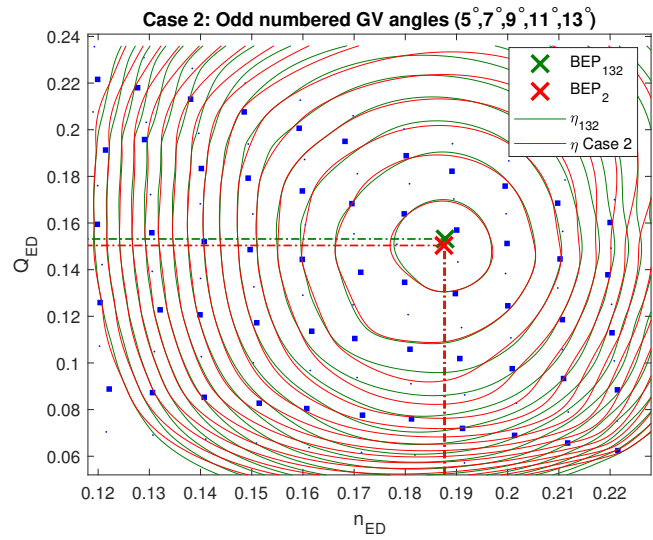
where η_{132} and $\eta_{reduced}$ is the hydraulic efficiency for the complete and the reduced hill chart, respectively. These values are from the interpolated points, where N is the number of points considered. In Table 4.10, (30) is calculated for 3.75×10^5 interpolation points as well as the deviation in percent. It turns out that all cases are very close to the complete hill chart, deviating $<0.2\%$ for every case. With only a deviation of $\approx 0.08\%$, the best method to reduce the number of operation points in the hill chart is Case 6. Reducing the number of simulation points would drastically reduce the computational cost of simulation of hill charts. This study shows that the number of operation points may be cut in half, and still produce accurately predicted hill chart.

Table 4.10: Evaluation of different methods for reducing interpolation points in hill chart.

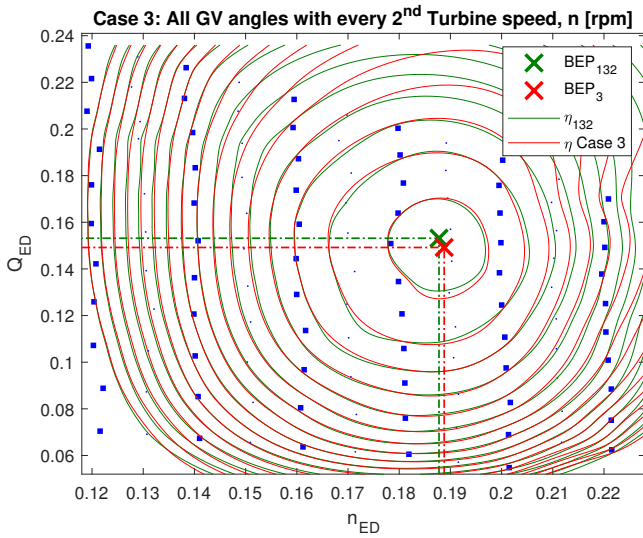
Case	1	2	3	4	5	6
RMS [%]	0.107	0.191	0.085	0.111	0.160	0.076
Normal Percent [%]	0.077	0.120	0.068	0.087	0.119	0.045



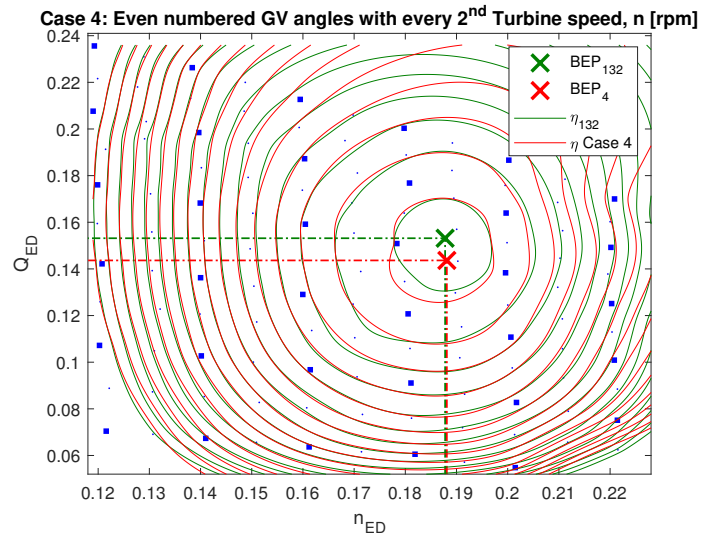
(a) Case 1: Even numbered guide vane angles.



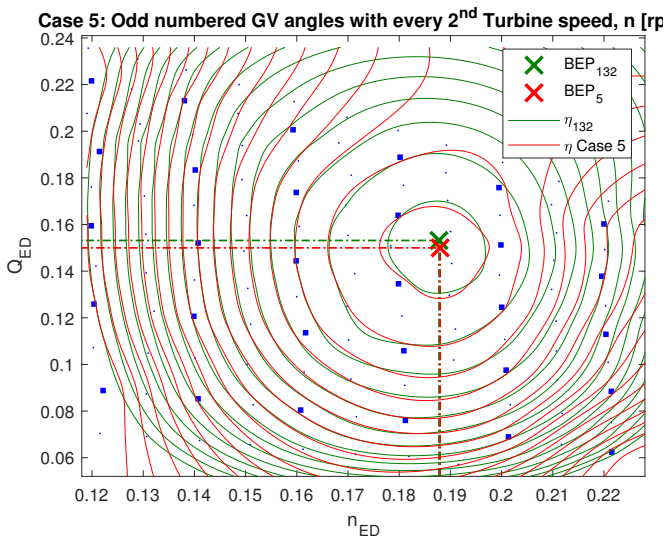
(b) Case 2: Odd numbered guide vane angles.



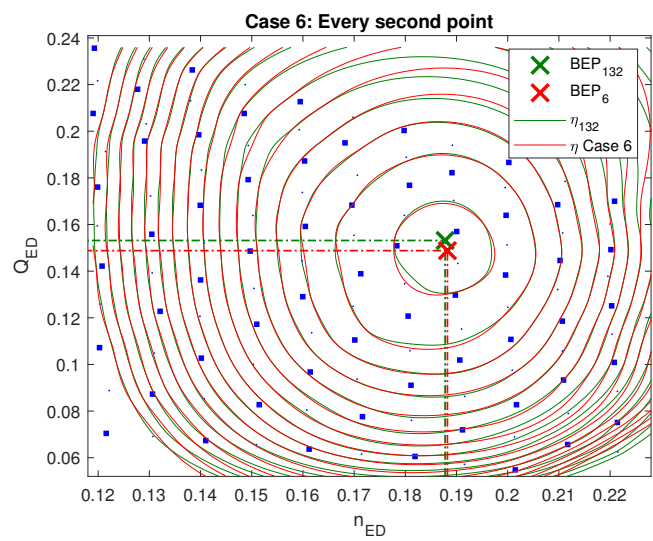
(c) Case 3: Every 2nd Turbine speed, n [rpm].



(d) Case 4: Even GV angles with 2nd Turbine speed.



(e) Case 5: Odd GV angles with 2nd Turbine speed.



(f) Case 6: Every second point.

Figure 4.12: Different methods for reducing interpolation points in hill chart.

5 Conclusion

Flow in a high head Francis turbine was analyzed using the standard $k - \varepsilon$ turbulence model. Numerical simulations were performed at 132 representative operating points and compared with available experimental data to verify its reliability. Simulations of different geometries were performed in order to reduce computational cost without sacrificing accuracy. A simplified geometry, without spiral case, were selected for the mesh independence study. Mesh independence study was carried out at part load, with guide vane opening of 7° for three different runner speeds. Mesh independence was also studied at BEP. This test showed grid discretization uncertainties up to 5.34% in discharge, Q . For the most part, uncertainties were low for efficiency. Medium mesh size was selected for further use due to computational cost. More precise prediction could be achieved, taking the labyrinth seals and disk friction loss into account.

Using three different turbulence models; $k - \varepsilon$, SST, and RNG- $k - \varepsilon$, investigation was done in order to address find the speed and accuracy of the models. The standard $k - \varepsilon$ were faster and more accurate and were selected for further use. A benchmark study was carried out to find the optimal number of computational cores to use, and were found to be 8 nodes. A hill chart over a wide range of $n_{ED}-Q_{ED}$ was produced and compared with experimental data. The difference between the experimental and numerical results was on average 2.87% overprediction, with the maximum difference (6.93%) being observed at $n = 432.5$ [rpm] and GV opening 6° . The BEP for the numerical results was higher and shifted to the right, compared to experiments. Torque was well predicted for most operating points. Omitting the simulation of labyrinth seals is believed that this is the main contributor to the discrepancies in efficiency in this thesis. However, the discrepancies could also come from disregarding losses in the spiral case and stay vanes. In general, efficiency is overestimated. Otherwise, the shape of the efficiency curve is fairly well captured. Reduction in the number of simulated operating points will reduce the computational cost a lot. Findings from this work shows that the number of points can be cut in half, compared to the original 132-point hill chart, without losing accuracy. That is if the reduction is made in a structural way, i.e. Case 6.

The calibration of a numerical method for efficiency calculations of Francis turbines is completed. This method proved itself effective for prediction of hill charts. However, it remains to see if this holds true for different turbine designs.

6 Further work

The different turbulence models are sensitive to different mesh with different Y^+ -values and element quality. Although the quality of the mesh has been checked (and were good) before a simulation, a systematic procedure to inspect the sensitivity of mesh quality on different turbulence models may be considered for further work. This also includes the study of the Y^+ -values.

When the mesh is satisfactory, the next step would be to perform simulations to investigate the influence of different losses, and to categorize them into parts to address their influence in hydraulic efficiency. This would create a deeper understanding of the physical features of the turbine as well as revealing the limitation of CFD-simulations.

Simulations at deep part load guide vane openings, $\alpha < 4$, and with high/low rotational speeds, can be considered for further work. This would include simulation on the runaway line where the flow is transient and highly unstable. A complete hill chart could then be created entirely from numerical simulations.

Several measures can be done to increase the simulation, speed such as; having a looser convergence criterion, fewer iterations, lower ordered advection scheme, and initializing simulations from previous ones.

The last, perhaps, most important step for further work is to apply this calibrated method on a different runner, where experimental data are available. The true accuracy of this simulation method would then be revealed and only then could say if the method applies to other turbines.

References

- [1] “BP Statistical review of world energy june 2018.” URL: <https://www.bp.com/content/dam/bp/en/corporate/pdf/energy-economics/statistical-review/bp-stats-review-2018-full-report.pdf>. Accessed: 2018-12-05.
- [2] T. Koetsier and M. Ceccarelli, “Explorations in the History of Machines and Mechanisms: Proceedings of HMM2012,” in *Explorations in the History of Machines and Mechanisms*, vol. 15 of *History of Mechanism and Machine Science*, (Dordrecht), pp. 397 – 404, Springer Netherlands, 2012.
- [3] The Norwegian Water Resources and Energy Directorate, “Norway and the european power market.” URL: <https://www.nve.no/energy-market-and-regulation/wholesale-market/norway-and-the-european-power-market/>, 28.01.2016. Accessed: 2018-12-04.
- [4] Politico, “Oil-rich norway could become europes green battery.” URL: <https://www.politico.eu/article/norways-glaciers-could-fill-europes-energy-gap-green-battery-renewables/>, 2016. Accessed: 2018-12-04.
- [5] M. Sprenger, “Debatable whether norway will become europe’s green battery.” URL: sintef.com/latestnews/debatablewhethernorwaywillbecomeeurope\T1\textquoterightsgreenbattery, 2018. Accessed: 2018-12-04.
- [6] S. Sawyer, “Global wind energy outlook 2016 (webinar presentation).” URL: <https://cleanenergysolutions.org/sites/default/files/documents/panelist-slides-gweo-2016-dec-15-2016.pdf>. Accessed: 2018-12-04.
- [7] IEA wind, “Wind energy in norway.” URL: <https://community.ieawind.org/about/member-activities/norway>. Accessed: 2018-12-05.
- [8] H. Holttinen, “Hourly wind power variations in the nordic countries,” *Wind Energy*, vol. 8, no. 2, pp. 173–195, 2005.
- [9] A. Deepak, C. Roger, and J. Gerald, “The impact of hydroelectric power and other forms of generation on grid frequency stability for the wecc region,” *HydroVision International, Sacramento, CA, July*, pp. 19–22, 2011.
- [10] E. Øgaard, “Francis-turbin.” URL: <http://www.vasskrafta.no/turbinar/francis-turbin-article214-479.html>, Dec. 2018. Accessed: 2018-12-04.
- [11] H. Brekke, *HYDRAULIC TURBINES Design, Erection and Operation*. NTNU, June 2001.
- [12] M. V. Magnoli and M. Maiwald, “Influence of hydraulic design on stability and on pressure pulsations in francis turbines at overload, part load and deep part load based on numerical simulations and experimental model test results,” *IOP Conference Series: Earth and Environmental Science*, vol. 22, p. 032013, Mar 2014.
- [13] U. Seidel, C. Mende, B. Hübner, W. Weber, and A. Otto, “Dynamic loads in Francis runners and their impact on fatigue life,” *IOP Conference Series: Earth and Environmental Science*, vol. 22, no. 3, p. 032054, 2014.

- [14] D. Schafer and J.-J. Simond, “Adjustable speed asynchronous machine in hydro power plants and its advantages for the electric grid stability..” URL: <http://infoscience.epfl.ch/record/134078>, 1998. Accessed: 2019-06-05.
- [15] T. Hildinger and L. Kodding, “Modern design for variable speed motor-generators-asynchronous (DFIM) and synchronous (SMFI) electric machinery options for pumped storage powerplants,” *Innsbruck, Hydro*, 2013.
- [16] C. Farell and J. Gulliver, “Hydromechanics of variable speed turbines,” *Journal of Energy Engineering*, vol. 113, no. 1, pp. 1–13, 1987.
- [17] M. Valavi and A. Nysveen, “Variable-speed operation of hydropower plants: A look at the past, present, and future,” *IEEE Industry Applications Magazine*, vol. 24, no. 5, pp. 18–27, 2018.
- [18] T. Kuwabara, A. Shibuya, and H. Furuta, “Design and dynamic response characteristics of 400 MW adjustable speed pumped storage unit for ohkawachi power station,” *IEEE Transactions on Energy Conversion*, vol. 11, no. 2, pp. 376–384, 1996.
- [19] G. Heckelsmueller, “Application of variable speed operation on Francis turbines,” *Ingenieria e Investigacion*, vol. 35, no. 1, pp. 12–16, 2015.
- [20] T. Vu and W. Shyy, “Performance prediction by viscous flow analysis for Francis turbine runner,” *Journal of fluids engineering*, vol. 116, no. 1, pp. 116–120, 1994.
- [21] M. Sabourin, Y. Labrecque, and V. De Henau, “From components to complete turbine numerical simulation,” in *Hydraulic Machinery and Cavitation*, pp. 248–256, Springer, 1996.
- [22] K. Anup, B. Thapa, and Y.-H. Lee, “Transient numerical analysis of rotor–stator interaction in a Francis turbine,” *Renewable Energy*, vol. 65, pp. 227 – 235, 2014. SI:AFORE 2012.
- [23] H. Akin, Z. Aytac, F. Ayancik, E. Ozkaya, E. Arioz, K. Celebioglu, and S. Aradag, “A CFD aided hydraulic turbine design methodology applied to Francis turbines,” in *Power Engineering, Energy and Electrical Drives (POWERENG), 2013 Fourth International Conference on*, pp. 694–699, IEEE, 2013.
- [24] J. Wu, K. Shimmei, K. Tani, K. Niikura, and J. Sato, “CFD-based design optimization for hydro turbines.(computational fluid dynamics)(author abstract)(report),” *Journal of Fluids Engineering*, vol. 129, no. 2, 2007.
- [25] S. Aradag, H. Akin, and K. Celebioglu, “CFD based design of a 4.3MW francis turbine for improved performance at design and off-design conditions,” *Journal of Mechanical Science and Technology*, vol. 31, pp. 5041–5049, Oct 2017.
- [26] H. Keck, P. Drtina, and M. Sick, “Numerical hill chart prediction by means of CFD stage simulation for a complete francis turbine,” in *Hydraulic Machinery and Cavitation*, pp. 170–179, Springer, 1996.
- [27] E. Tengs, P.-T. Storli, and M. A. Holst, “Numerical generation of hill-diagrams; validation on the francis99 model turbine,” *International Journal of Fluid Machinery and Systems*, vol. 11, no. 3, pp. 294–303, 2018.

- [28] T. C. Vu and S. Retieb, “Accuracy assessment of current cfd tools to predict hydraulic turbine efficiency hill chart,” in *Proceedings of the 21st IAHR Symposium on Hydraulic Machinery and Systems, Lausanne, Switzerland*, vol. 1, pp. 193–198, 2002.
- [29] “Norwegian hydropower centre, *Francis 99*.” URL: <https://www.ntnu.edu/nvks/francis-99>. Accessed: 2018-12-05.
- [30] I. Iliev, C. Trivedi, E. Agnalt, and O. G. Dahlhaug, “Experimental study of the pressure pulsations in variable-speed francis and pump turbines,” *International Association for Hydro-Environment Engineering and Research, IAHR2018 Kyoto, Japan*, Soon available online, 2018.
- [31] C. Trivedi, M. Cervantes, B. K. Gandhi, and O. G. Dahlhaug, “Experimental and numerical studies for a high head Francis turbine at several operating points,” *Journal Of Fluids Engineering - Transactions Of The Asme*, vol. 135, no. 11, 2013.
- [32] A. Nordvik, “Variable speed operations of Francis turbines,” Project Thesis, NTNU, Produktutvikling og produksjon, Energi-, prosess- og strømningssteknikk, 2018.
- [33] H. Brekke, *Pumper & Turbiner*. NTNU, March 2003.
- [34] E. Tengs, P.-T. Storli, and M. Holst, “Optimization procedure for variable speed turbine design,” *Engineering Applications of Computational Fluid Mechanics*, vol. 12, no. 1, pp. 652–661, 2018.
- [35] H. Brekke, *Introduction To Hydraulic Machinery*. NTNU, March 2000.
- [36] International Electrotechnical Commission, “Hydraulic turbines, storage pumps and pump-turbines - Model acceptance tests,” Nov. 1999.
- [37] J. Fraile-Ardanuy, J. R. Wilhelmi, J. J. Fraile-Mora, and J. I. Perez, “Variable-speed hydro generation: operational aspects and control,” *IEEE Transactions on Energy Conversion*, vol. 21, pp. 569–574, June 2006.
- [38] E. H. Sundfør, “Design and operation of a Francis turbine with variable speed capabilities,” Master’s thesis, NTNU, 2017.
- [39] A. Borghetti, M. Di Silvestro, G. Naldi, M. Paolone, and M. Alberti, “Maximum efficiency point tracking for adjustable-speed small hydro power plant,” *16th PSCC, Glasgow, Scotland*, 2008.
- [40] C. Bergan, R. Goyal, M. J. Cervantes, and O. G. Dahlhaug, “Experimental investigation of a high head model Francis turbine during steady-state operation at off-design conditions,” *IOP Conference Series: Earth and Environmental Science*, vol. 49, no. 6, 2016.
- [41] C. Trivedi, M. Cervantes, and O. G. Dahlhaug, “Experimental and numerical studies of a high-head francis turbine: A review of the Francis-99 Test Case,” *Energies*, 2016.
- [42] D. C. Wilcox, *Turbulence modeling for CFD*. La C nada, Calif: DCW Industries, 2nd ed. ed., 1998.
- [43] W. Jones and B. Launder, “The prediction of laminarization with a two-equation model of turbulence,” *International Journal of Heat and Mass Transfer*, vol. 15, no. 2, pp. 301 – 314, 1972.

- [44] H. Versteeg, *An introduction to computational fluid dynamics : the finite volume method*. Harlow: Pearson/Prentice Hall, 2nd ed. ed., 2007.
- [45] X.-D. Yang, H.-Y. Ma, and Y.-N. Huang, “Prediction of homogeneous shear flow and a backward-facing step flow with some linear and non-linear k- ϵ turbulence models,” *Communications in Nonlinear Science and Numerical Simulation*, vol. 10, no. 3, pp. 315 – 328, 2005.
- [46] F. R. Menter, M. Kuntz, and R. Langtry, “Ten years of industrial experience with the SST turbulence model,” *Turbulence, heat and mass transfer*, vol. 4, no. 1, pp. 625–632, 2003.
- [47] A. N. Kolmogorov, “Equations of turbulent motion in an incompressible fluid,” in *Dokl. Akad. Nauk SSSR*, vol. 30, pp. 299–303, 1941.
- [48] F. R. Menter, “Two-equation eddy-viscosity turbulence models for engineering applications,” *AIAA journal*, vol. 32, no. 8, pp. 1598–1605, 1994.
- [49] “SST k-omega model.” URL: https://cfd-online.com/Wiki/SST_k-omega_model. Accessed: 2018-12-11.
- [50] S. A. Orszag, “Analytical theories of turbulence,” *Journal of Fluid Mechanics*, vol. 41, no. 2, pp. 363–386, 1970.
- [51] G. N. Coleman and R. D. Sandberg, “A primer on direct numerical simulation of turbulence-methods, procedures and guidelines,” *Technical Report AFM-09/01a*, 2010.
- [52] W. E. Nagel, D. B. Kröner, and M. M. Resch, eds., *High performance computing in science and engineering '10 : transactions of the High Performance Computing Center, Stuttgart (HLRS) 2010*. Berlin ;: Springer-Verlag, 2010.
- [53] J. H. Ferziger and M. Peric, *Computational methods for fluid dynamics*. Springer Science & Business Media, 2012.
- [54] W. L. Oberkampf, M. Sindir, and A. T. Conlisk, “Guide for the verification and validation of computational fluid dynamics simulations,” *American Institute of Aeronautics and Astronautics, Reston, VA*, 1998.
- [55] NASA, “*Uncertainty and Error in CFD Simulations*.” URL: <https://www.grc.nasa.gov/WWW/wind/valid/tutorial/errors.html>. Accessed: 2019-06-10.
- [56] U. B. Mehta, “Guide to credible computer simulations of fluid flows,” *Journal of Propulsion and Power*, vol. 12, no. 5, pp. 940–948, 1996.
- [57] Sharcnet, “*11.1.1. Discretization of the Governing Equations*.” URL: https://www.sharcnet.ca/Software/Ansys/16.2.3/en-us/help/cfx_thry/i1311648.html. Accessed: 2019-06-10.
- [58] Sharcnet, “*14.2. Special Partitioner, Solver and Interpolator Executables*.” URL: https://www.sharcnet.ca/Software/Ansys/16.2.3/en-us/help/cfx_solvr/i1305559.html#i1305580. Accessed: 2019-06-10.
- [59] D. Čelič and H. Ondráčka, “The influence of disc friction losses and labyrinth losses on efficiency of high head Francis turbine,” *Journal of Physics: Conference Series*, vol. 579, no. 1, p. 012007, 2015.

- [60] K.-R. G. Jakobsen, E. Tengs, and M. A. Holst, “Reducing computational effort of high head Francis turbines,” *IAHR2018, Kyoto, Japan*, 2018.
- [61] M. J. Selvig Hallén, “Simulation of Rotor-Stator Interactions (RSI’s) in a High Head Francis Turbine,” Master’s thesis, NTNU, Produktutvikling og produksjon, Energi-, prosess- og strømningssteknikk, 2018.
- [62] Z. Yaping, L. Weili, R. Hui, and L. Xingqi, “Performance study for Francis-99 by using different turbulence models,” *Journal of Physics: Conference Series*, vol. 579, no. 1, p. 012012, 2015.
- [63] Sharcnet, “2.3.2. Recommended Configurations of Boundary Conditions.” URL: https://www.sharcnet.ca/Software/Ansys/16.2.3/en-us/help/cfx_mod/i1300679.html. Accessed: 2018-12-16.
- [64] D. Jošt, A. Škerlavaj, M. Morgut, P. Mežnar, and E. Nobile, “Numerical simulation of flow in a high head Francis turbine with prediction of efficiency, rotor stator interaction and vortex structures in the draft tube,” *Journal of Physics: Conference Series*, vol. 579, no. 1, p. 012006, 2015.
- [65] Sharcnet, “2.2.2. Two Equation Turbulence Models.” URL: https://www.sharcnet.ca/Software/Ansys/16.2.3/en-us/help/cfx_thry/i1302321.html#i1302327. Accessed: 2018-12-11.
- [66] H. NTNU, “Idun cluster info.” URL: <https://www.hpc.ntnu.no/display/hpc/Idun+Cluster>. Accessed: 2019-05-24.
- [67] H. NTNU, “Vilje info.” URL: <https://www.hpc.ntnu.no/display/hpc/Vilje>. Accessed: 2019-05-24.
- [68] M. Lenarcic, M. Eichhorn, S. J. Schoder, and C. Bauer, “Numerical investigation of a high head francis turbine under steady operating conditions using foam-extend,” *Journal of Physics: Conference Series*, vol. 579, p. 012008, Jan 2015.
- [69] J. D. Buron, S. Houde, R. Lestriez, and C. Deschênes, “Application of the non-linear harmonic method to study the rotor-stator interaction in francis-99 test case,” *Journal of Physics: Conference Series*, vol. 579, p. 012013, Jan 2015.
- [70] I. Celik, U. Ghia, P. Roache, C. Freitas, H. Coleman, and P. Raad, “Procedure for estimation and reporting of uncertainty due to discretization in CFD applications,” *Journal of Fluids Engineering (Transactions of the ASME)*, vol. 130, no. 7, pp. 078001 (4)–078001 (4), 2008.
- [71] Sharcnet, “Chapter 14: CFX Expression Language (CEL).” URL: https://www.sharcnet.ca/Software/Ansys/16.2.3/en-us/help/cfx_ref/i1304009.html. Accessed: 2018-12-17.
- [72] A. B. Bondi, “Characteristics of scalability and their impact on performance,” in *Proceedings of the 2Nd International Workshop on Software and Performance, WOSP '00*, (New York, NY, USA), pp. 195–203, ACM, 2000.
- [73] G. M. Amdahl, “Validity of the single processor approach to achieving large scale computing capabilities, reprinted from the afips conference proceedings, vol. 30 (atlantic city,

- n.j., apr. 18–20), afips press, reston, va., 1967, pp. 483–485, when dr. amdahl was at international business machines corporation, sunnyvale, california,” *IEEE Solid-State Circuits Society Newsletter*, vol. 12, pp. 19–20, Summer 2007.
- [74] J. F. Gülich, *Numerical Flow Calculations*, pp. 499–574. Berlin, Heidelberg: Springer Berlin Heidelberg, 2014.
- [75] F.-S. Lien and M. Leschziner, “Assessment of turbulence-transport models including non-linear rng eddy-viscosity formulation and second-moment closure for flow over a backward-facing step,” *Computers & Fluids*, vol. 23, no. 8, pp. 983–1004, 1994.
- [76] C. Trivedi, M. J. Cervantes, and B. K. Gandhi, “Investigation of a high head francis turbine at runaway operating conditions,” *Energies*, vol. 9, no. 3, 2016.
- [77] K.-R. G. Jakobsen and M. A. Holst, “Cfd simulations of transient load change on a high head francis turbine,” in *Journal of Physics: Conference Series*, vol. 782, p. 012002, IOP Publishing, 2017.
- [78] I. Iliev, C. Trivedi, and O. Dahlhaug, “Simplified hydrodynamic analysis on the general shape of the hill charts of francis turbines using shroud-streamline modeling,” *Journal of Physics: Conference Series*, vol. 1042, no. 1, 2018.
- [79] J. Schiffer, H. Benigni, and H. Jaberg, “Analysis of the leakage behavior of francis turbines and its impact on the hydraulic efficiency—a validation of an analytical model based on computational fluid dynamics results,” *Journal of Fluids Engineering*, vol. 139, no. 2, p. 021106, 2017.
- [80] J. Boussinesq, “Essa sur latheries des eaux courantes. memoires presentes par divers savants a l’academic des sciences de l’institut national de france,” *Tome XXIII*, no. 1, 1877.

A Appendix

A.1 Paper for CRHT-IX'19

The following paper was written in association with CRHT-IX'19 symposium in Kathmandu, Nepal.

Numerical prediction of hill charts of Francis turbines

Andreas Nordvik, Igor Iliev, Chirag Trivedi, and Ole Gunnar Dahlhaug

Department of Energy and Process Engineering, Norwegian University of Science and Technology, Trondheim, Norway

E-mail: andnordv@stud.ntnu.no

April 2019

Abstract. This present work compares numerically predicted hill chart to experimental measurements of a Francis turbine. The main objective is to create a model for recreating hill charts using computational fluid dynamics (CFD). Accurate prediction of hill charts are useful in the design stage of production and may result in a more efficient runner. The primary focus is the prediction of efficiency and investigation of possible simplifications without loss in accuracy. By using steady-state simulations, preliminary tests were made on four different meshes, and two different turbulence models, namely the standard $k - \varepsilon$ model and the shear stress transport model. Simplifications of geometry have been tested to investigate if the simulation time can be reduced without sacrificing accuracy. Numerical simulations of 132 operating points were carried out. The efficiency was predicted with the maximal difference from measured values of 6.93%.

1. Introduction

With the rapid development of computer technology, computational fluid dynamics (CFD) has emerged as a powerful tool to directly simulate internal turbulent flow in individual or multiple components of a turbomachine [1, 2]. Turbines are tailor-made to specific conditions at a specific site, and small improvements in the geometry can have a large positive effect on operation [3]. A CFD aided design methodology applied to hydraulic turbines is, therefore, a desirable approach for increasing efficiency [4]. This has also been studied in [5, 6]. The efficiency diagram, also called hill chart, provides useful information about a turbine. The first numerically predicted hill chart using CFD was published in 1996 [7]. Accurate prediction of hill charts are useful in the design stage of production and can be used in an optimization procedure which may result in a more efficient runner [8]. The main objective of this work is to create a model for recreating hill charts using CFD.

This paper seeks to investigate the efficiency of high head Francis turbines utilizing the Francis-99 turbine at NTNU as validation for the study. By means of CFD simulations, construction of 132 operating points in the hill chart are predicted. The simulations are then compared with experimental results for validation. Trivedi et al. [9] carried out experimental

and numerical studies for a high head Francis turbine at several operating points, namely best efficiency point, high load (HL), and two different operating points at part load (PL). The simulations took 90 days to complete on a cluster of central processing units (CPU), and the results showed good agreement with experiments for efficiency. The difference between the experimental and numerical results increased on moving away from the best efficiency point, with the maximum difference ($\sim 11\%$) being observed at part load. Due to discrepancies in efficiency being large together with the aforementioned transient phenomenons, it was decided to mesh independence study on part load with guide vane (GV) opening of 70%, as well as for BEP (GV opening being 100%). Steady-state simulations for 11 different guide vane openings were carried out from PL (GV opening 40%) to HL (GV opening 140%).

2. Theory

2.1. The Hill-diagram

The hydraulic efficiency in a hydro turbine is calculated as the power output divided by the available water power:

$$\eta = \frac{\omega T}{\rho g Q H} \quad [-] \quad (1)$$

where T is the torque on the runner's hub, shroud, and blades, ω is the angular velocity of the turbine runner, ρ is the fluid density, g is the gravitational acceleration and Q is the discharge (volumetric flow rate) through the turbine.

The net head in equation (1) is, according to the guidelines set in IEC 60193 [10], defined as

$$H = \frac{\Delta P}{\rho g} + \frac{v_1^2 - v_2^2}{2g} + (z_1 - z_2) \quad [m] \quad (2)$$

, where v_1 and v_2 are the velocities at the inlet and outlet respectively. The last term describes the difference in elevation from inlet to outlet. The value of the pressure (ΔP) is acquired by the differential pressure, as shown in figure 1.

The Hill-diagram provides us with useful information about a turbine. The efficiency diagram is also called the characteristic diagram. It shows the turbines characteristics, or how it performs, under different operating conditions [11]. Hill-diagrams are created with dimensionless parameters so it is applicable for all turbines that are equally shaped geometrically. We can then compare with other rotating machinery, models and prototypes [11]. According to IEC 60193, to construct the Hill-diagram, the dimensionless volume flow Q_{ED} is plotted against the dimensionless rotational speed n_{ED} [10]. These parameters are given as,

$$Q_{ED} = \frac{Q}{D_2^2 \sqrt{gH}} \quad [-] \quad (3)$$

$$n_{ED} = \frac{n D_2}{\sqrt{gH}} \quad [-] \quad (4)$$

, where D_2 is the outlet diameter in meter and n is the rotational speed in rpm.

To create the Hill-diagram, one has to measure the flow, head, and torque. The guide vane opening has to be kept constant while the rotational speed is varied. This procedure is then repeated for several different guide vane openings, and by (3) and (4) one can plot the points along constant guide vane lines.

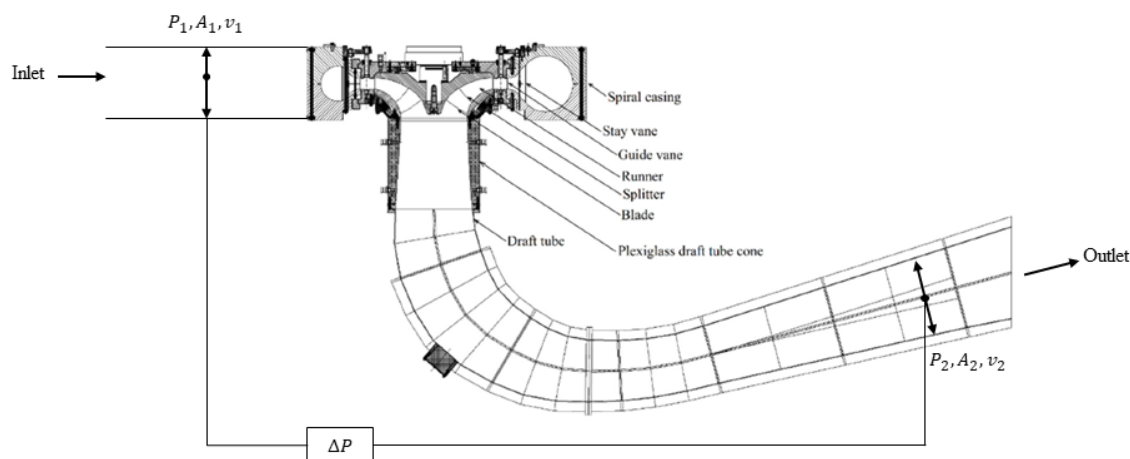


Figure 1. Two-dimensional view of the investigated model Francis turbine, retrieved from [12] and edited. $\Delta P = P_1 - P_2$ and A denotes the area.

2.2. The Francis-99 test case

The test case for this study is a model turbine at the Waterpower Laboratory at NTNU. It is a Francis type 1:5.1 scaled model of a prototype in a Norwegian power plant called Tokke [13]. It includes a spiral casing, a distributor with 14 stay vanes integrated into the spiral casing and 28 guide vanes. The runner has 15 blades with an additional 15 splitter blades, for a total of 30 runner blades. The draft tube is an elbow-type. A 2D section of the model is illustrated in figure 1. The test rig is a hydraulic system capable of generating $\approx 14\text{m}$ head for open loop, and $\approx 100\text{m}$ head for closed loop [12]. The experimental data used for validation of the CFD method in this paper is taken from [14]. However, the placement of BEP in figure 3 does not come from this study but have been tested more extensively in other measurement performed in the lab in accordance with IEC 60193 [10].

3. Numerical model

3.1. Computational domain

A complete simulation of the turbine with spiral casing, distributor, runner and draft tube including the labyrinth seal and disk friction losses is necessary for a realistic simulation of the flow in Francis turbines [15]. However, the increasing complexity and size of the

geometry will make a necessity for more cells in the computational mesh in order to get a good resolution of the flow in the simulation. This is computationally demanding and will result in longer simulation time. A full simulation with all details is therefore not feasible. The spiral case and draft tube are large and thereby requires a lot of cells. To reduce the computational cost, preliminary tests were conducted and are divided into three different cases; Case 1: Full model, Case 2: No spiral case and Case 3: Short draft tube and no spiral case. These tests showed that the relative speedup between Case 2 and Case 1 was about 1,8. Which means that reducing the geometry by excluding the spiral case was almost twice as fast to simulate as well as preserving the accuracy of the simulation. Case 3 showed an unstable behavior and did not converge. It was then decided to proceed with Case 2. The computational domain of Case 2 including boundary conditions is shown in figure 2.

3.2. Mesh

The meshes for the draft tube, runner and the guide vanes were made separately for different studies connected to Francis-99. The mesh for the draft tube was made with the ANSYS CAD module ICEM CFD. Similar meshes from previous studies had been tested for convergence [9]. However, a new mesh independence study was conducted in order to ensure mesh independence with the changes that were made.

Because simulations were going to be executed for several different guide vane openings it was necessary to create several meshes for each change in the guide vane angle. TurboGrid was used to rotate the geometry and create the mesh. The mesh was then checked for element quality and then exported for further use in CFX.

3.3. Turbulence models

Preliminary tests were conducted on two different turbulence models, the Shear Stress Transport model (SST) and $k - \epsilon$ -model. For the same turbine, the model turbine installed at the Waterpower Laboratory at NTNU, C. Trivedi et al. [9] conducted a numerical study where they used the same two turbulence models, namely SST and $k - \epsilon$. They found that $k - \epsilon$ was better at estimating the hydraulic efficiency with about $\sim 1\%$. Another study on the same turbine, the Francis-99, from Z. Yaping et al. [16] compared the standard $k - \epsilon$ turbulence model to the SST model with different outlet boundary conditions. They found that the differences between the experimental and numerical efficiency, head and torque simulated by standard $k - \epsilon$ turbulence model are smaller than that simulated by the SST turbulence model. Hence, the $k - \epsilon$ model could better predict steady-state efficiency. Again, on the same turbine, D. Jošt et al. [17] carried out a numerical study where they used SST, standard $k - \epsilon$ and zonal large-eddy-simulation (ZLES) with different inlet conditions and solvers in order to estimate the efficiency at three operating points. They found that the efficiency, calculated with CFX, yielded good agreement with the use of $k - \epsilon$ model, however, this was only so because both head and torque were wrong with about the same.

The selection of turbulence models for this paper was made from the basis of these studies. Since it is the same turbine in all three studies, it is easy to compare with the results of this article.

3.4. Simulation setup

The preliminary tests were performed on a local computer with steady-state analysis type and at runner speed equal $n_{ED} \approx 0.18$, and guide vane opening of 40%. The convergence criteria for all the simulations was set to $RMS \leq 10^{-5}$. Simulations were set to run for 1000 iterations even if the convergence criteria for rms of pressure, mass-momentum, and turbulent parameters were met.

The computational resources to perform simulations were used under the No-tur/Norstore project: Numerical investigations of a Francis turbine (project number NN9504K), using a super-computer at NTNU . No change in any parameter of interest was seen after 3500 iterations when conducting mesh independence study (set to 5000 iterations). This was done to ensure convergence for the mesh independence study. All the solution parameters used for performing the numerical simulations are shown in table 1.

Table 1. System setup for all simulations.

Parameter	Description
Analysis type	Steady state
Interfaces	Frozen rotor; discretization type-GGI
Fluid	Incompressible Newtonian fluid; water properties updated with actual density and viscosity
Boundary conditions	Inlet: total pressure inlet with direction, $P_{1,tot} = 231250$ [Pa] $\approx 12.05m$ net head Turbulence intensity 5% Outlet: Static pressure Reference pressure: 0 Pa Wall: No slip
Discretization and solution controls	Advection scheme: High resolution Turbulence numeric: High resolution
Turbulence models	Standard $k - \epsilon$
Convergence control	rms of pressure, mass-momentum, and turbulent parameters $\leq 10E-5$
Physical timescale	Auto timescale Conservative
Run type	Intel MPI Distributed Parallel: 5 nodes with 20 cores per node
Total run for GCI	PL (GV opening 70%): $n = 188$ rpm, $n = 244$ rpm and $n = 299$ rpm BEP (GV opening 100%): $n = 320$ rpm

All meshes were connected together with Frozen rotor interface between the stationary and the rotating domain. The frozen rotor interface works so that the frame of reference is changed but the relative orientation of the components across the interface is fixed. This model produces a steady-state solution to the multiple frame of reference problem, with some account of the interaction between the two frames. These interfaced together with the boundary conditions are shown in figure 2.

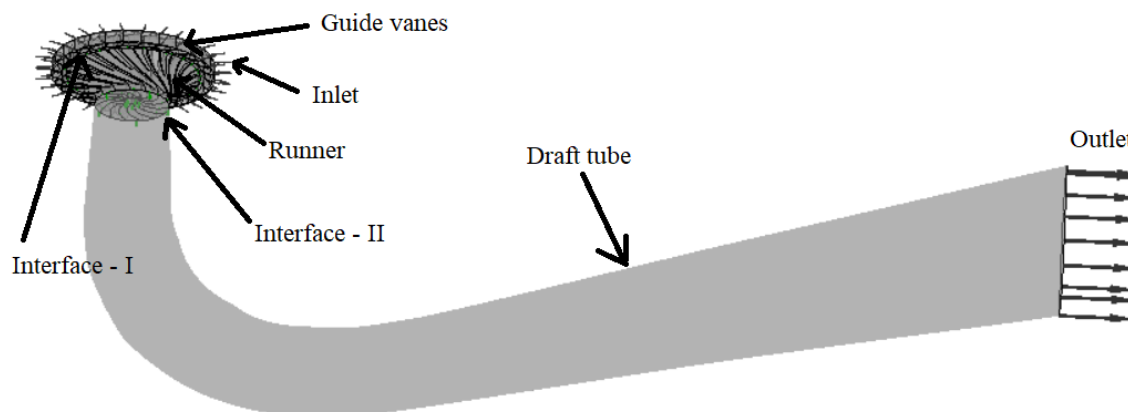


Figure 2. Computational domain of the model Francis turbine with two interfaces namely guide vane to runner (interfaceI) and runner to draft tube (interfaceII). Made similar to [9].

3.5. Boundary conditions

In addition to choosing interface and turbulence model, different boundary conditions have been tested in order to look at the effect of these. In the aforementioned study, Z. Yaping et al. [16] showed that the opening-type boundary condition gave a slightly better estimation of efficiency. In order to further investigate these effects, preliminary tests of several different outlet conditions were conducted. The pressure at the outlet was set equal to the measured pressure from experiments $P_{out} = 113kPa$.

As well as outlet condition, it is necessary to prescribe a proper inlet condition. Preliminary tests were conducted with mass flow inlet condition. However, when designing a new turbine, the flow rate corresponding to a certain guide vane opening is not known in advance. Therefore we want to know how accurate prediction is when a value of head is input data and a value of flow rate is the output of the numerical simulation. For that reason, numerical simulations were conducted with total pressure at the inlet. In this case, head becomes the input data, while a value of flow rate is a result of numerical simulation [17]. Total pressure inlet and static pressure outlet are very sensitive to initial guess, therefore the median pressure from experiments was applied. The total pressure inlet was set to $P_{1,tot} = 231250$ [Pa], which results in $\approx 12.05m$ net head.

4. Results and Discussion

The error in the quantities head, torque, and hydraulic efficiency will be regarded separately. This is to avoid that errors in head and torque cancels. Efficiency (η), given by equation (1), is proportional to $\propto T/H$, therefore it is important to look at the individual parameters to get a better understanding of the simulated efficiency. It is a common mistake to make, and could potentially lead to perfect results in hydraulic efficiency, even though both head and

torque have errors.

4.1. Mesh independence study

The recommended procedure for estimation of uncertainty due to discretization in CFD has been used to evaluate the mesh independence [18]. The grid convergence index (GCI) [18] is an industry-recognized method for assessing mesh quality but will not be repeated here. The computed flow parameters are tabulated in table 2-5:

Table 2. $n_{ED} \approx 0.13$, GV: 70%

Parameter	η [%]	T [Nm]	Q [m^3/s]
ϕ_1	84.600	618.96	0.16179
ϕ_2	84.488	615.02	0.16097
ϕ_3	83.940	586.76	0.15456
ϕ_{ext}^{21}	84.630	619.73	0.16194
GCI_{fine}^{21} [%]	0.051	0.156	0.11286
GCI_{med}^{32} [%]	0.217	0.958	0.75020

Table 3. $n_{ED} \approx 0.10$, GV: 70%

Parameter	η [%]	T [Nm]	Q [m^3/s]
ϕ_1	71.289	716.99	0.17163
ϕ_2	71.155	711.57	0.17650
ϕ_3	70.570	676.27	0.16350
ϕ_{ext}^{21}	71.34	718.18	0.16846
GCI_{fine}^{21} [%]	0.084	0.207	2.30914
GCI_{med}^{32} [%]	0.319	1.161	5.34657

Table 4. $n_{ED} \approx 0.16$, GV: 70%

Parameter	η [%]	T [Nm]	Q [m^3/s]
ϕ_1	92.495	511.07	0.14956
ϕ_2	92.434	508.62	0.14894
ϕ_3	91.961	486.40	0.14315
ϕ_{ext}^{21}	92.506	511.44	0.14965
GCI_{fine}^{21} [%]	0.015	0.091	0.07598
GCI_{med}^{32} [%]	0.097	0.693	0.59664

Table 5. $n_{ED} \approx 0.17$, GV:100%(BEP)

Parameter	η [%]	T [Nm]	Q [m^3/s]
ϕ_1	94.586	614.50	0.18446
ϕ_2	94.506	610.32	0.18335
ϕ_3	94.050	588.35	0.17758
ϕ_{ext}^{21}	94.605	615.58	0.18475
GCI_{fine}^{21} [%]	0.0248	0.220	0.19732
GCI_{med}^{32} [%]	0.1306	1.078	0.95526

Here ϕ and ϕ_{ext} is a variable critical to the conclusions being reported and the extrapolated value. The subscript 1, 2 and 3 denotes the fine, medium and coarse mesh, respectively. GCI_{fine}^{21} is the fine-grid convergence index and is a measure of discretization error of the mesh. The apparent order, p , of the solution ranged from 3.37 to 7.44. The different mesh sizes were made according to [18], with refinement factor $r > 1.3$. For table 2-4, $r_{21} = 1.318$ and $r_{32} = 1.346$. For table 5, $r_{21} = 1.312$ and $r_{32} = 1.326$. Presented in table 3; the highest estimated numerical uncertainties in the hydraulic efficiencies were $\approx 0.32\%$ and ≈ 0.08 with fine and medium grid densities, respectively. In general, the medium mesh showed lower uncertainties particularly on hydraulic efficiency, compared to torque and discharge. The maximum uncertainty was discharge (Q) at 5.35% with $n_{ED} \approx 0.10$ and GV angle 70%, using medium mesh. For the fine grid, the maximum uncertainty was 2.3%, on the same operating point.

The GCI_{fine}^{21} was very low compared to the GCI_{med}^{32} . The converged solution with the medium grid was used for further simulations at different operating conditions, considering how computationally demanding the fine grid was.

4.2. Hill chart

Using the medium mesh from the GCI study, 132 simulations with 11 different guide vane

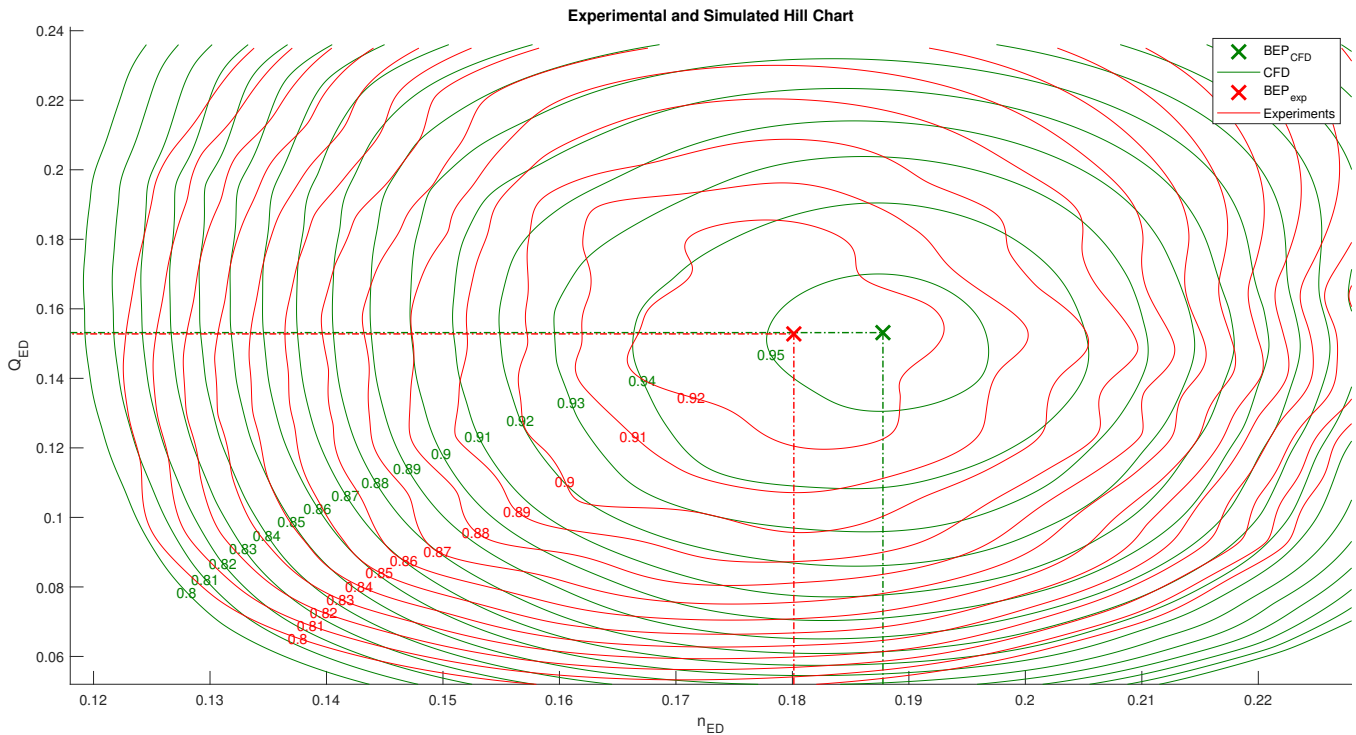


Figure 3. Red line shows experimental hill chart with data from [14]. Green line shows numerically predicted hill chart using CFD.

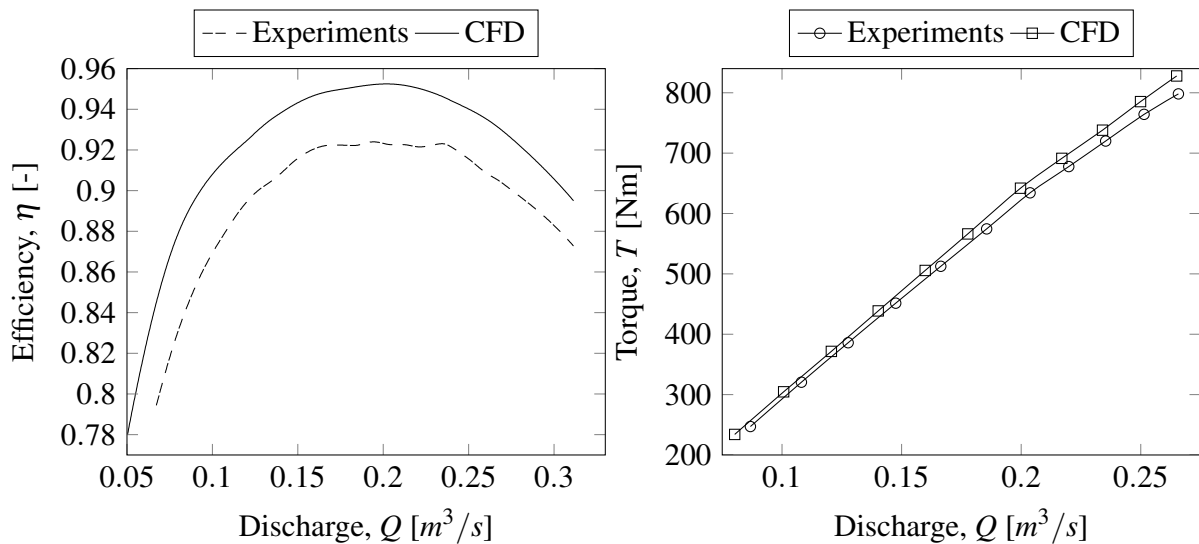


Figure 4. The left plot shows experimental and numerical CFD efficiency for constant $n_{ED} = 0.18$. The right plot shows torque for constant $n_{ED} = 0.18$.

A cross-section from the hill chart in figure 3 with constant $n_{ED} = 0.18$ is shown in figure

4. The constant n_{ED} -line describes the characteristics of normal operation. All simulations were carried out with GV opening in the range of [40%, 140%] with an increment of $\approx 10\%$ or 1° angle. The approximation (\approx) used throughout the paper is only used to present the data. All simulations were carried out using experimental values as input.

The hydraulic efficiency was numerically predicted with the maximum difference found at GV opening of 60% and $n = 432.5$ rpm, was calculated to be 6.93%, compared to experiments. The difference (Δ) is calculated as, $\Delta X = X_{numerical} - X_{experimental}$, where X is the variable of interest. At the lowest guide vane opening (40%), the minimum difference in efficiency was found at 0.13%, with $n = 244.4$ rpm. This is not trivial, as stated earlier, this is a highly problematic operating point with transient flow occurring in the draft tube. It is also recognizable considering other studies on the same runner, presented in a review paper by Trivedi et al. [12], showed a larger deviation in efficiency at part load than this study. The maximal difference in torque, found at GV opening of 140% and $n = 222.5$ rpm, was calculated to be 72.4 Nm.

Even more important than absolute value of efficiency is getting the shape of the efficiency curve and the position of BEP. Figure 3 shows that the BEP for numerical results is higher, i.e. higher efficiency, and shifted to the right in the hill chart compared to experiments. Q_{ED} matches almost exactly the experimental value whereas the n_{ED} is off by 4.3%. The average difference in efficiency was 2.87% for the whole hill chart. D. Jošt et al. [17] tested both head and volume flow as input data, and found that volume flow was slightly underpredicted when using head as input data. Similarly, this study underpredicted volume flow, on average, -5.6 l/s. D. Celič et al. [15] studied the influence on hydraulic efficiency from labyrinth losses. They found that the difference between the experimental and numerical efficiency lowers down from 7% to 2% at PL operation. It is believed that this is the main contributor to the discrepancies in efficiency in this study. However, the discrepancies could also come from disregarding losses in the spiral case and stay vanes. In general efficiency is overestimated, otherwise, the shape of the efficiency curve is fairly well captured.

5. Conclusion

Flow in a high head Francis turbine was analyzed by using $k - \varepsilon$ turbulence model. Numerical simulations were performed at 132 representative operating points and compared with available experimental data to verify its reliability. The difference between the experimental and numerical results was on average 2.87% overprediction, with the maximum difference (6.93%) being observed at $n_{ED} = 432.5$ and GV opening 60%. The BEP for the numerical results was higher and shifted to the right, compared to experiments. Torque was well predicted for most operating points. Simulations for the mesh independence study were carried out at part load, with guide vane opening of 70% for three different runner speeds. Mesh independence was also studied at BEP. This grid scaling test showed grid discretization uncertainties up to 5.34% in discharge, Q . Medium mesh size was selected for further use due

to computational cost. The shape of the efficiency curve was fairly well captured, however more accurate prediction could be achieved with other turbulence models.

References

- [1] T. Vu and W. Shyy, "Performance prediction by viscous flow analysis for Francis turbine runner," *Journal of fluids engineering*, vol. 116, no. 1, pp. 116–120, 1994.
- [2] M. Sabourin, Y. Labrecque, and V. De Henau, "From components to complete turbine numerical simulation," in *Hydraulic Machinery and Cavitation*, pp. 248–256, Springer, 1996.
- [3] K. Anup, B. Thapa, and Y.-H. Lee, "Transient numerical analysis of rotorstator interaction in a Francis turbine," *Renewable Energy*, vol. 65, pp. 227 – 235, 2014. SI:AFORE 2012.
- [4] H. Akin, Z. Aytac, F. Ayancik, E. Ozkaya, E. Arioz, K. Celebioglu, and S. Aradag, "A CFD aided hydraulic turbine design methodology applied to Francis turbines," in *Power Engineering, Energy and Electrical Drives (POWERENG), 2013 Fourth International Conference on*, pp. 694–699, IEEE, 2013.
- [5] J. Wu, K. Shimmei, K. Tani, K. Niikura, and J. Sato, "Cfd-based design optimization for hydro turbines," *Journal of Fluids Engineering*, vol. 129, no. 2, 2007.
- [6] S. Aradag, H. Akin, and K. Celebioglu, "CFD based design of a 4.3MW francis turbine for improved performance at design and off-design conditions," *Journal of Mechanical Science and Technology*, vol. 31, pp. 5041–5049, Oct 2017.
- [7] H. Keck, P. Drtina, and M. Sick, "Numerical hill chart prediction by means of CFD stage simulation for a complete francis turbine," in *Hydraulic Machinery and Cavitation*, pp. 170–179, Springer, 1996.
- [8] E. Tengs, P.-T. Storli, and M. A. Holst, "Numerical generation of hill-diagrams; validation on the francis99 model turbine," *International Journal of Fluid Machinery and Systems*, vol. 11, no. 3, pp. 294–303, 2018.
- [9] C. Trivedi, M. Cervantes, B. K. Gandhi, and O. G. Dahlhaug, "Experimental and numerical studies for a high head Francis turbine at several operating points," *Journal Of Fluids Engineering - Transactions Of The Asme*, vol. 135, no. 11, 2013.
- [10] International Electrotechnical Commission, "Hydraulic turbines, storage pumps and pump-turbines - Model acceptance tests," Nov. 1999.
- [11] H. Brekke, *Introduction To Hydraulic Machinery*. NTNU, March 2000.
- [12] C. Trivedi, M. Cervantes, and O. G. Dahlhaug, "Experimental and numerical studies of a high-head francis turbine: A review of the Francis-99 Test Case," *Energies*, 2016.
- [13] C. Bergan, R. Goyal, M. J. Cervantes, and O. G. Dahlhaug, "Experimental investigation of a high head model Francis turbine during steady-state operation at off-design conditions," *IOP Conference Series: Earth and Environmental Science*, vol. 49, no. 6, 2016.
- [14] I. Iliev, C. Trivedi, E. Agnalt, and O. G. Dahlhaug, "Variable-speed operation and pressure pulsations in a francis turbine and a pump-turbine," *IOP Conference Series: Earth and Environmental Science*, vol. 240, p. 072034, mar 2019.
- [15] D. Celič and H. Ondráčka, "The influence of disc friction losses and labyrinth losses on efficiency of high head Francis turbine," *Journal of Physics: Conference Series*, vol. 579, no. 1, p. 012007, 2015.
- [16] Z. Yaping, L. Weili, R. Hui, and L. Xingqi, "Performance study for Francis-99 by using different turbulence models," *Journal of Physics: Conference Series*, vol. 579, no. 1, p. 012012, 2015.
- [17] D. Jošt, A. Skerlavaj, M. Morgut, P. Mežnar, and E. Nobile, "Numerical simulation of flow in a high head Francis turbine with prediction of efficiency, rotor stator interaction and vortex structures in the draft tube," *Journal of Physics: Conference Series*, vol. 579, no. 1, p. 012006, 2015.
- [18] I. Celik, U. Ghia, P. Roache, C. Freitas, H. Coleman, and P. Raad, "Procedure for estimation and reporting of uncertainty due to discretization in CFD applications," *Journal of Fluids Engineering (Transactions of the ASME)*, vol. 130, no. 7, pp. 078001 (4)–078001 (4), 2008.

A.2 Correction of dimensions according to synchronous speed

In order to meet the demand of synchronous speed Francis turbine, we have to correct the dimensions of the outlet of the runner. This is done by the following procedure.

First, we have to assume that we have the same discharge at BEP, *Q . Then we get the following relation by correction of rotational speed for $\beta_2 = const.$ and $c_{u2} = const.$ (i.e conformed velocity diagram).

$$c_{m2corr} = \frac{4^*Q}{\pi D_{2corr}^2} \quad \& \quad c_{m2} = \frac{4^*Q}{\pi D_2^2} \quad (31)$$

which gives

$$\frac{c_{m2corr}}{c_{m2}} = \left(\frac{D_2}{D_{2corr}} \right)^2 = \frac{u_{2corr}}{u_2}. \quad (32)$$

Further we have that $\beta_2 = const.$ and $c_{u2} = cu_{2corr} = 0$, which gives that,

$$\tan(\beta_2) = \frac{c_{m2}}{u_2} = \frac{4^*Q/\pi D_2^2}{\frac{\pi}{60}nD_2} \quad \& \quad \tan(\beta_2) = \frac{c_{m2corr}}{u_{2corr}} = \frac{Q/\pi D_{2corr}^2}{\frac{\pi}{60}nD_{2corr}} \quad (33)$$

This gives,

$$n_{corr}D_{2corr}^3 = nD_2^3 \quad \vee \quad D_{2corr} = \left(\frac{nD_2^3}{n_{corr}} \right)^{\frac{1}{3}}. \quad (34)$$

If we instead insert a given number of pole pair, Z_p , and calculate n_{corr} directly, we can find D_{2corr} directly. We then have to calculate a correction value for $u_2 = u_{2corr}$ which is given by the following equation;

$$u_{2corr} = n_{corr} \cdot \pi \cdot D_{2corr} / 60. \quad (35)$$

Further exist c_{m2} as,

$$c_{m2} = u_{2corr} \cdot \tan(\beta_2), \quad (36)$$

A control of c_{m2} can be done by the following equation;

$$c_{m2} = \frac{4^*Q}{\pi D_{2corr}^2}. \quad (37)$$

The outlet geometry at the trailing edge of the blade with $D_2 = D_{2corr}$ is now derived. Make sure that the submergence is controlled after (1). If the submergence is too large, we have to select a lower peripheral velocity by increasing the number of pole pairs and a turbine with lower speed number or change *Q and make a smaller turbine to the selected rpm.

A.3 Reynolds-averaged Navier-Stokes equations (RANS)

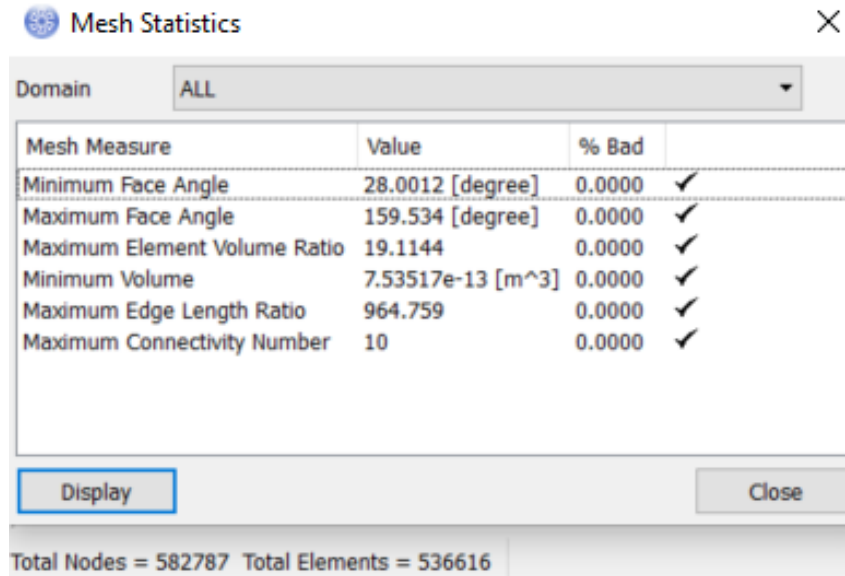
The RANS equations, as shown in (38), are time-averaged equations of motion used to describe the motion of turbulent fluid flow. However, the unknown Reynolds stress needs another term in order to be solved. This can be done by the linear eddy viscosity model, put forth by Boussinesq [80] and presented in (39).

$$\rho \overline{U_j} \frac{\partial \overline{U_i}}{\partial x_j} = \rho \overline{f_i} + \frac{\partial}{\partial x_j} \left[-\overline{p} \delta_{ij} + \mu \left(\frac{\partial \overline{U_i}}{\partial x_j} + \frac{\partial \overline{U_j}}{\partial x_i} \right) \right] - \rho \overline{u'_i u'_j} \quad (38)$$

$$\overline{u'_i u'_j} = \frac{2}{3} k \delta_{ij} - \nu_T \left(\frac{\partial \overline{U_i}}{\partial x_j} + \frac{\partial \overline{U_j}}{\partial x_i} \right) \quad (39)$$

where, $\overline{f_i}$ represents the external forces, μ is the fluid viscosity, $\overline{u'_i u'_j}$ is the Reynolds stress, δ_{ij} is the Kronecker delta, ν_T is the turbulent eddy viscosity and $\overline{U_{i,j}}$ the mean velocity.

A.4 Mesh statistics for medium mesh for the different domains



Mesh Measure	Value	% Bad	
Minimum Face Angle	28.0012 [degree]	0.0000	✓
Maximum Face Angle	159.534 [degree]	0.0000	✓
Maximum Element Volume Ratio	19.1144	0.0000	✓
Minimum Volume	7.53517e-13 [m^3]	0.0000	✓
Maximum Edge Length Ratio	964.759	0.0000	✓
Maximum Connectivity Number	10	0.0000	✓

Total Nodes = 582787 Total Elements = 536616

Figure A.1: Mesh statistic for the runner in TurboGrid with 536 616 elements (medium mesh) in one passage. The statistics show that all elements are good in this mesh.

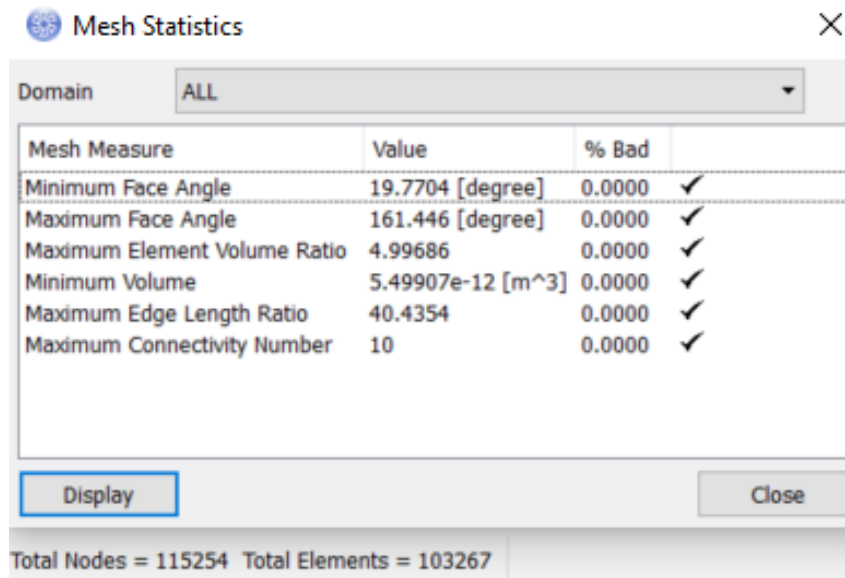


Figure A.2: Mesh statistic for the guide vane ($\alpha = 7^\circ$) in TurboGrid with 103 267 elements (medium mesh) in one passage. The statistics show that all elements are good in this mesh.

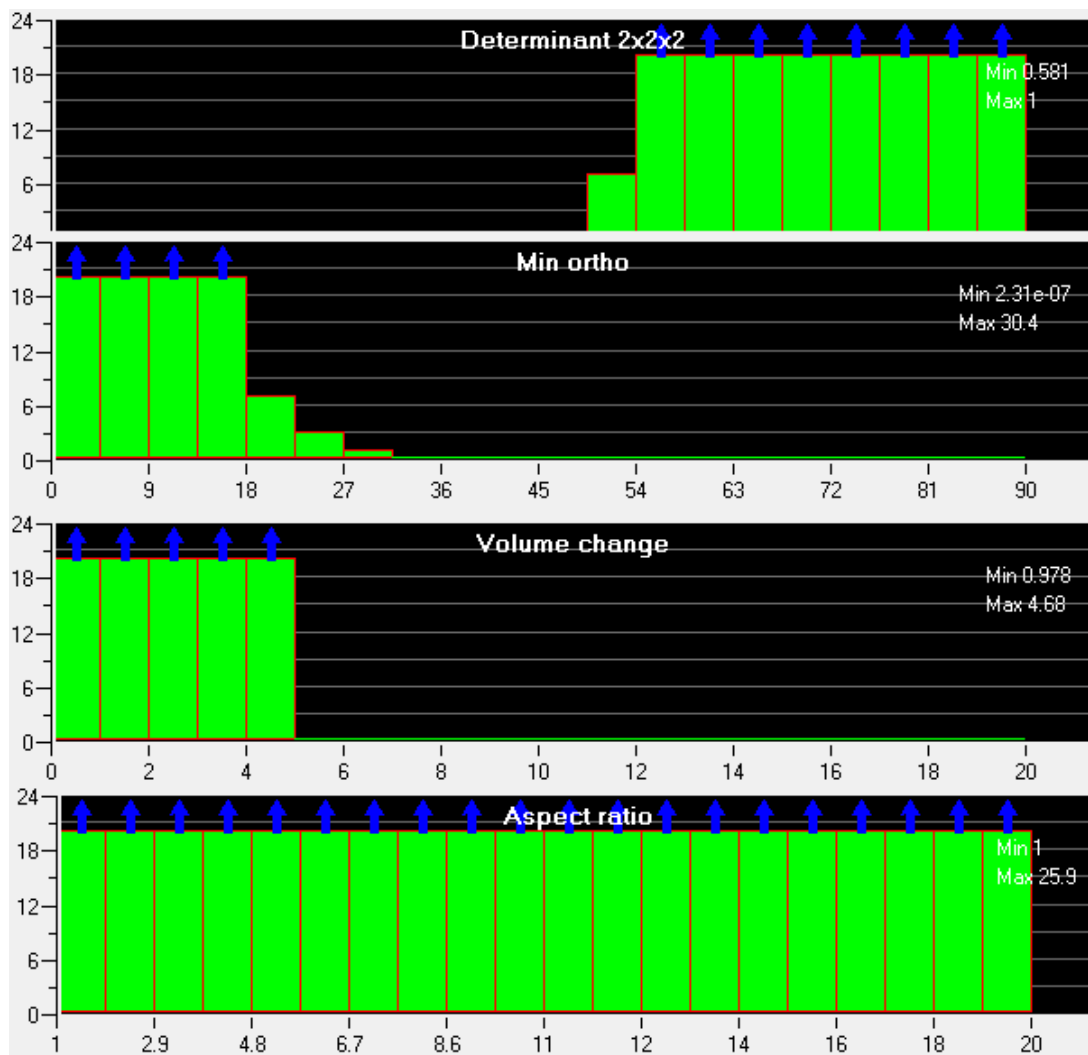


Figure A.3: Mesh statistic for the draft tube in ICEM CFD with 851 190 elements (medium mesh). The statistics show that all elements are good in this mesh.

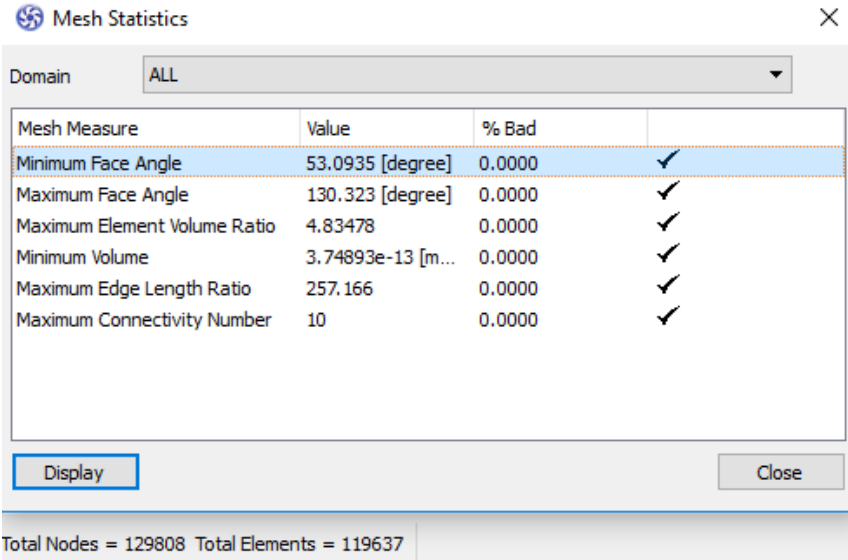
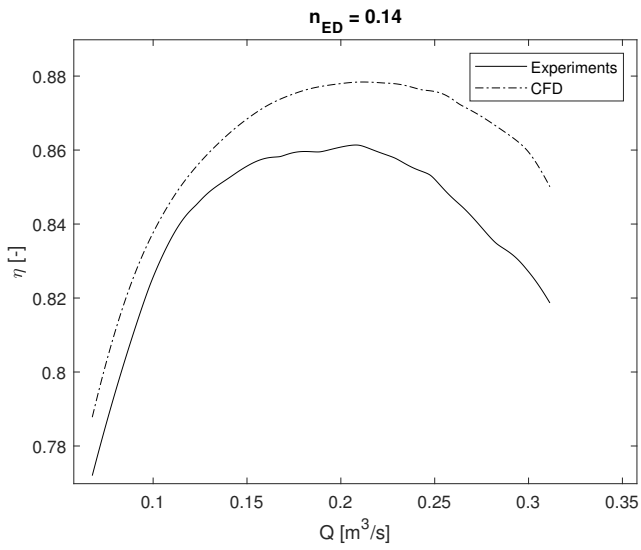
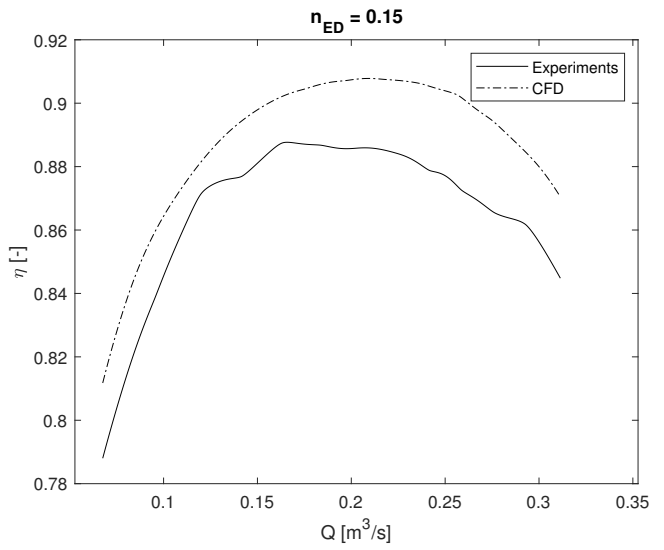


Figure A.4: Mesh statistic for the simplified guide vane in TurboGrid with 119 637 elements. The statistics show that all elements are better in this mesh compared to Fig. A.2.

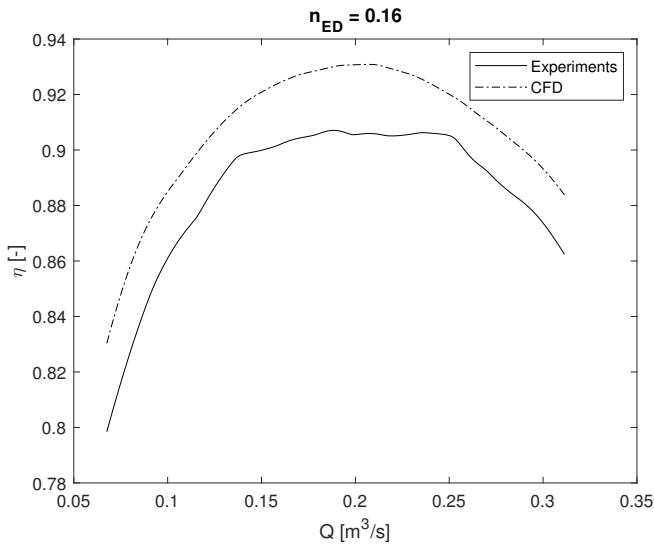
A.5 Constant n_{ED} -efficiency plots



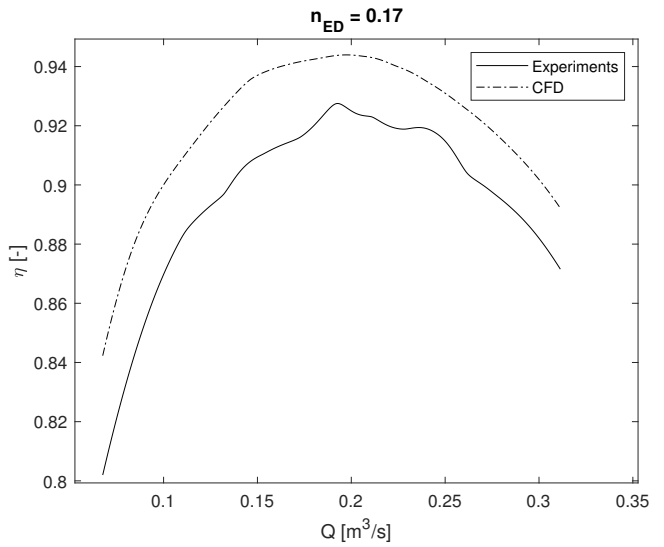
(a) Exp. and num. hill chart with $n_{ED} = 0.14$.



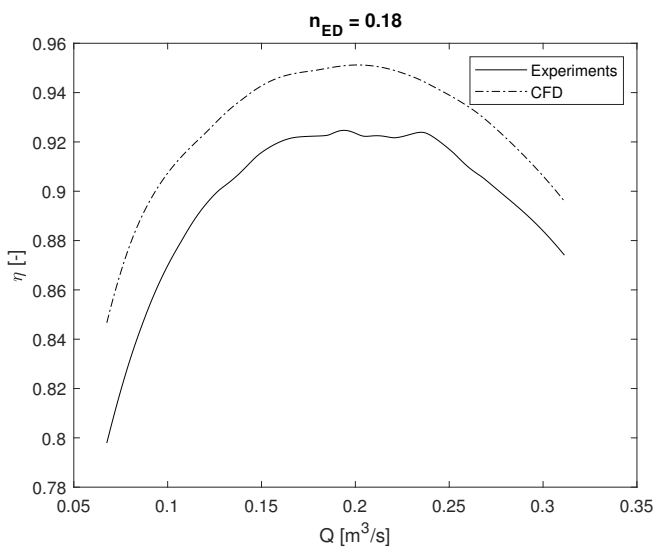
(b) Exp. and num. hill chart with $n_{ED} = 0.15$.



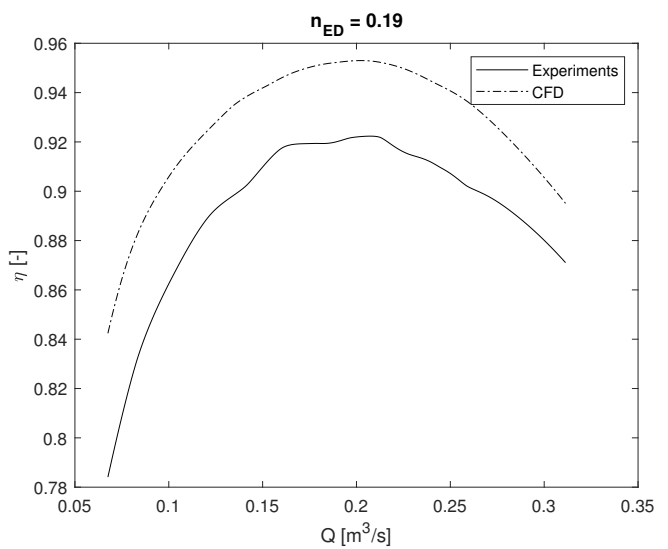
(c) Exp. and num. hill chart with $n_{ED} = 0.16$.



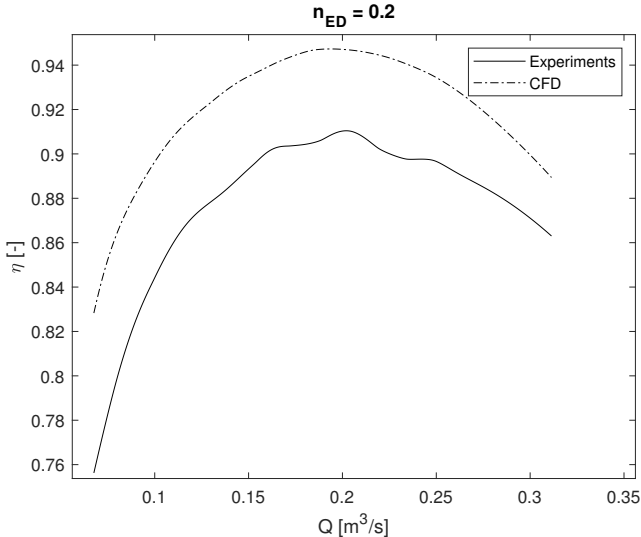
(d) Exp. and num. hill chart with $n_{ED} = 0.17$.



(e) Exp. and num. hill chart with $n_{ED} = 0.18$.



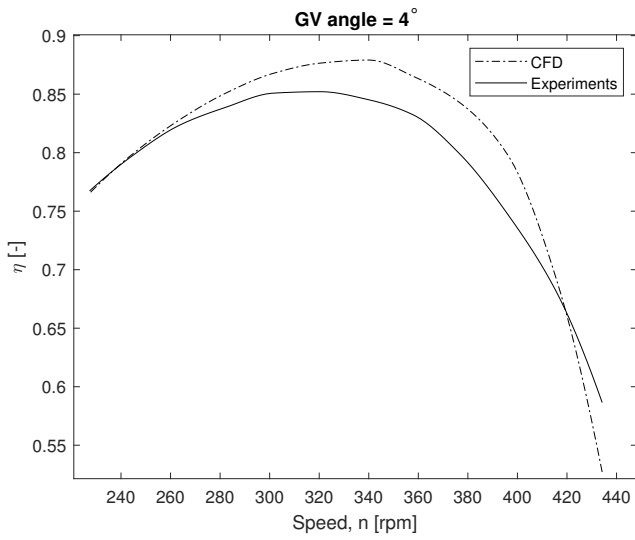
(f) Exp. and num. hill chart with $n_{ED} = 0.19$.



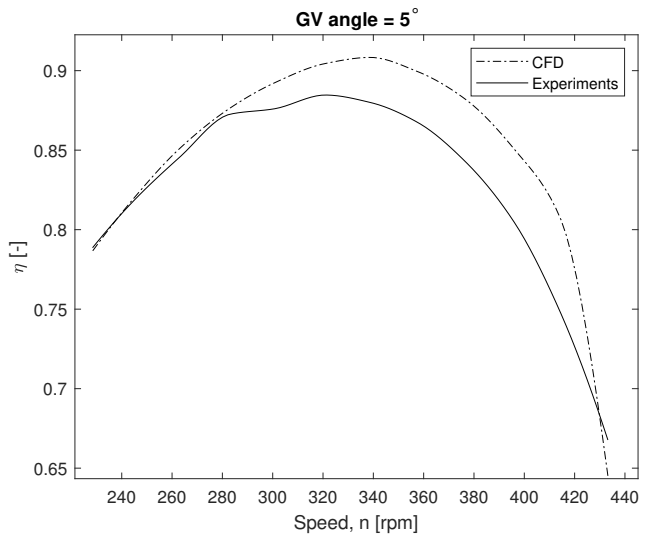
(g) Exp. and num. hill chart with $n_{ED} = 0.19$.

Figure A.6: Experimental and numerical hill charts for different constant n_{ED} lines.

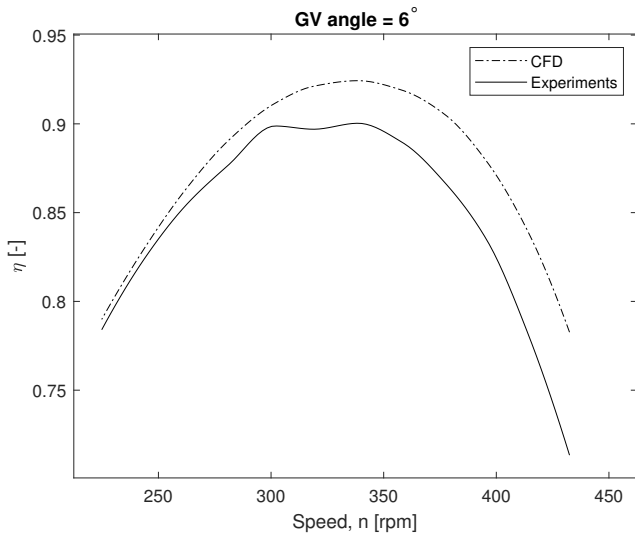
A.6 Constant guide vane opening efficiency plots



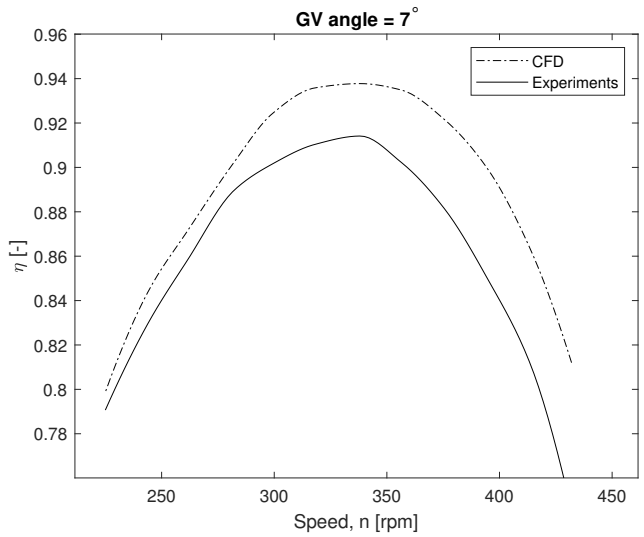
(a) Exp. and num. hill chart with $\alpha = 4^\circ$.



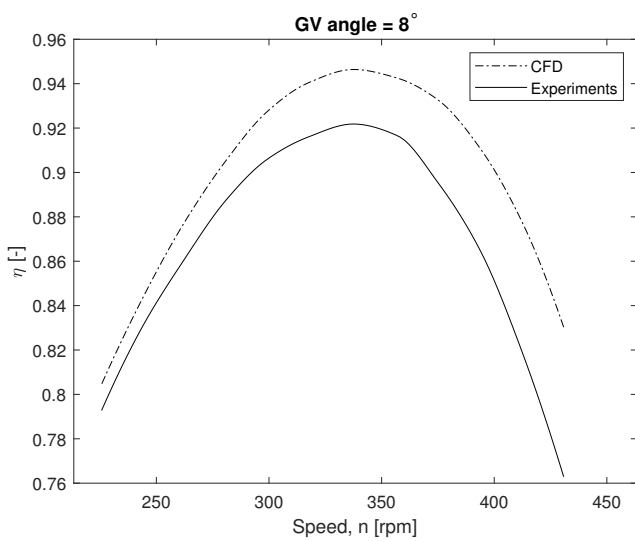
(b) Exp. and num. hill chart with $\alpha = 5^\circ$.



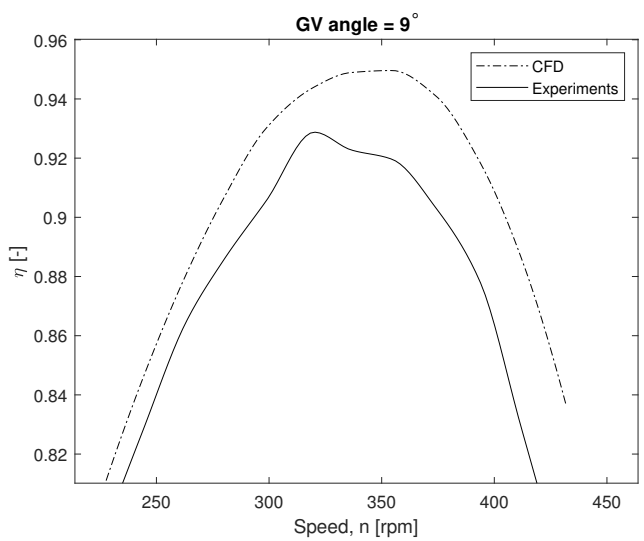
(c) Exp. and num. hill chart with $\alpha = 6^\circ$.



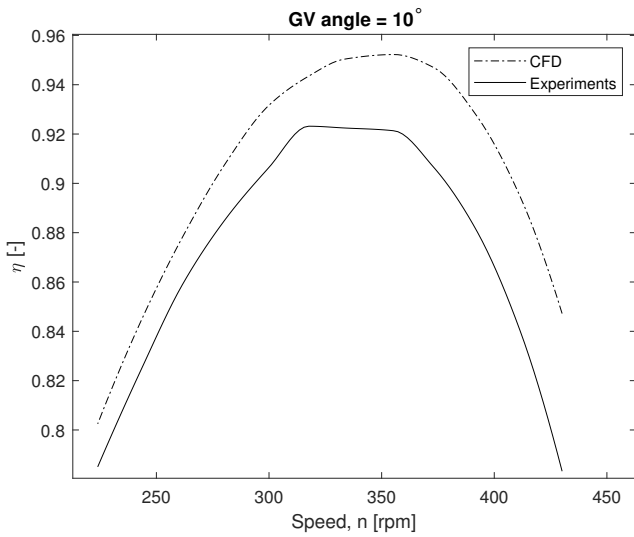
(d) Exp. and num. hill chart with $\alpha = 7^\circ$.



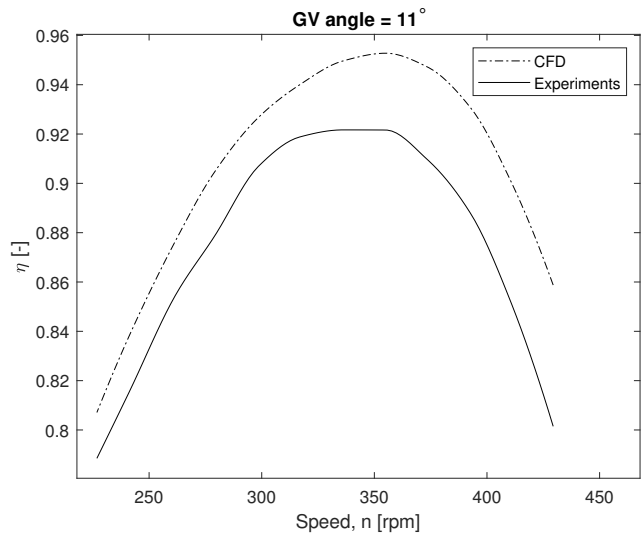
(e) Exp. and num. hill chart with $\alpha = 8^\circ$.



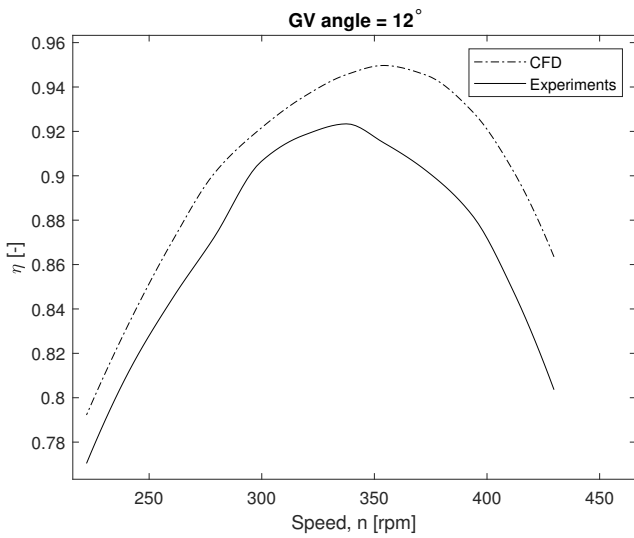
(f) Exp. and num. hill chart with $\alpha = 9^\circ$.



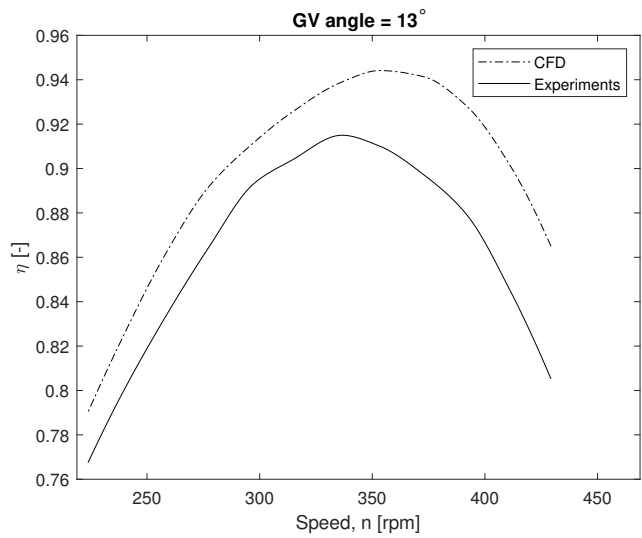
(g) Exp. and num. hill chart with $\alpha = 10^\circ$.



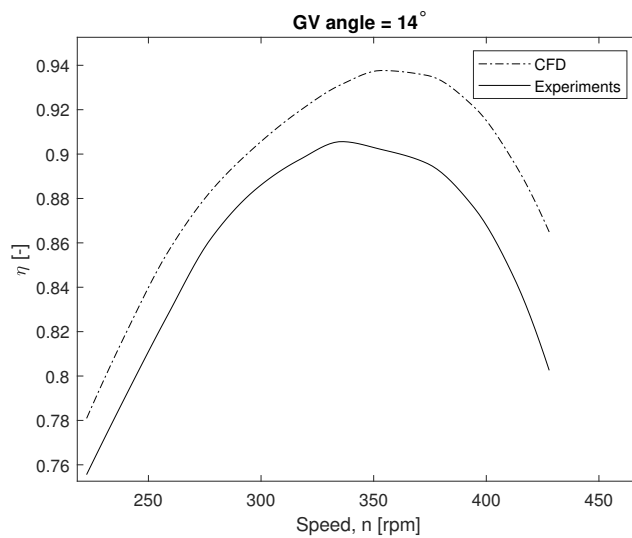
(h) Exp. and num. hill chart with $\alpha = 11^\circ$.



(i) Exp. and num. hill chart with $\alpha = 12^\circ$.



(j) Exp. and num. hill chart with $\alpha = 13^\circ$.



(g) Exp. and num. hill chart with $\alpha = 14^\circ$.

Figure A.8: Experimental and numerical hill charts for different guide vane openings (α).

A.7 Euler efficiency hill chart compared to normal efficiency

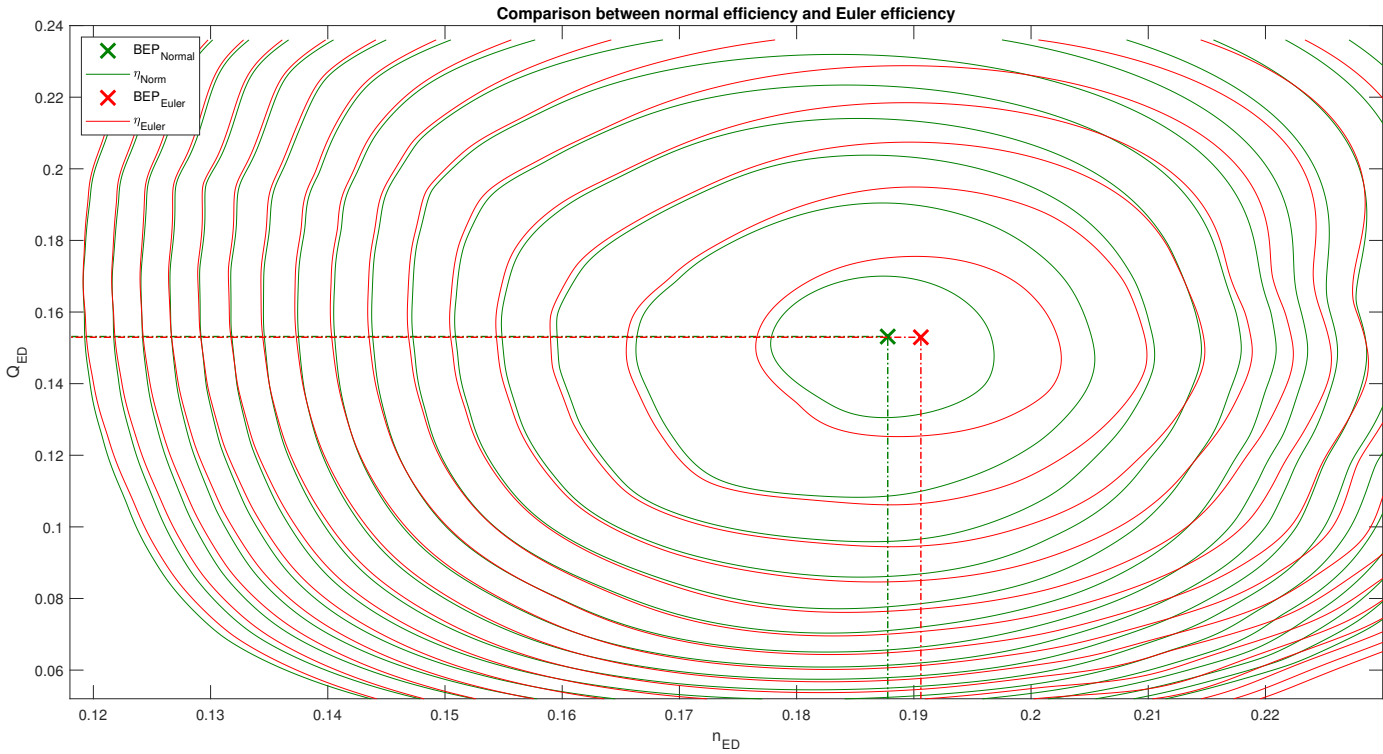


Figure A.9: Comparison between Euler efficiency hill chart according to (7) and normal efficiency according to (16).

A.8 MATLAB Script for creating the Hill chart

```

1 %% Creating Hill-diagram
2
3 % Load excel data
4 load('CopyofF99expdata.mat')
5 F99expdata = table2array(CopyofF99expdata);
6
7 % Variables
8 g = 9.82;
9 D2 = 0.349;
10 % Assign data to variables
11 a = [F99expdata([50:61 68:79 87:98 107:118 127:138 148:159 169:180 190:201 211:222 232:243
253:264],1)];
12 n = [F99expdata([50:61 68:79 87:98 107:118 127:138 148:159 169:180 190:201 211:222 232:243
253:264],2)];
13 H = [F99expdata([50:61 68:79 87:98 107:118 127:138 148:159 169:180 190:201 211:222 232:243
253:264],3)];
14 Q = [F99expdata([50:61 68:79 87:98 107:118 127:138 148:159 169:180 190:201 211:222 232:243
253:264],4)];
15 T = [F99expdata([50:61 68:79 87:98 107:118 127:138 148:159 169:180 190:201 211:222 232:243
253:264],5)];
16 eta = [F99expdata([50:61 68:79 87:98 107:118 127:138 148:159 169:180 190:201 211:222 232:243
253:264],6)];
17
18 % Calculation of n_ed Q_ed
19 ned = (n.*D2)./(60*sqrt(g.*H));
20 Qed = Q./(D2^2.*sqrt(g.*H));
21
22 % Finding BEP
23 BEP = find(eta==max(eta));
24 BEPx = ned(BEP);
25 BEPy = Qed(BEP);
26 BEPz = eta(BEP);
27
28 % Plot figure
29 figure(1)
30 xlabel('ned')
31 ylabel('Qed')
32 zlabel('eta')
33 hold on
34
35 % Assingning to new variable name
36 X = ned;
37 Y = Qed;
38 Z = eta;
39
40 % Surface plot and interpolation
41 [xq,yq] = meshgrid(linspace(round(min(X),3),round(max(X),3),1000),linspace(round(min(Y),3),
round(max(Y),3),1000)));
42 vq = griddata(X,Y,Z,xq,yq,'v4');
43 mesh(xq,yq,vq)
44 plot3(X,Y,Z,'.',BEPx,BEPy,BEPz,'rx')
45
46 % Contour plot with points and projection points
47 figure(2)
48 hold on
49
50 %Plot data points
51 plot(ned,Qed,'b.','MarkerSize',3,'LineWidth',3,'HandleVisibility','off')
52 %Plot BEP from dataset
53 plot(BEPx,BEPy,'kx','MarkerSize',5,'LineWidth',2,'HandleVisibility','on')
54
55 %Plot interpolated BEP
56 [BEP1,BEP2] = find(vq==max(vq(:)));
57 BEPxq = xq(BEP1,BEP2);
58 BEPyq = yq(BEP1,BEP2);
59 BEPzq = vq(BEP1,BEP2);
60
61 plot(BEPxq,BEPyq,'rx','MarkerSize',14,'LineWidth',2)
62 plot([BEPxq,BEPxq,0],[0,BEPyq,BEPyq],'-','Color','r','LineWidth',1,'HandleVisibility','off')

```



```
63
64 minLevel = 0.8;
65 maxLevel = 0.92;
66 numberOfLevels = 13;
67 levels = sort([linspace(minLevel, maxLevel, numberOfLevels), linspace(minLevel, maxLevel,
    numberOfLevels)]);
68
69 [C,h] = contour(xq,yq,vq,[levels 0.923 0.923], 'Color','r', 'LineStyle','-', 'HandleVisibility','
    on');
70 clabel(C,h, 'manual', 'Rotation',0, 'Color','r')
71 plot([0,0.001],[0,0.001], 'r-', 'HandleVisibility','off')
72
73 % Calculating the variable speed line
74 for i = 2:(size(xq,1)-1)
75     for j = 2:(size(yq,2)-1)
76         s(j-1,[1,2,3]) = [xq(i,j),yq(i,j),vq(i,j)];
77     end
78     var(i-1,[1,2,3]) = [s(find(s(:,3))==max(s(:,3))),1),s(find(s(:,3))==max(s(:,3))),2),s(find(s
        (:,3))==max(s(:,3))),3)];
79 end
80
81 plot(var(110:820,1),var(110:820,2), '-r', 'LineWidth',1.5)
82 % Plot legends and title
83 legend('BEP_{Interpolated}','\eta', 'Variable speed', 'Location', 'NorthWest');
84 title('Experimental Hill Chart')
85 xlabel('n_E_D')
86 ylabel('Q_E_D')
87 zlabel('\eta')
88 axis([0.118 0.23 0.052 0.24])
```

,

A.9 Different messages from ANSYS

Here are some error messages from ANSYS:

```

+-----+
|                                     |
|                               Host Memory Information (Mbytes)                |
|                                     |
+-----+-----+-----+-----+-----+
| Host          | Npart | System  | Allocated | %      |
+-----+-----+-----+-----+-----+
| IEPT1128     |      8 | 32676.22 | 33261.41 | 101.79 |
+-----+-----+-----+-----+-----+

+-----+-----+-----+-----+-----+
| ERROR #333100220 has occurred in subroutine Out_Memory.                    |
| Message:                                                                 |
|                                                                 |
| The allocated memory exceeds the system memory on      1 host(s).        |
|                                                                 |
| The logical expert parameter "enforce system memory limit"                |
| controls whether this is a fatal error.                            |
|                                                                 |
| The current setting is: fatal                                           |
|                                                                 |
| Allocating more than the system memory may result in slow or              |
| unreliable operation and is not recommended.                        |
+-----+-----+-----+-----+-----+

```

Figure A.10: Memory problem that happens when simulating too many cells, in this case 27.7 million.

```

=====
OUTER LOOP ITERATION = 704                      CPU SECONDS = 1.260E+06
=====
| Equation      | Rate | RMS Res | Max Res | Linear Solution |
+-----+-----+-----+-----+-----+
| U-Mom        | 1.05 | 2.9E-05 | 4.3E-03 | 1.2E-01 ok|
| V-Mom        | 1.05 | 2.6E-05 | 5.3E-03 | 1.6E-01 ok|
| W-Mom        | 1.01 | 2.6E-05 | 1.8E-03 | 1.3E-01 ok|
| P-Mass       | 1.02 | 1.4E-05 | 5.7E-03 | 18.5 6.1E-02 OK|
+-----+-----+-----+-----+-----+
|                                     |
| ***** Notice *****          |
| A wall has been placed at portion(s) of an OUTLET                    |
| boundary condition (at 53.0% of the faces, 40.2% of the area)        |
| to prevent fluid from flowing into the domain.                        |
| The boundary condition name is: Outlet.                                |
| The fluid name is: Fluid 1.                                           |
| If this situation persists, consider switching                          |
| to an Opening type boundary condition instead.                          |
+-----+-----+-----+-----+-----+
| K-TurbKE     | 1.03 | 2.7E-04 | 2.2E-02 | 10.6 7.1E-02 OK|
| E-Diss.K     | 1.27 | 6.7E-04 | 1.2E-01 | 12.0 2.3E-03 OK|
+-----+-----+-----+-----+-----+

```

Figure A.11: Artificial wall problem that happens when simulating SST turbulence model.

```

=====
OUTER LOOP ITERATION =      5                      CPU SECONDS = 2.956E+03
-----
|      Equation      | Rate | RMS Res | Max Res | Linear Solution |
+-----+-----+-----+-----+-----+
| Wallscale          | 0.60 | 4.5E-05 | 1.4E-03 | 20.7 7.6E-02 OK|
+-----+-----+-----+-----+-----+
| U-Mom              | 0.09 | 1.6E-03 | 5.0E-02 | 3.5E+04 F |
| V-Mom              | 0.01 | 1.5E-04 | 7.1E-03 | 7.3E+04 F |
| W-Mom              | 0.10 | 6.8E-04 | 2.1E-02 | 5.5E+05 F |
| P-Mass             | 0.00 | 6.8E-07 | 3.6E-05 | 9.5 3.7E+07 F |
+-----+-----+-----+-----+-----+
|                    |      |         |         |                 |
|          ***** Notice *****          |
| A wall has been placed at portion(s) of an OUTLET |
| boundary condition (at 1.6% of the faces, 1.2% of the area) |
| to prevent fluid from flowing into the domain. |
| The boundary condition name is: outlet. |
| The fluid name is: Fluid 1. |
| If this situation persists, consider switching |
| to an Opening type boundary condition instead. |
+-----+-----+-----+-----+-----+
|                    |      |         |         |                 |
|          ***** Notice *****          |
| A wall has been placed at portion(s) of an INLET |
| boundary condition (at 64.1% of the faces, 52.3% of the area) |
| to prevent fluid from flowing out of the domain. |
| The boundary condition name is: Inlet. |
| The fluid name is: Fluid 1. |
| If this situation persists, consider switching |
| to an Opening type boundary condition instead. |
+-----+-----+-----+-----+-----+
|                    |      |         |         |                 |
| ERROR #001100279 has occurred in subroutine ErrAction. |
| Message: |
| Floating point exception: Overflow |
| |
| |
| |
+-----+-----+-----+-----+-----+

```

Figure A.12: Overflow problem that happens when simulating total pressure inlet.

A.10 Script for running jobs on Idun

```
#!/bin/bash

## Specify job name, simulation time, number of nodes, partition, RAM memory, Array (loops
w, i.e. path, from 0-10 where %2 means max two jobs at once), and mail to user for updates:

#SBATCH --job-name=9deg_RNG_files
#SBATCH -t 28:20:00
#SBATCH --nodes=6 --ntasks-per-node=20
#SBATCH --partition=WORKQ
#SBATCH --mem=120000
#SBATCH --array=0-10%2
#SBATCH --mail-type=ALL
#SBATCH --mail-user=andnordv@stud.ntnu.no

## Makes error files in case of failure:
#SBATCH --output=%j.out
#SBATCH --error=%j.err

## Recommended safety settings:
set -o errexit # Make bash exit on any error
set -o nounset # Treat unset variables as errors

# Make sure the directory with chat case exists by setting the environmental variable $w to the
# sub-directory and test for its existence
w=/home/$USER/$SLURM_JOB_NAME/dp$SLURM_ARRAY_TASK_ID/CFX/CFX/
if [ ! -d $w ]; then mkdir -p $w;fi

## Copy a .ccl file to $w, which can edit the setup (here I change turbulence model to RNG):
cp RNG.ccl $w
cd $w

## Create host list
srun hostname -s | sort > /tmp/hosts.$SLURM_JOB_ID
nodes='tr
n' ; < /tmp/hosts.$SLURM_JOB_ID

# echo "nodes= "$nodes

module load CFX/19.2

export CFX5RSH=ssh

## Run the application
cfx5solve -def CFX.def -maxet "28[hr]" -double -parallel -batch -ccl RNG.ccl -large -s 1.5 -
start-method 'Intel MPI Distributed Parallel' -par-dist $nodes

## Clean up
rm /tmp/hosts.$SLURM_JOB_ID
```

A.11 Script for running jobs on Vilje

```
#!/bin/bash
#####
#
# Running CFX in distributed parallel mode
#
#####
# Specify -N (job name), -A (project number), -l (select="number of nodes"), -l (simulation
time), -J (Array, looping w, i.e. path), -j (create error files), and -m (mail to user):

#PBS -N dp
#PBS -A nn9669k
#PBS -l select=8:ncpus=32:mpiprocs=16
#PBS -l Fluent=32
#PBS -l walltime=21:20:00
#PBS -J 0-10
#PBS -j oe
#PBS -m abe

module load cfx/19.1

# Creates a variable which is coupled with -N (job name) and -J (array loop) above:
case=$PBS_JOBNAME$PBS_ARRAY_INDEX

cd $PBS_O_WORKDIR

# Create (if necessary) the working directory
w=/work/$PBS_O_LOGNAME/9deg_RNG_files/$case/CFX/CFX/
if [ ! -d $w ]; then mkdir -p $w; fi

# Copy inputfile and move to working directory
cp SST.ccl $w
cd $w

nodes='cat $PBS_NODEFILE'
nodes='echo $nodes | sed -e 's/ /,g''

export CFX5RSH=ssh

# Run the application: cfx5solve -batch -maxet "29[hr]" -double -parallel -batch -ccl SST.ccl
-large -s 1.5 -def CFX.def -start-method 'Platform MPI Distributed Parallel' -par-dist $nodes
```

